Dissertation
submitted to the
Combined Faculties of the Natural Sciences and Mathematics
of the Ruperto-Carola-University of Heidelberg, Germany
for the degree of
Doctor of Natural Sciences

put forward by
Dipl.-Phys. Benjamin Joachim Galow
born in Mannheim, Germany
Oral examination: 18th January 2012

Laser-generated Ion Beams for Medical Applications

Referees: **Hon.-Prof. Dr. Christoph H. Keitel**
PD Dr. Andrey Surzhykov

Zusammenfassung

Das Aufkommen von Hochleistungs-Lasersystemen ebnete den Weg für Laserbeschleunigung von Ionenstrahlen. Basierend auf theoretischen Simulationen demonstrieren wir die Realisierbarkeit von Laser-generierten Ionenstrahlen, welche die strengen Kriterien radio-onkologischer Anwendungen erfüllen. Teilchenenergien von mehreren hundert MeV und einer niedrigen Energiestreuung von 1 % sind im Rahmen direkter Laserbeschleunigung erzeugbar. Wir schlagen einen Mechanismus vor, um Teilchenstrahlen, die aus Laser-Plasma-Wechselwirkungsprozessen stammen, effizient nachzubeschleunigen, wobei die Injektion der Teilchen in den Fokus realistisch modelliert wird. Die Einführung eines langwelligen CO_2-Lasers führt zu einem Anstieg in der Gesamtzahl an beschleunigten Teilchen pro Bündel, der um drei Größenordnungen höher ist verglichen zu Lasern mit Wellenlängen um 1 μm. Durch Anwendung gepulster Lasersysteme in unterschiedlichen Strahlenkonfigurationen (einzeln oder zwei gekreuzte Strahlen), zeigen wir, dass Ionenstrahlen mit hoher Teilchenzahl erzeugt werden können. In einem anderen Schema stellen wir, basierend auf Particle-In-Cell-Simulationen, die Wechselwirkung eines gechirpten Laserpulses mit einem Wasserstoffgastarget vor, dessen räumliche Ausdehnung vergleichbar mit der Laserwellenlänge ist. Die niedrigfrequenten Komponenten des Laserpulses ermöglichen es, bereits durch die Wechselwirkung mit modernsten Lasersystemen mit Intensitäten von 10^{21} W/cm^2 klinisch anwendbare Teilchenstrahlen zu erzeugen.

Abstract

The advent of high-power laser systems paved the way for laser acceleration of ion beams. Based on theoretical simulations, we demonstrate the feasibility of laser-generated ion beams matching the strict requirements for radio-oncological applications. Particle energies of several hundred MeV and low energy spreads of 1% are feasible within the framework of direct laser acceleration. A mechanism is suggested to efficiently post-accelerate particle beams originating from laser-plasma interaction processes, where the injection of ions into the focus is modeled in a realistic way. Introducing a long-wavelength CO_2 laser leads to an increase in the total number of particles accelerated as one bunch by three orders of magnitude as compared to lasers with a wavelength around 1 μm. By employing pulsed laser systems in a single- and a crossed-beams configuration, we show that ion beams of high particle numbers can be produced. In a different setting we put forward the interaction of a chirped laser pulse with a hydrogen gas target of spatial extension of the order of the laser wavelength studied by means of particle-in-cell simulations. The low frequency components of the laser pulse allow for generating clinically applicable beams already while interacting with state-of-the-art laser systems of intensities of 10^{21} W/cm^2.

Within the scope of this thesis, the following articles have been published in peer-reviewed journals:

- Benjamin J. Galow, Zoltán Harman, and Christoph H. Keitel,
  "Intense high-quality medical proton beams via laser fields,"
  Opt. Express **18**, 25950-25957 (2010)

- Benjamin J. Galow, Yousef I. Salamin, Tatyana V. Liseykina, Zoltán Harman, and Christoph H. Keitel,
  "Dense Monoenergetic Proton Beams from Chirped Laser-Plasma Interaction,"
  Phys. Rev. Lett **107**, 185002 (2011)
  (See also: "Hochwertige energiereiche und dichte Ionenstrahlen durch Laserbeschleunigung", press release of the Max Planck Institute for Nuclear Physics, `http://www.idw-online.de/pages/de/news449697`)

- Zoltán Harman, Yousef I. Salamin, Benjamin J. Galow, and Christoph H. Keitel,
  "Optimizing direct intense-field laser acceleration of ions,"
  Phys. Rev. A **84**, 053814 (2011)

Article in preparation:

- Benjamin J. Galow, Zoltán Harman, and Christoph H. Keitel,
  "Direct strong-field laser acceleration of ions from underdense plasmas"

Contents

Chapter 1

Introduction

Albert Einstein's contributions to physics are invaluable. While it is of general knowledge that he is the father of the theory of relativity, it is less known that already in 1917 he formulated the fundamental concept of the laser in his rate equation model of stimulated and spontaneous emission of light [1]. More than four decades later, in 1960, the technical realization of the laser [2] heralded a new era of technology and fundamental research. At the beginning of the 1970s the rapid advancement of laser systems and their peak intensities was suddenly interrupted, when the laser intensities became so extraordinarily strong to cause severe damage to the gain medium. This barrier was bypassed by Strickland and Mourou in the mid-1980s [3] by stretching a laser pulse in time, letting it pass through a gain medium and subsequently recompressing it. The underlying technique is called Chirped Pulse Amplification (CPA) [4] on which any modern laser system relies. Only about 20 years later, lasers with a peak intensity as high as 10^{22} W/cm^2 at a repetition rate of 0.1 Hz have been realized [5]. Future facilities such as the Extreme Light Infrastructure (ELI) [6] will even reach laser intensities in the excess of 10^{24} W/cm^2 employing short pulses of a duration of a few laser cycles and being focused to the order of the laser wavelength at an output power of several petawatts. At the projected High Power laser Energy Research (HiPER) facility [7], lasers of several hundred kilojoule output energy will be realized. For a review on the interaction of high-power lasers with matter, we refer to [8, 9] and for short-pulse attosecond physics to [10].

The feasibility of creating ultra-intense laser pulses did not only stimulate the birth of a striking diversity of fundamental research but also let emerge potential applications of paramount importance and far-reaching consequences to society: Strong electric fields of the order of 10^{12} V/m involved in high-intensity laser pulses can be utilized to accelerate charged particles. Particle accelerators aiming at exploring the smallest structures of the universe have undergone an impressive development during the past fifty years, which is culminated in the Large Hadron Collider (LHC) [11] being often referred to as "the world's largest science experiment" [12]. At the LHC, the limit of the underlying synchrotron technique is reached. For protons being accelerated to

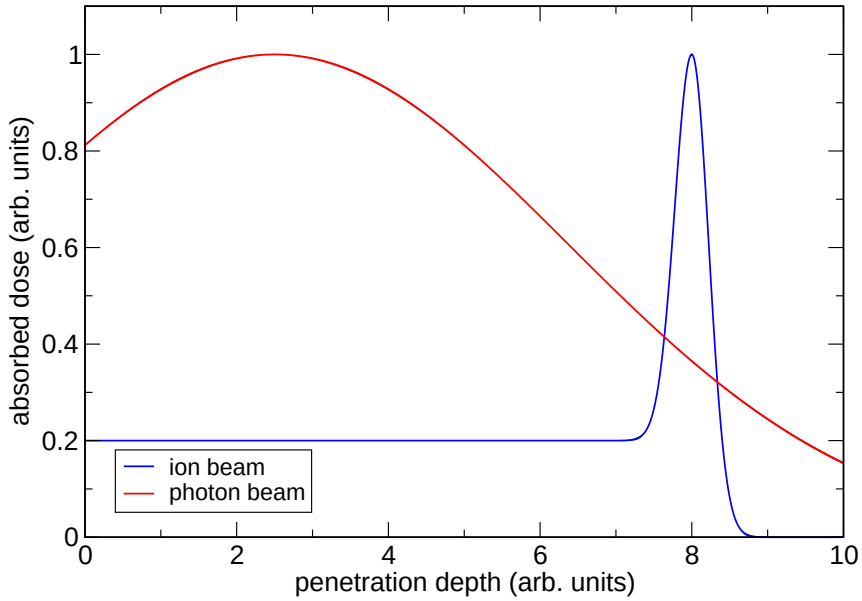

Figure 1.1 – Schematic illustration (adapted from Fig. 1 of Ref. [19]) of the absorption of radiation in tissue.

an energy of 7 TeV which corresponds to almost the speed of light, the energy loss due to synchrotron radiation prevents the particles from gaining further energy. Hence, alternative methods to accelerate charged particles such as laser acceleration are indispensable and may lead to a drastic reduction in size for high-performance accelerators. Moreover, medical applications would greatly benefit from more compact accelerators.

Recently, the Heidelberg Ion beam Therapy center (HIT) [13, 14] went online utilizing accelerated ion beams to treat deep-seated malign tumors, e.g. tumors located at the skull base [15–18]. The advantage of using ion beams over conventional gamma rays has its origin in the absorption behavior of radiation in matter: Photons continuously loose their energy while penetrating a tissue (see red curve Fig. 1.1) and hence damage both, healthy as well as malign cells. In contrast, ion beams deposit most of their energy at a characteristic penetration depth, the so-called Bragg peak (see peak around the penetration depth of 8 units in the blue curve, Fig. 1.1). The characteristic penetration depth depends on the initial kinetic energy of the ion beam. To irradiate a tumor of specific thickness, one superposes ion beams of different energy. For detailed information, such as the biological effectiveness of several ion species we refer to [19]. Hadron cancer therapy comes along with strict requirements for the ion beams:

1. Sufficient kinetic energies (>200 MeV) to be able to treat deep-seated tumors.

2. Sharp enough energy spread (≈1%) to spare the healthy tissue.

3. High enough proton flux ($> 10^6$ protons/bunch at a 5-Hz repetition rate) to keep the treatment cycles acceptably short.

Due to the demanding requirements for the accelerated beams, a large percentage of the total costs of a facility such as HIT [14], which amount to 119,000,000 EUR [14], is spent on the synchrotron and its concrete shieldings. Furthermore, in order to irradiate the patients from all angles, a huge gantry with a total weight of 670 tons is necessary [14]. This enormous cost factor could be drastically reduced by the adoption of compact laser-based accelerators, which may allow for much simpler beam guidance. Interesting conceptual design studies of potential laser-based accelerators for medical applications have been carried out. J. Weichsel et al. [20] propose an optical gantry, such that the ion beams created by laser-matter interaction could be generated close to the patient, making a complex beam guidance dispensable. Of course, present lasers in the PW domain are still quite expensive and relatively large. For example, the Apollon beamline, a prototype of one of the beamlines of the ELI project, is expected to operate at a power of 10 PW with a projected cost of 25,000,000 EUR; the Vulcan upgrade [21] at Rutherford Appleton Laboratory (RAL) in the UK will also operate at 10 PW, with a cost of 25,000,000 GBP. However, a substantial decrease in price and size is likely by means of, e.g., optical parametric chirped-pulse amplification (OPCPA) [22] within a few years.

Long before the availability of high-intensity laser systems the dynamics of an electron in a strong laser field has already been studied theoretically [23–25]. Even for a plane wave multiplied with a temporal pulse envelope, the dynamics still can be solved by analytical means. This particular solution offers an important insight: After the electromagnetic pulse passed by an electron initially being at rest, it returns to rest (for details see Sect. 3.1 of [26]). The so-called Lawson-Woodward theorem [27,28] generalizes this finding: A charged particle cannot extract net energy from an electromagnetic plane wave. How can charged particles then be accelerated by lasers? The answer is given by the non-uniformity of the intensity distribution of a focused laser following a Gaussian profile [29] and thus the Lawson-Woodward theorem does not apply. In particular, high-intensity lasers need to be strongly focused. Additionally, a point charge exposed to such a laser field feels a non-vanishing average force, the (relativistic) ponderomotive force [30].

During the past two decades, a multitude of interesting schemes has been proposed to directly accelerate charged particles interacting with strong laser fields. Early work on electron acceleration [31,32] already indicated promising energy gain gradients of several GeV/m, outperforming classical synchrotron facilities by orders of magnitude. For tightly focused laser beams of a waist radius of only few laser wavelengths it was theoretically predicted [33,34] that electrons of GeV energies are possible after ejection out of the micron-size focal area. An electron shot from outside into the focal region of the laser beam may experience three different scenarios [33]: If its initial energy is too low, it will be reflected or scattered off the laser beam. Too high initial velocity will lead

to a transmission through the laser beam and finally for a favorable initial kinetic energy the electron is captured and accelerated (Capture and Acceleration Scenario (CAS) [35,36]). The transverse electric field together with the longitudinal magnetic field confine the particle while the axial electric component accelerates it [8]. Further, more involved schemes have been suggested, e.g. to inject a particle into the focus of two crossed beams [31,32,37,38] or to let a particle interact with a beat wave (Vacuum Beat Wave Laser Accelerator (VBWLA)) created by the superposition of two laser waves of slightly different frequencies [32,39,40]. The latter uses the increased field amplitude of the beat wave, yielding an increase of the energy gain. Furthermore it was demonstrated via classical Monte-Carlo simulations that GeV electrons [41] can be created from highly charged ions. The underlying mechanism is that ionization take places at the peak intensity of the incident laser beam leading to efficient energy gain. Another interesting scheme is called autoresonant laser acceleration [42]. Due to a strong static external magnetic field an electron submitted to the laser wave undergoes cyclotron motion. If the cyclotron frequency of the electron coincides with the laser frequency, huge energy gains may be realized.

Besides the so-called direct- or vacuum acceleration schemes, another branch of laser-induced particle beam creation arose. In 1979, Tajima and Dawson [43] presented the idea of exciting a neutral plasma by an electromagnetic wave. The concept of laser-wakefield acceleration was born: An electromagnetic wave entering a plasma displaces the much lighter electrons from the ions, leaving an area of huge space charge, pulling back the electrons and causing a plasma oscillation, the so-called wake. Electrons may be trapped and co-propagate in phase with the wake resulting into considerable energy gain. This has been confirmed experimentally [44–46] and even monoenergetic electron beams have been measured in the meantime [47]. Later, a proton-beam-driven plasma wakefield accelerator allowing for TeV-electrons was proposed [48].

Experiments utilizing high-intensity lasers to interacting with solid targets opened up the door of laser-plasma-based ion acceleration. Different regimes for laser-plasma ion acceleration exist [9]. For laser intensities of $10^{18}-10^{21}$ W/cm^2 and solid targets with a thickness ranging from a few to tens of micrometers, Target Normal Sheath Acceleration (TNSA) is the prevailing mechanism [49]. In TNSA, a strong quasi-static electric field (often referred to as the "virtual cathode") is induced at the rear surface of the target, as a result of emission and acceleration of the electrons caused by an intense linearly polarized laser field. Ion acceleration, by the sheath electric field, has been extensively studied in [50–58]. A similar laser-plasma-interaction process, the Skin-Layer Ponderomotive Acceleration (S-LPA) resulting from the huge electric potential gradient of a thick plasma slab at the laser-irradiated side leads to slow (keV) ion beams of high density [59]. The regime of Radiation-Pressure-Dominant Acceleration (RPA), has become accessible recently by decreasing the target thickness [49]. Circularly polarized lasers at normal incidence have been employed, which suppress electron heating and let all particle species co-propagate as a quasi-neutral plasma bunch in front of the light wave ("light sail"-mechanism) [49, 60]. Despite recent experimental [49] and theoretical [61] progress, clinically useful ion

beams [13] have not yet been produced within any of those schemes.

In this thesis we demonstrate the creation of laser-induced ion beams fulfilling the challenging criteria of hadron cancer therapy (as mentioned above) based on theoretical simulations. Starting point of our investigations in Chapter 2 is the direct acceleration of an ensemble of ions [62] exposed to tightly focused laser fields, being either linearly [63] or radially [64, 65] polarized. The mechanism of acceleration is demonstrated and explained on the basis of the relativistic equations of motion of an ensemble of charged particles in strong laser fields. We investigate dependence of the accelerated particle beam properties, e.g., the exit kinetic energy distribution, the number of particles accelerated, on such laser system parameters as wavelength, power and waist radius. It is shown that the ions gain kinetic energies of several hundred MeV/nucleon, while interacting with laser beams with powers of the order of $0.1-10$ petawatt.[1] Additionally, the accelerated ion beams have an energy spread of about 1%[1]. In the simulations of Chapter 2, we use CO_2 lasers which have a wavelength of 10.6 μm. Due to the cubic dependence of the focal volume on the laser wavelength, about three orders of magnitude more particles can be accelerated than with titan-sapphire lasers of 1.054 μm wavelength, used e.g. in Ref. [62].

Whereas in Chapter 2 the source of the particle ensemble remains untreated, we resolve this issue in Chapter 3. Herein, we simulate the injection of a particle ensemble originating from laser-plasma processes such as the above-mentioned TNSA or S-LPA mechanism into an approaching Gaussian laser pulse. The initial velocity distributions of the particle ensembles coincide with the ones of the underlying plasma source [59]. The role of potential particle-particle interaction effects is investigated based on the coupled Lorentz-Newton equations of motion for a particle test ensemble at typical ion densities applied later on. The model includes relativistic effects on the ion-ion interaction to second order in the scaled velocity $\beta = v/c$ (with v being the typical particle velocity). Our simulations clearly demonstrate that in this realistic scenario the proton beam properties of Chapter 2 can be maintained. The simulations are carried out not only for a single laser beam but also for two crossed laser beams (originally introduced for electrons [31, 32, 37, 38]). Due to the coherent superposition of two laser beams, higher exit kinetic energies can be achieved. It should be emphasized that we do reach the proton flux threshold necessary for broader radio-oncological application. To our knowledge, this is the first scheme fulfilling all criteria for hadron cancer therapy based on an all-optical set-up.

So far we considered laser vacuum acceleration schemes. In Chapter 4 we study the interaction of a frequency-chirped laser beam [66–68] with a hydrogen plasma target. The numerical simulations are performed within the framework of Particle-In-Cell (PIC) simulations (cf. Ref. [69] for a review). This method allows to solve the many-body dynamical problem of an electromagnetic plasma in a fully relativistic treatment. The basic idea of our model stems from the realization that an incoming highly relativistic laser pulse quickly ionizes the

[1] Similar results have been demonstrated in [62] for a different laser wavelength.

hydrogen atoms in the target and accelerates the electrons away from the much heavier protons, as the pulse intensity rises. At high enough laser intensities the protons get accelerated directly by the laser field. We derive an expression for the energy transfer during interaction of a particle with chirped unfocused as well as pulsed electromagnetic fields. The results indicate the feasibility of generating intense (10^7 particles per bunch) and phase-space collimated beams of protons (energy spread of about 1%). The low-frequency components of the applied laser pulse, guaranteed by the appropriate chirping of the laser frequency, allow the particles to gain sufficient kinetic energy (around 250 MeV per particle) for hadron cancer therapy. The required laser intensities of the order of 10^{21} W/cm^2 fall in the range of state-of-the-art laser systems [5]. Furthermore, we show that applying this scheme very collimated beams with a divergence angle of only 2° may be created. Eventually we give a brief summary and an outlook in Chapter 5.

Chapter 2

Direct intense-field laser acceleration of ions

The dynamics of ion acceleration in tightly focused laser beams is investigated in relativistic simulations. Studies are performed to find the optimal parameters which maximize the energy gain, beam quality and flux. The exit ionic kinetic energy and its uncertainty are improved and the number of accelerated particles is increased by orders of magnitude in comparison with [62], especially when working with a longer laser wavelength. Laser beams of powers of the order of 0.1−10 petawatt and focused to sub-wavelength spot radii are shown to directly accelerate protons and bare nuclei of helium, carbon, and oxygen from a few to several hundred MeV/nucleon. Variation of the volume of the initial ionic ensemble, as well as the introduction of a pulse-shape on the laser fields, have been investigated. Large parts of this Chapter have been published in [70]. The underlying article has been written predominantly by the co-authors Z. Harman and Y. I. Salamin.

2.1 Introduction

In this Chapter we present results of theoretical studies in which laser light is the source of energy to directly accelerate ions produced by other means. These particles gain substantial energy when subjected to present-day petawatt power laser systems, capable of generating electric fields several orders of magnitude stronger than the field of the proton at the site of the electron in a hydrogen atom (defining the atomic unit of electric field). The mechanism of acceleration is demonstrated and explained on the basis of the relativistic equations of motion of an ensemble of charged particles in strong laser fields. We investigate dependence of the accelerated particle beam properties, e.g., the exit kinetic

energy distribution, the number of particles accelerated, on such laser system parameters as wavelength, power and waist radius.

We want to determine the optimal range of parameters. We find that the number of accelerated ions can be increased by orders of magnitude compared to earlier vacuum acceleration results [62, 71] by increasing the laser wavelength by one order of magnitude. Furthermore, the energy gain of ions and its spread are improved by increasing the wavelength of the laser field. This can be experimentally achieved, e.g., by using CO_2 lasers of a wavelength of 10.6 μm [72], rather than near-infrared lasers with wavelengths around 1 μm. Simulations in this chapter demonstrate energy gains by protons and helium, carbon and oxygen nuclei of up to several hundred MeV/nucleon as a result of interaction with linearly and radially polarized laser beams. These gains may be achieved even using a multi-terawatt laser system, provided it is focused to a sub-wavelength waist radius. Focusing beams of multi-terawatt or petawatt powers to μm spot sizes yields laser intensities of the order of 10^{20}–10^{23} W/cm^2, which defines the range of interest. In radiotherapy, employing heavier ions, the required energies fall in the range 20−580 MeV/nucleon with less than 1% energy fluctuations [73].

This Chapter is organized as follows. In Section 2.2 the linearly and radially polarized fields of a tightly focused laser beam will be reviewed. Section 2.3 will be devoted to outlining the main single-particle equations and method of their solution, while the simulations will be described in Section 2.4. Simulations for acceleration of nuclei by linearly- and radially-polarized laser beams will be carried out and their results discussed in sections 2.5 and 2.6, respectively. In Section 2.7, effects of the size of the initial particle ensemble, and an added pulse-shape to the laser fields, on the kinetic energies of the accelerated particles, will be investigated and discussed. Our conclusions will be summarized in Section 2.8.

2.2 The laser fields

In this Section a derivation[1] of the fields of the laser beams will be outlined based on Ref. [63] for linearly polarized light and on Ref. [64, 65, 71, 74] for radially polarized light, respectively. First of all, it should be recalled that the tightly focused beams develop axial as well as transverse electric and magnetic components. Tight-focusing, to a waist radius $w_0 < \lambda$, also calls for a more accurate description of the fields beyond what is familiar from the paraxial approximation. The corresponding laser power and intensity expressions ought also to be described to the same level of accuracy. For both linear and radial polarization, the parameters of a Gaussian beam will be used to model the fields. Those are the beam waist radius w_0, the Rayleigh length (or depth

[1]Section 2.2 is a purely reproductive part based on the given references. It contains no own results.

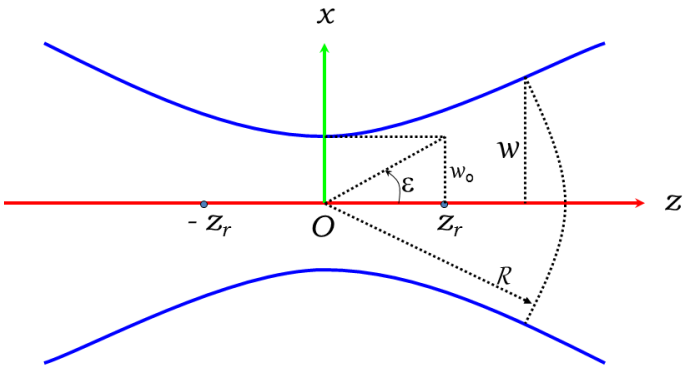

Figure 2.1 – Sketch [75] of Gaussian beam geometry.

of focus) $z_r = \pi w_0^2/\lambda$, where λ is the wavelength, and the diffraction angle $\varepsilon = w_0/z_r = \lambda/(\pi w_0)$. For a sketch of the beam geometry, we refer to Fig. 2.1.

2.2.1 Linear polarization

Let us start with a derivation of the linearly polarized electric and magnetic field components used for the simulations carried out below. The basic idea is to solve the wave equation as a power series in the diffraction angle squared ε^2. First, this was done for the so-called paraxial approximation (up to $\mathcal{O}(\varepsilon^2)$) [29]. Then the series was extended to $\mathcal{O}(\varepsilon^5)$ [76] and eventually to $\mathcal{O}(\varepsilon^{11})$ [63]. The latter reference will serve as the guideline for the brief derivation and we refer to it for details. The wave equation for the vector potential reads (SI units)

$$\nabla^2 \boldsymbol{A} = \frac{1}{c^2}\frac{\partial^2 \boldsymbol{A}}{\partial t^2}, \tag{2.1}$$

which is linked to the scalar potential ϕ via the Lorentz condition

$$\nabla \cdot \boldsymbol{A} + \frac{1}{c^2}\frac{\partial \phi}{\partial t} = 0. \tag{2.2}$$

After solving the wave equation, the electromagnetic field components may be obtained via the well-known relations

$$\boldsymbol{E} = -\nabla\phi - \frac{\partial \boldsymbol{A}}{\partial t}, \tag{2.3}$$

$$\boldsymbol{B} = \nabla \times \boldsymbol{A}. \tag{2.4}$$

In order to solve Eq. (2.1), one can make the following ansatz which factorizes the vector potential in a phase-dependent term and a coordinate-dependent one (ψ) (Cartesian coordinates are assumed):

$$\boldsymbol{A}(x,y,z,t) = \boldsymbol{e}_x A_0 \psi(x,y,z) e^{i(\omega t - kz)} \tag{2.5}$$

Here, A_0 is a constant factor and the laser field is assumed to be polarized along the x-direction and propagating along the z-direction. Plugging this ansatz into the wave equation yields the following equation for ψ:

$$\nabla^2 \psi - 2ik\frac{\partial \psi}{\partial z} = 0. \tag{2.6}$$

For further simplification a coordinate rescaling is reasonable

$$\xi = \frac{x}{w_0}, \quad v = \frac{y}{w_0}, \quad \zeta = \frac{z}{z_r}, \quad \rho^2 = \xi^2 + v^2. \tag{2.7}$$

Using these definitions, Eq. (2.6) reads

$$\nabla_\perp^2 \psi - 4i\frac{\partial \psi}{\partial \zeta} + \varepsilon^2 \frac{\partial^2 \psi}{\partial \zeta^2} = 0, \tag{2.8}$$

where we introduced the transverse Laplacian operator

$$\nabla_\perp^2 \equiv \frac{1}{\rho}\frac{\partial}{\partial \rho}\left(\rho \frac{\partial}{\partial \rho}\right). \tag{2.9}$$

The appearance of the typically small parameter ε^2 in Eq. (2.8) suggests it as an expansion parameter for ψ, i.e.,

$$\psi = \sum_{n=0}^{\infty} \varepsilon^{2n} \psi_{2n}. \tag{2.10}$$

This turns Eq. (2.8) into

$$\nabla_\perp^2 \psi_0 - 4i\frac{\partial \psi_0}{\partial \zeta} = 0 \quad (n = 0), \tag{2.11}$$

$$\nabla_\perp^2 \psi_{2n} - 4i\frac{\partial \psi_{2n}}{\partial \zeta} + \frac{\partial^2 \psi_{2n-2}}{\partial \zeta^2} = 0 \quad (n \geq 1). \tag{2.12}$$

The solution of these equations, giving the field components E_x, E_y, E_z, B_y and B_z to order ε^{11} in the diffraction angle, may be found in [63]. We quote here only the leading couple of terms in each component, for the sake of the useful discussions to be presented below. With $\mathcal{O}(\varepsilon^n)$ meaning the last term to be

included in the component in question is of order ε^n, where n =10 or 11, the field components may be written as

$$\begin{aligned}
E_x &= E\left\{S_1+\varepsilon^2\left[\xi^2 S_3-\frac{\rho^4 S_4}{4}\right]+\cdots+\mathcal{O}(\varepsilon^{10})\right\}, && (2.13)\\
E_y &= E\xi\upsilon\left\{\varepsilon^2\left[S_3\right]+\cdots+\mathcal{O}(\varepsilon^{10})\right\}, && (2.14)\\
E_z &= E\xi\left\{\varepsilon\left[C_2\right]+\cdots+\mathcal{O}(\varepsilon^{11})\right\}, && (2.15)\\
B_x &= 0, && (2.16)\\
B_y &= \frac{E}{c}\left\{S_1+\varepsilon^2\left[\frac{\rho^2 S_3}{2}-\frac{\rho^4 S_4}{4}\right]+\cdots+\mathcal{O}(\varepsilon^{10})\right\}, && (2.17)\\
B_z &= \frac{E}{c}\upsilon\left\{\varepsilon\left[C_2\right]+\cdots+\mathcal{O}(\varepsilon^{11})\right\}. && (2.18)
\end{aligned}$$

With ω the angular frequency of the fields, $\psi_G=\tan^{-1}\zeta$, and $r=\sqrt{x^2+y^2}$, $\rho=r/w_0$, the remaining variables in Eqs. (2.13)-(2.18) have the following definitions

$$\begin{aligned}
E &= E_{0l}e^{-r^2/w^2};\quad w=w_0\sqrt{1+\zeta^2}, && (2.19)\\
C_n &= \left(\frac{w_0}{w}\right)^n\cos(\psi+n\psi_G);\quad n=1,2,3,\cdots, && (2.20)\\
S_n &= \left(\frac{w_0}{w}\right)^n\sin(\psi+n\psi_G), && (2.21)
\end{aligned}$$

where

$$\psi=\psi_0+\omega t-kz-\frac{kr^2}{2R};\quad R=z+\frac{z_r^2}{z}, \qquad (2.22)$$

and ψ_0 is a constant initial phase. Also, t is the time and $k=2\pi/\lambda$ is the wavenumber. E_{0l} is the amplitude of the linearly polarized laser field. Note that the definitions of some quantities differ slightly from [8]. On the other hand the corresponding power expression may be given, to the same order in ε as the field components, by

$$\begin{aligned}
P_l &= \frac{\pi w_0^2}{4}\frac{E_{0l}^2}{c\mu_0}\left[1+\left(\frac{\varepsilon}{2}\right)^2+2\left(\frac{\varepsilon}{2}\right)^4+6\left(\frac{\varepsilon}{2}\right)^6\right.\\
&\quad\left.+\frac{45}{2}\left(\frac{\varepsilon}{2}\right)^8+\frac{195}{2}\left(\frac{\varepsilon}{2}\right)^{10}\right], && (2.23)
\end{aligned}$$

where c is the speed of light in vacuum, μ_0 is the permeability of free space (cf. [63] for details). It should be emphasized that $E_{0l}\propto\sqrt{P_l}$ and that the leading term in E_{0l} is inversely proportional to w_0 [62].

2.2.2 Radial polarization

Since focusing to a waist radius $w_0<\lambda$ is crucial for achieving the high energy gains we have in mind [62], it is natural to seek for modes of a Gaussian beam that may be focused to the tightest spot possible. It has recently been shown [77–79] that a (low-intensity) radially polarized beam may be focused

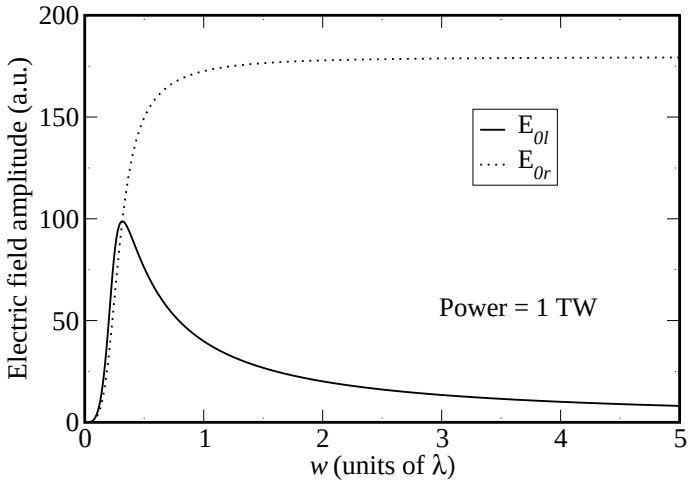

Figure 2.2 – Laser field strength at focus (E_{0l} for linear polarization and E_{0r} for radial polarization) as a function of the waist radius at focus.

down to a spot size $(0.16\lambda)^2$. This is better than the spot size of $(0.26\lambda)^2$ achieved for a linearly polarized beam. The spot size is defined as the area enclosed by a contour at which the beam intensity corresponds to the half of its peak value [62]. Radially polarized fields are also referred to axicon beams.

The only components of the electric field of a radially polarized laser beam are the radial component E_r and the axial component E_z. In addition to that only one magnetic field component, B_θ, which is azimuthal, exists. As will be demonstrated below, E_z works efficiently to accelerate the particles [62].

The derivation of the radial field components is identical to the one for linear polarization up to the fact that one starts with assuming cylindrical symmetry and coordinates for the vector potential:

$$\boldsymbol{A}(r,\theta,z,t) = \boldsymbol{e}_z A_0 \psi(r,z) e^{i(\omega t - kz)} \tag{2.24}$$

Here, the laser propagation direction and its alignment are both along the z-axis. For further details the reader will be directed elsewhere [64, 65, 71, 74] for the full expressions, in terms of the Gaussian beam parameters, of the fields of the radially-polarized beam. We quote here, too, only the leading terms of the field components

$$E_r = E\left\{\varepsilon\rho C_2 + \cdots + \mathcal{O}(\varepsilon^{11})\right\}, \tag{2.25}$$

$$E_z = E\left\{\varepsilon^2\left[S_2 - \rho^2 S_3\right] + \cdots + \mathcal{O}(\varepsilon^{10})\right\}, \tag{2.26}$$

$$B_\theta = \frac{E}{c}\left\{\varepsilon\rho C_2 + \cdots + \mathcal{O}(\varepsilon^{11})\right\}. \tag{2.27}$$

On the other hand, the power expression of the axicon beam, to order ε^{10}, takes

on the following form

$$P_r = \frac{\pi w_0^2}{2}\frac{E_{0r}^2}{c\mu_0}\left(\frac{\varepsilon}{2}\right)^2\left[1+3\left(\frac{\varepsilon}{2}\right)^2+9\left(\frac{\varepsilon}{2}\right)^4 +30\left(\frac{\varepsilon}{2}\right)^6+\frac{225}{2}\left(\frac{\varepsilon}{2}\right)^8\right]. \tag{2.28}$$

We want to emphasize here, too, that the radially polarized electric field amplitude $E_{0r} \propto \sqrt{P_r}$ [62]. Furthermore, the leading term in E_{0r} turns out to be independent of w_0, when plugging in $\varepsilon = w_0/z_r$. The dependence upon w_0 of the field strength is shown in Fig. 2.2. Note that, whereas the linearly polarized field strength attains a maximum value beyond which it falls down with increasing waist radius, the radially polarized strength increases steadily to an asymptotic constant value (cf. [62, 65]).

2.3 Single-particle trajectory calculations

In this Section the theory of our calculations will be briefly outlined. Motion of a single particle of mass M and charge Q in the electric and magnetic fields $\boldsymbol{E}$ and $\boldsymbol{B}$, respectively, of a laser beam will be considered classically, and relativistically. The use of laser systems of high-intensity (in excess of 10^{18} W/cm^2) leads to relativistic particle dynamics. Thus the dynamics will be governed by the Lorentz-Newton (or energy-momentum transfer) equations (SI units) [62, 80] including the external electromagnetic fields

$$\frac{d\boldsymbol{p}}{dt} = Q[\boldsymbol{E} + c\boldsymbol{\beta}\times\boldsymbol{B}]; \quad \frac{d\mathcal{E}}{dt} = Qc\boldsymbol{\beta}\cdot\boldsymbol{E}. \tag{2.29}$$

The relativistic energy of the particle is given by $\mathcal{E} = \gamma Mc^2$ and its momentum by $\boldsymbol{p} = \gamma Mc\boldsymbol{\beta}$, respectively. $\boldsymbol{\beta}$ is the velocity scaled by c, and $\gamma = (1-\beta^2)^{-1/2}$ is the Lorentz factor. Out of many single-particle dynamical aspects, we are mainly interested in the energy gained by the particle as a result of interaction with a laser beam. Here we first restrict ourselves to continuous fields. The case of pulsed lasers, which are able to produce the high powers needed, is treated in Section 2.7. To arrive at the energy gain, numerical solutions to the equations above will be sought. In most cases of practical utility, a solution proceeds along the following lines. First, the two equations are combined to give [71]

$$\frac{d\boldsymbol{\beta}}{dt} = \frac{Q}{\gamma Mc}\left[(\boldsymbol{E} + c\boldsymbol{\beta}\times\boldsymbol{B}) - \boldsymbol{\beta}(\boldsymbol{\beta}\cdot\boldsymbol{E})\right]. \tag{2.30}$$

Then, in principle, a numerical integration of Eq. (2.30) yields $\boldsymbol{\beta}$ and as a consequence γ_f at a later time t_f [62]. This time equates to many laser field cycles such that one ensures that laser-particle interaction is finished. Finally, one calculates the energy gain [8] of the particle from

$$G = (\gamma_f - \gamma_i)Mc^2, \tag{2.31}$$

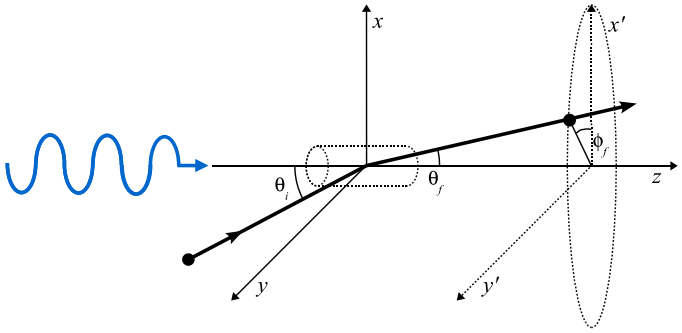

Figure 2.3 – A schematic diagram showing the geometry of laser acceleration of nuclei. θ_i and θ_f represent the injection and the ejection angle of the particles, respectively.

where $\mathcal{E}_i = \gamma_i Mc^2$ is the initial (injection) energy.

Energy carried by an optical photon of wavelength $\lambda \sim 1\mu$m is of the order of 1 eV, much smaller than a typical nuclear excitation energy. So, barring multi-photon absorption, these charge states remain intact in, and get accelerated by, the strong electromagnetic fields of present-day laser intensities already in excess of 10^{22} W/cm^2. It should be noted that, with the applications in mind, we treat the acceleration of bare nuclei; the behavior of ions which are not fully stripped may be more complex due to strong-field ionization processes.

The procedure outlined above has been used to study acceleration of electrons by linearly polarized laser fields [33]. The same procedure has been followed recently in investigating possible acceleration of electrons by radially polarized laser fields [71]. In the latter calculations, however, single-particle dynamics only were emphasized and a set of artificial initial conditions (rest at the origin of coordinates) was used in most cases. From the single-particle calculations one learns that electron laser acceleration to GeV energy is possible. As it has been explained [32, 33], the use of focused fields circumvents the Lawson-Woodward theorem [27, 28] which predicts zero net acceleration in the case of an infinite plane wave. Study of individual particle trajectories showed that most of the energy gain takes place during interaction with a small number of laser field cycles. In addition to that, the role of laser focusing has been thoroughly discussed. Dependence of the gain on the initial phase ψ_0 of the fields was also demonstrated. Maximum gain from high-intensity laser fields required that the particles be injected into the focal region at space-time points corresponding to the neighborhood of some specific value of ψ_0 allowing the particles to surf on the laser waves and gain energy from them. Failing to meet the conditions of the right value of ψ_0 results in phase-slippage and can even lead to deceleration. An optimum ψ_0 value has to be determined for each set of initial conditions, particle charge, laser polarization and laser power. For example, for particles released from rest near the beam focus (and origin of coordinates) maximum gain may be obtained from radially polarized fields for $\psi_0 \approx \pi$, for negatively charged entities, and $\psi_0 \approx 0$ for positively charged ones.

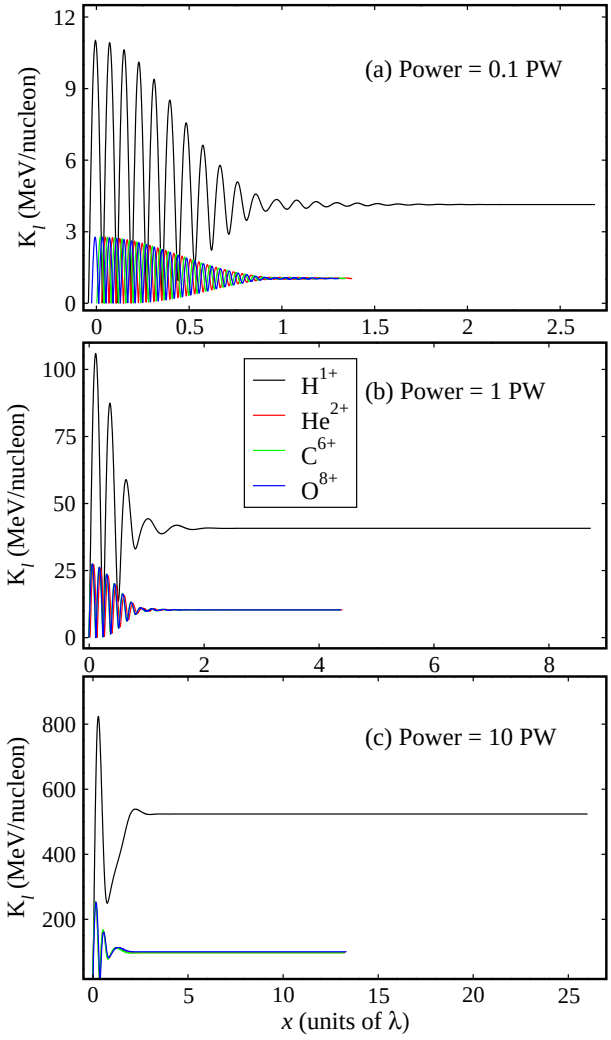

Figure 2.4 – Evolution of the kinetic energies of four nuclear species in linearly polarized laser fields as functions of their excursion distances along the laser propagation direction (cf. Fig. 3 of [62] calculated at shorter λ and as function of laser cycle T). The laser wavelength is $\lambda = 10.6$ μm and the beam waist radius at focus is $w_0 = 0.48\lambda$. The given powers (0.1, 1 and 10 PW) correspond to peak intensities $I \sim 2.14 \times 10^{20}$, 2.14×10^{21} and 2.14×10^{22} W/cm^2, respectively. The injection angle is $\theta_i = 10^\circ$ for all particles. Integration of the equations of motion was carried out over a range of values $\Delta\eta = 60\pi$ of the variable $\eta \equiv \omega(t - z/c)$.

These values correspond to space-time points at which the particle is initially subjected to the accelerating field minimum.

This Chapter is about laser acceleration of bare nuclei (recently done by [71]). We wish to develop the study of direct laser acceleration of an ensemble of bare nuclei consisting of a large set of initial positions and momenta of the particles like it was done in [62] (the methods are adopted from this reference) and employing the most accurately-represented fields [63, 71] as introduced in the previous Section.

An approximate value for the magnitude of energy gain that may be achieved using present-day laser systems, can be obtained from estimate formulas. Consider a nucleus of charge $+Ze$, where Z is the atomic number, near the focus of a linearly polarized laser beam, itself the origin of coordinates. According to Eqs. (2.13)-(2.18), the fields are transverse near the focus, with E_x and B_y being the only non-vanishing components. So, together with the magnetic force, the force due to E_x will act to accelerate the nucleus. An approximate expression for the energy gain may then be obtained from the second of Eqs. (2.29) which now reads $d\mathcal{E}/dt \approx Qc\beta_x E_x$. Taking $\beta_x \sim 1$, an exaggeration that will result in the final expression overestimating the gain, and recognizing that in this limit, $E \sim E_0$ and $S_1 \sim \sin(\omega t)$, the approximate equation may now be formally integrated with respect to time. The final result will then yield the following approximate expression for the maximum gain per nucleon, in MeV, when the laser power is given in terawatt (TW)

$$G_l[\text{MeV/nucleon}] \sim \frac{2Z}{A}\left(\frac{\lambda}{\pi w_0}\right)\sqrt{30P_l[\text{TW}]}, \tag{2.32}$$

where A is the atomic number and the field strength E_{0l} has been replaced by its value from the leading term in the power expression (2.23). As an example, a nucleus of $^{12}_{6}$C, or any nucleus having the same charge-to-mass ratio $Z/A = 0.5$, will gain approximately 3.63 MeV/nucleon from a 1 TW laser focused to a waist radius $w_0 = 0.48\lambda$. A proton, on the other hand, would gain about 7.26 MeV from the same laser. As will be demonstrated below, these numbers are at least one order of magnitude greater than the results of calculations that employ the accurate fields. In addition to employing the values of the fields right at the focus, this must also be due, in part, to setting $\beta_x \sim 1$ in arriving at Eq. (2.32).

Similar analysis involving the radially polarized fields (2.25)-(2.27) gives the following approximate expression for the maximum gain

$$G_r[\text{MeV/nucleon}] \sim \frac{Z}{A}\left(\frac{\lambda}{\pi w_0}\right)^2\sqrt{240P_r[\text{TW}]}. \tag{2.33}$$

According to this expression, a carbon nucleus in a 1 TW field focused to $w_0 = 0.48\lambda$ achieves a gain $G_r \sim 3.41$ MeV/nucleon, which is slightly smaller than what would be obtained from a linearly polarized field of the same parameters. On the other hand, the gain by a proton would be $G_r \sim 6.81$ MeV. In fact, a comparison of Eqs. (2.32) and (2.33) shows that G_r will be greater than G_l as long as $w_0/\lambda < \sqrt{2}/\pi \sim 0.45$. Unfortunately, only low-intensity radially polarized beams may be generated in the laboratory at present [77–79].

2.4 The simulations

In this Section the full power of the accurate field expressions will be used to study the dynamics of bare nuclei on the basis of Eqs. (2.29). A simple order-of-magnitude estimate [81] reveals that the inter-particle Coulomb force, F_C,

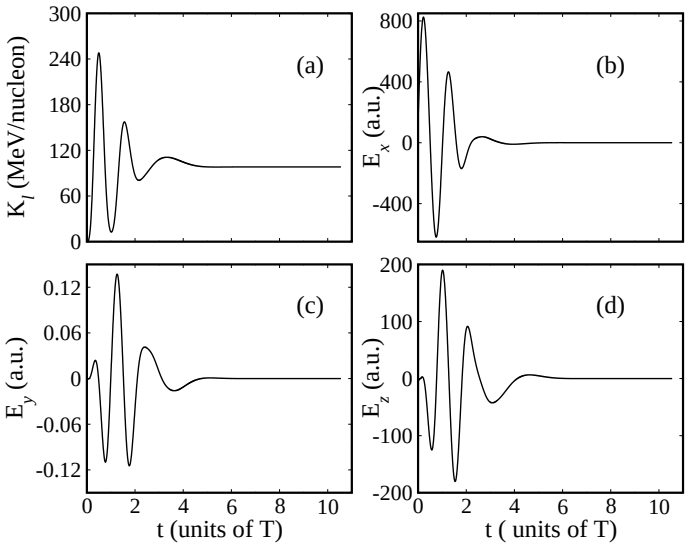

Figure 2.5 – (a) Kinetic energy of a nucleus of oxygen as a result of interaction with a linearly polarized 10 PW laser beam, and (b)-(d) the electric field components E_x, E_y and E_z, respectively, seen by the particle along its trajectory as functions of the time in units of T, the laser period. Integration of the equations of motion was carried out over a range of values $\Delta\eta = 20\pi$ of the variable $\eta \equiv \omega(t - z/c)$. The remaining parameters are the same as in Fig. 2.4.

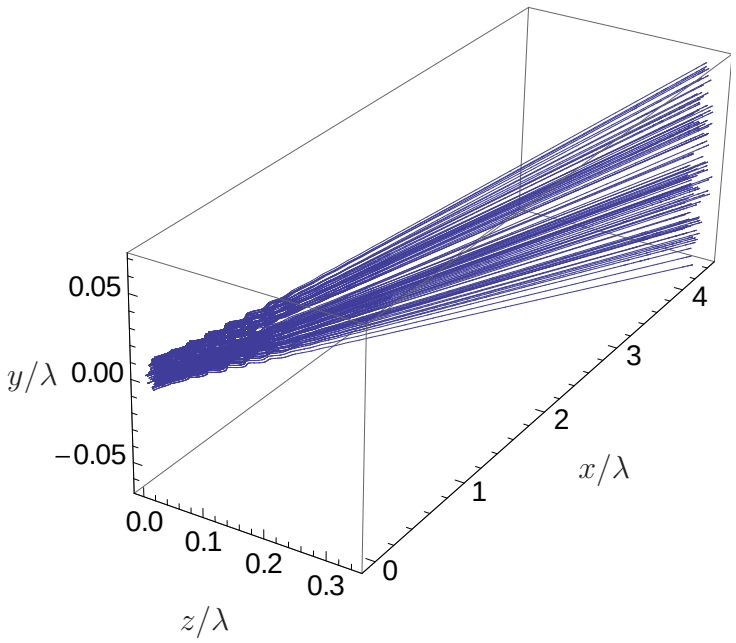

Figure 2.6 – 3D trajectories of 100 He^{2+} nuclei (alpha particles) in a 1 PW linearly polarized laser beam. All other parameters are the same as in Fig. 2.4.

between a pair of, say, protons in an ensemble of the sort described above is small compared to the force, F_L, felt by a particle of the same type from the laser electric field. For the laser-field intensities used in our calculations in this paper, $F_C \ll F_L$ for any ionic charge state. Furthermore, as it has been shown by simulations including the inter-ionic interaction in the relativistic equations of motion (see [82] and Chapter 3), at the low particle densities considered in our simulations (approx. 10^{17} ions/cm^3), even the field-free evolution of the ionic ensemble after acceleration is only negligibly influenced by ion-ion interaction effects.

We consider an ensemble[2] of N non-interacting particles initially in a cylinder of radius R_c and length L_c oriented along the laser beam axis, taken as the z-axis, and centered on the origin of coordinates as shown in Fig. 2.3. The initial position coordinates (x_0, y_0, z_0) will be taken as uniformly distributed within the cylinder (but will be picked at random in our numerical simulations). The particles will be assumed to possess initial kinetic energies distributed normally around a mean value $\bar{K}$ and having a spread ΔK. Without any loss of generality, the initial motion of all particles will be taken in the xz-plane and at some angle θ_i with respect to the beam axis.

Our interest, in this Section, is mainly in the energy gain, or exit kinetic energy, of the nuclei, their trajectories and, hence, the aspects that determine the quality of an accelerated beam of such accelerated nuclei. In the next two sections we study the laser acceleration of four nuclear species, namely, hydrogen, helium, carbon and oxygen in some detail.

2.5 Acceleration by a linearly polarized laser beam

Intense high-energy proton beams are widely generated by irradiating solid surfaces with intense laser light [43, 50–58]. The mechanism at work in these experiments is the target normal sheath acceleration (TNSA), caused by the strong quasi-static electric field, which is generated by the laser-assisted ionization of the target electrons and the positive ions they leave behind. In our work, alternatively, the method is one of acceleration in vacuum by subjecting the particles directly to the laser beam. In the subsequent simulations, the wavelength will be taken as $\lambda = 10.6$ μm, corresponding to a CO_2 laser. Choosing a wavelength larger than the conventional range around 1 μm, which characterizes titanium-sapphire and Nd:YAG lasers, is motivated by the fact that the focal volume increases approximately as $\propto \lambda^3$, which allows for three orders of magnitude more particles to be accelerated by the laser pulse as one bunch. Note that, for $w_0 \sim \lambda$, the Rayleigh length $z_r = \pi w_0^2/\lambda \sim \pi\lambda$. In our calculations, however, focusing will be to a waist radius $w_0 = 0.48\lambda$. Note that the peak intensity of a linearly polarized 100 TW laser system, focused to this

[2]This method is adapted from [62].

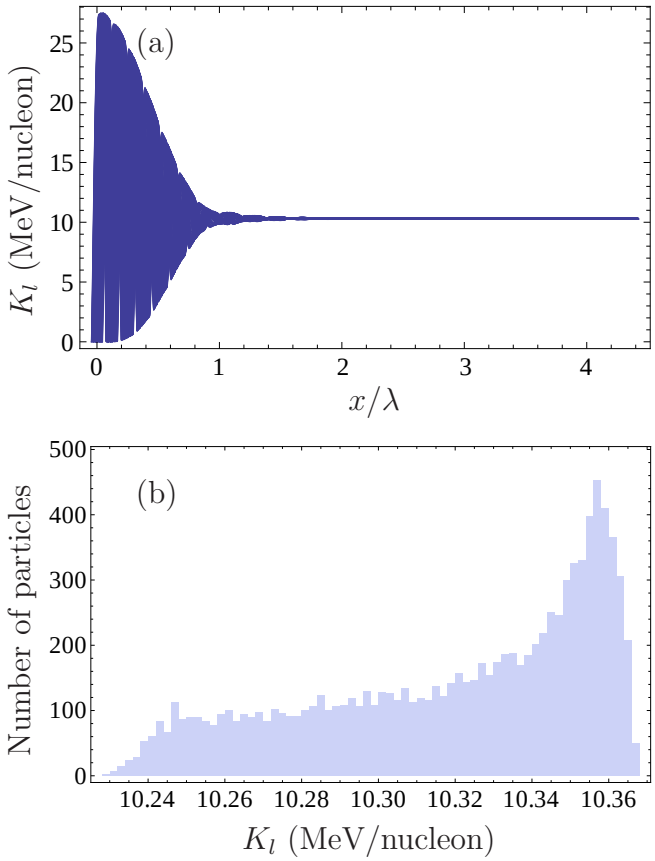

Figure 2.7 – (a) Exit kinetic energies of 100 He nuclei (alpha particles) in a 1 PW linearly polarized laser beam vs. the excursion of each along the x-axis (the laser polarization direction). (b) The distribution of final kinetic energies of 10,000 alpha particles. All other parameters are the same as in Fig. 2.4.

level, is already $I \sim 2.14 \times 10^{20}$ W/cm^2. We consider an initial ensemble of N = 5000 particles injected at an angle $\theta_i = 10^\circ$ relative to the beam axis. The particles have a mean kinetic energy $\bar{K} = 10$ keV and a spread $\Delta K = 10$ eV. The initial coordinates of the particles will be randomly picked from within a cylinder of length $L_c = 1$ μm and radius $R_c = 0.1$ μm [62].

Results from single-particle calculations are presented in Fig. 2.4. The particle in each case is selected at random from the ensemble described above. In this figure, the kinetic energy, $K \equiv Mc^2(\gamma - 1)$, of each particle is shown as it evolves along the x-axis of its trajectory. Note that the exit kinetic energy, at the end of the particle trajectory, displayed in Fig. 2.4 is about ten times greater than the estimates made above. Such a deviation is not surprising, given that in the simulations we considered tightly focused laser fields. As the laser power is tuned from 0.1 PW to 10 PW, a proton's exit kinetic energy increases roughly from 4 MeV to 523 MeV. On the other hand, evolution of the kinetic energies of all the other nuclear species, as well as their exit values, are more or less the same. This should come as no surprise because the gain depends on the charge to mass ration Z/A, as shown in the qualitative analysis, Eqs. (2.32)

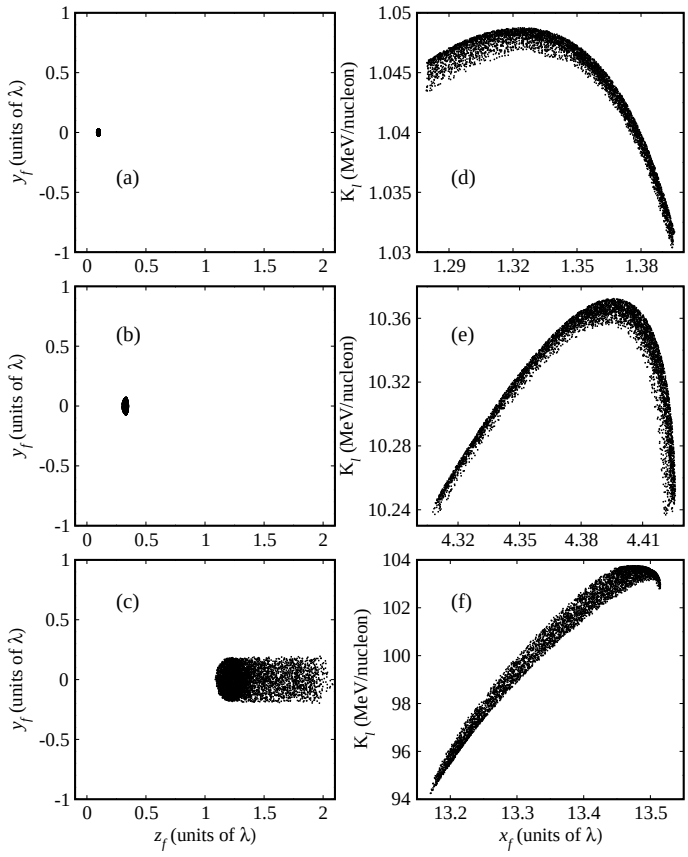

Figure 2.8 – (a)-(c) Accelerated particle beam cross-sections in the yz-plane (cf. Fig. 2 of [62] calculated at shorter λ), and (d)-(f) exit kinetic energies of the accelerated particles vs. the total excursion distance along the laser polarization direction. The laser power used in producing each row of figures is 0.1, 1 and 10 PW (top to bottom). The initial ensemble consists of 5000 He^{2+} nuclei in a cylinder of length $L_c = 1$ μm and radius $R_c = 0.1$ μm. All other parameters are the same as in Fig. 2.4.

and (2.33). This ratio is 0.5 for helium , carbon and oxygen, while it is equal to unity in the case of the proton. The exit kinetic energies of the He, C, and O nuclei increase from roughly 1 MeV/nucleon to 97 MeV/nucleon as the laser power is increased from 0.1 PW to 10 PW. We would like to note that while laser powers in the 0.1–1 PW regime are readily available today, powers of the order of tens of PWs will be provided by upcoming facilities [6, 7]. Also, the problem of focusing to sub-wavelength waist radii at such powers is yet to be resolved.

In Fig. 2.5 (a) evolution of the kinetic energy of a nucleus of oxygen (O^{8+} ion) is shown as a function of the time. Note that interaction of the particle with the 10 PW laser field is substantial only over a few laser field cycles. No appreciable energy is gained beyond that. To see which laser electric field components were most effective in the acceleration process we plot the strengths of all three components along the particle trajectory in (b)-(d). During the interaction, the

Power (PW)	$\bar{x}_f \pm \Delta x_f$ (λ)	$\bar{y}_f \pm \Delta y_f$ (λ)	$\bar{z}_f \pm \Delta z_f$ (λ)	$\Delta\Omega$ (sr)	$\bar{K}_l \pm \Delta K$ (MeV/nucleon)
0.1	1.34 ± 0.03	0.00 ± 0.01	0.10 ± 0.01	1.9×10^{-4}	1.044 ± 0.005
1	4.38 ± 0.03	0.00 ± 0.03	0.33 ± 0.01	8.1×10^{-5}	10.33 ± 0.04
10	13.37 ± 0.10	0.00 ± 0.09	1.39 ± 0.22	4.7×10^{-4}	100.8 ± 2.8

Table 2.1 – Particle coordinates, beam solid angles and kinetic energies at the ends of the trajectories of helium nuclei accelerated by linearly polarized laser beams. Results shown here are derived from the data used to produce Fig. 2.8.

figures show that, for the parameter set employed, E_x has been most effective in accelerating the particle, E_y more than three orders of magnitude less effective, while E_z has mostly played a negative (decelerating) effect.

For the purpose of illustration, we show trajectories of 100 particles from the ensemble, in Fig. 2.6. The particles are accelerated in the direction of the resultant $\boldsymbol{E}$ field, from which they gain the most energy. With time, a particle develops substantial momentum and the $\boldsymbol{v}\times\boldsymbol{B}$ force begins to affect its direction of motion. Thus, wiggles in the trajectories show up over the part of the figure that corresponds to effective interaction, which is a few field cycles at most, followed by particle motion along essentially straight lines. The effect of all the force components causes the trajectories to lie within a wedge-like structure of an approximately rectangular cross section.

Shown in Fig. 2.7 are kinetic energies of the particles whose trajectories are displayed in Fig. 2.6. Note that the spread in the exit kinetic energies is quite small. More on this topic will be found below.

Next, effect of the acceleration process on an ensemble of 5000 alpha particles will be discussed. In Fig. 2.8, we show the positions to which the ensemble evolves as a result of the acceleration mechanism, together with the exit kinetic energies of its members. For example, Figs. 2.8(a)-(c) give the coordinates (z_f, y_f) at the ends of the 5000 trajectories. As the laser power increases, the (roughly) rectangular end beam cross-section grows in size indicating an increase in particle beam divergence. The cross-section also shifts center (to the right) which indicates the overall combined effect of the laser E_z and magnetic field components. This is also accompanied by the expected increase in the energy gain and final x excursion. Figs. 2.8(d)-(f) give the exit kinetic energies (at ends of trajectories) against the exit coordinate x_f. Note here, too, that the spread in exit kinetic energies is quite small, so is the spread in the excursion distance along the polarization direction. These points will be discussed further below, in connection with the suitability of a particle beam for use in radiotherapy.

For the purpose of further discussion of the results we denote by $\bar{x}_f, \bar{y}_f, \bar{z}_f$, and $\bar{K}_l$, the ensemble averages of the exit coordinates x_f, y_f, z_f and exit kinetic energy K_l, respectively, at the end of the trajectories. Furthermore,

$\Delta x_f, \Delta y_f, \Delta z_f$, and ΔK_l will denote the standard deviations in these quantities. As usual, a standard deviation will represent a measure of the spread in the quantity in question. According to Figs. 2.8(a)-(c) the final position coordinates in the zy-plane are randomly distributed in a region of space that may be approximated by rectangles whose sides can be estimated by $2\Delta z_f$ and $2\Delta y_f$. Recognizing that $\bar{x}_f$ is the largest excursion made by a particle along one of the three coordinate axes, we may also speak of a solid angle, defined approximately for our purposes here by $\Delta\Omega \simeq (2\Delta z_f)(2\Delta y_f)/\bar{x}_f^2$. Final mean position coordinates and the spread in each, in units of the laser wavelength λ, the approximate solid angle, in sr, and the kinetic energy and spread in it, in MeV/nucleon, are collected in Table 2.1, for the data of Fig. 2.8. Note that the spread in exit kinetic energy is ~ 0.5, 0.4 and 2.8%, respectively, in the three cases considered.

In comparison to these results, according the combined experimental-theoretical study of Ref. [53], TNSA produces similar maximal proton kinetic energies. At the laser intensities given in Fig. 2.9, TNSA results in kinetic energies of around 20, 60, and 250 MeV (see Fig. 1a of Ref. [53], showing results for a laser of a wavelength 1.054 μm), with energy spreads of the order of 20-30%, which is to be compared to our results of 5.1, 55 and 590 MeV, respectively (see Fig. 2.9). Thus, while our direct ion acceleration scheme is outperformed by TNSA at lower intensities, it leads to higher kinetic energy gains at the highest intensity of 7.41×10^{21} W/cm^2, and generally to much lower energy spreads (see Table 2.1). More efficient acceleration has been predicted by RPA schemes; e.g., in Ref. [83], a relativistic acceleration regime is suggested which leads to GeV/nucleon ion energies at an intensity of 10^{22} W/cm^2.

2.6 Acceleration by a radially polarized laser beam

Two characteristics give the radially polarized beam an edge over the linearly polarized one. It can be focused to a tighter spot, and it has three field components; one mainly responsible for the acceleration. The tighter spot means a higher peak intensity (see Fig. 2.2) and, hence, leads to better gain. On the other hand, the axial electric field component, E_z, which is mainly responsible for the acceleration, increases in strength with tighter focusing at the expense of the radial component E_r and the azimuthal magnetic component B_θ. Recall that both E_r and B_θ vanish identically on the beam axis, leaving E_z to work effectively alone to accelerate the particles.

Consequently, due to its geometrical properties, a radially polarized laser beam is better suited for the purpose of acceleration than a linearly polarized beam. Unfortunately, generation of high-intensity radially polarized light is still a challenge. Nevertheless, assuming such beams can be produced in the near future, we will present and discuss below results of numerical simulations similar

to the ones considered above, albeit for radially polarized beams.

To begin with, Fig. 2.9, in which evolution of the particle kinetic energies along the laser beam direction of propagation, is similar to Fig. 2.4. Note first that, by comparison, the exit kinetic energies in this case are slightly higher than in the linearly polarized case. The end particle coordinates (along the laser beam axis) are also greater than the excursion distances along the linearly polarized beam polarization direction. This hints at the strength of the axial electric field component, E_z, and its role in the acceleration process.

Further insight into the nature of the trajectories may be gained from Fig. 2.10 that will shed light on the accelerated particle beam quality. The first thing to note is the increase in transverse spreading, in the xy-plane, with increasing laser power. This divergence may also be assessed in terms of a solid angle defined roughly by $\Delta\Omega \simeq (2\Delta x_f)(2\Delta y_f)/\bar{z}_f^2$, where the area covered by the points is considered as a rectangle of sides $2\Delta x_f$ and $2\Delta y_f$. Fig. 2.10 is to be compared with Fig. 2.5. Note that E_z is the strongest component and from reading (a) and (d) together one concludes that E_z is the accelerating field component, while E_r (or equivalently its components, in this context, E_x and E_y) play a minor role.

Figures 2.11 and 2.12 are similar to Figs. 2.6 and 2.7. The rectangular shape taken by the beam cross section in 2.11 seems to be sharper than in 2.6. This conclusion is also supported by Fig. 2.13, which is the analog of Fig. 2.8. Evolution of the kinetic energy with excursion distance, as shown in Fig. 2.12, seems to suggest that the spread in exit energies is smaller in the radially polarized case than it is in the corresponding linearly polarized counterpart. Support for this conclusion may be found by comparing Figs. 2.13(d)-(f) with 2.8(d)-(f).

Results from our simulations employing radially polarized beams, paralleling those displayed in Table 2.1 for the linearly polarized case, are shown in Table 2.2. One observes an increase in energy gain with increasing power, as expected. Note that the spread in the exit kinetic energies is less than 1% in all of the three cases considered. Comparing corresponding items in Tables 2.1 and 2.2, one finds that the radially polarized fields result in more energy gain compared to the linearly polarized ones.

Power (PW)	$\bar{x}_f \pm \Delta x_f$ (λ)	$\bar{y}_f \pm \Delta y_f$ (λ)	$\bar{z}_f \pm \Delta z_f$ (λ)	$\Delta\Omega$ (sr)	$\bar{K}_r \pm \Delta K$ (MeV/nucleon)
0.1	0.03 ± 0.12	0.00 ± 0.02	2.63 ± 0.01	1.6×10^{-3}	1.334 ± 0.011
1	0.02 ± 0.48	0.00 ± 0.09	9.60 ± 0.06	1.8×10^{-3}	12.67 ± 0.11
10	0.01 ± 3.13	0.00 ± 0.55	49.15 ± 0.52	2.9×10^{-3}	142.3 ± 1.2

Table 2.2 – Particle coordinates, beam solid angles and kinetic energies at the ends of the trajectories of helium nuclei accelerated by radially polarized laser beams. Results shown here are derived from the data used to produce Fig. 2.13.

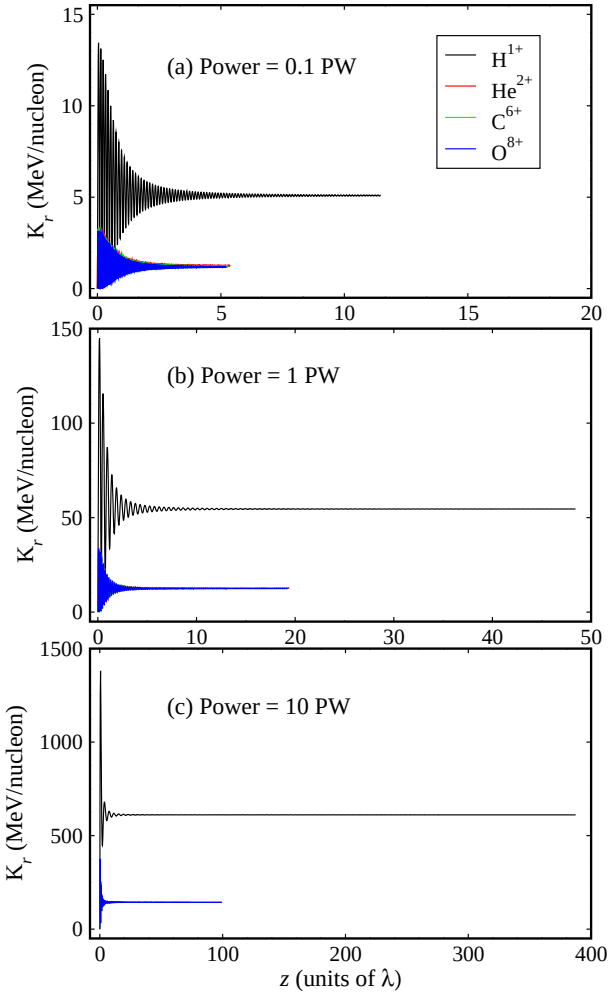

Figure 2.9 – Evolution of the kinetic energies of four nuclear species in radially polarized laser fields as functions of their excursion distances along the laser propagation direction (cf. Fig. 5 of [62] calculated at shorter λ and as function of laser cycle T). The laser wavelength is $\lambda = 10.6$ μm and the beam waist radius at focus is $w_0 = 0.48\lambda$. The given powers (0.1, 1 and 10 PW) correspond to peak intensities $I \sim 7.41 \times 10^{19}$, 7.41×10^{20} and 7.41×10^{21} W/cm^2, respectively. (Strictly, at points on the transverse plane through the focus where $z = 0$ and $r \sim w_0/\sqrt{2}$). Injection angle is $\theta_i = 10°$ for all particles. Integration of the equations of motion was carried out over a range of values $\Delta\eta = 200\pi$ of the variable $\eta \equiv \omega(t - z/c)$.

2.7 Initial ion distribution and pulse-shape effects

We performed simulations to study the effect of different volumes of the initial ion distribution on the energy spread of the accelerated particles. The size (volume) of the initial cylinder ($L_c = 1$ μm, $R_c = 0.1$ μm) has been increased by factors of 2, 4, and 8, while keeping the other parameters fixed. Table 2.3 shows the result of these calculations for a laser power of 10 PW. Given are

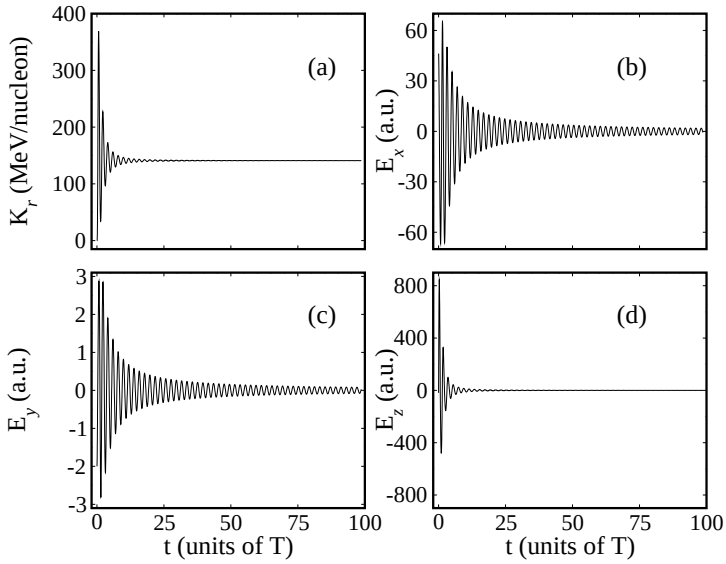

Figure 2.10 – Same as Fig. 2.5, but for a radially polarized beam. Note that $E_x = E_r \cos\theta$ and $E_y = E_r \sin\theta$, where $\theta = \arctan(y/x)$. Integration of the equations of motion was carried out over a range of values $\Delta\eta = 100\pi$ of the variable $\eta \equiv \omega(t - z/c)$. The remaining parameters are the same as in Fig. 2.9.

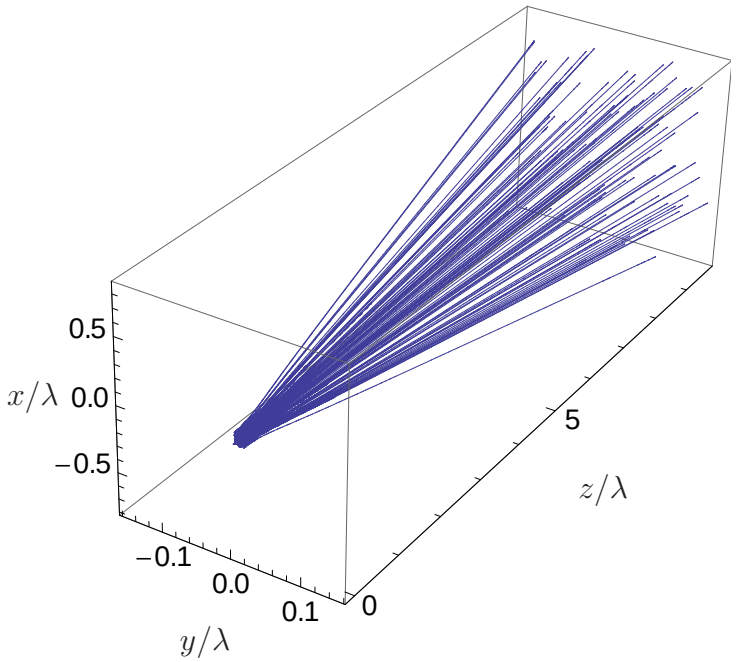

Figure 2.11 – Same as Fig. 2.6 but for a radially polarized laser system and the excursion distance is along the z-axis. Integration of the equations of motion was carried out over a range of values $\Delta\eta = 100\pi$ of the variable $\eta \equiv \omega(t - z/c)$.

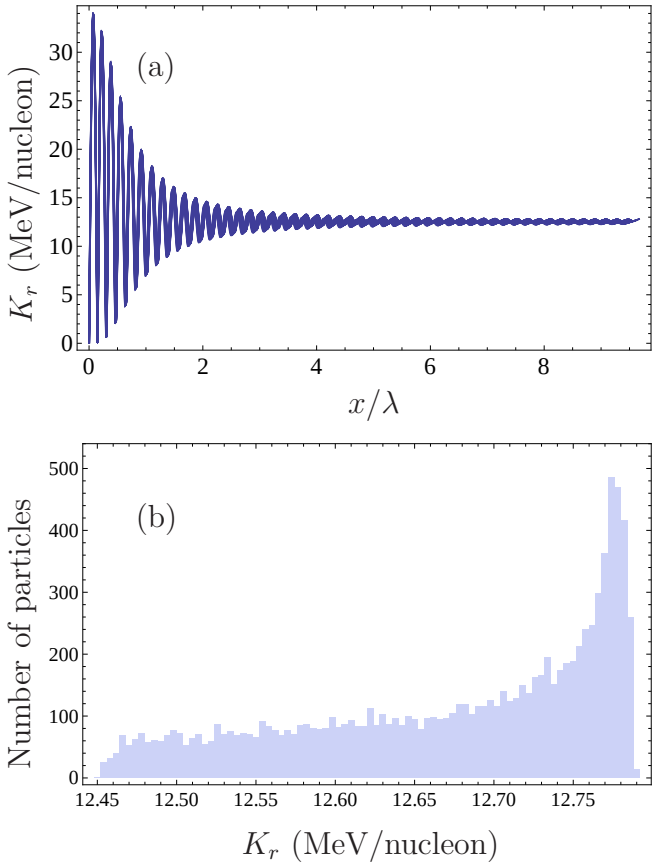

Figure 2.12 – Same as Fig. 2.7 but for a radially polarized laser system and the excursion distance is along the z-axis. Integration of the equations of motion was carried out over a range of values $\Delta\eta = 100\pi$ of the variable $\eta \equiv \omega(t - z/c)$.

the average final kinetic energies together with their spreads (standard deviations) and the percentage energy spread. As can be seen, the increase of the initial volume has a twofold effect: the average energy is slightly lowered and its spread increases significantly, roughly linearly. The values in the table give the tolerances on the size of the initial ionic distribution. As can be seen in Table 2.3, ions accelerated by radially polarized fields are somewhat more tolerant to the increase in size of the interaction region, thus allowing for the acceleration of a larger number of particles, while keeping kinetic energy and energy spread under control.

In addition, we performed simulations which employ laser systems that provide their energy in pulses of finite duration, and compared the results with those obtained using continuous wave (cw) lasers, keeping all other parameters fixed. To lowest order in the time, a pulse-shape can be introduced by multiplying the laser fields with the phase-dependent factor $g(\eta)$, where $\eta = \omega t - kz$, effectively via the following transformations

$$\begin{aligned} \boldsymbol{E} &\rightarrow g(\eta)\boldsymbol{E}, \\ \boldsymbol{B} &\rightarrow g(\eta)\boldsymbol{B}. \end{aligned} \tag{2.34}$$

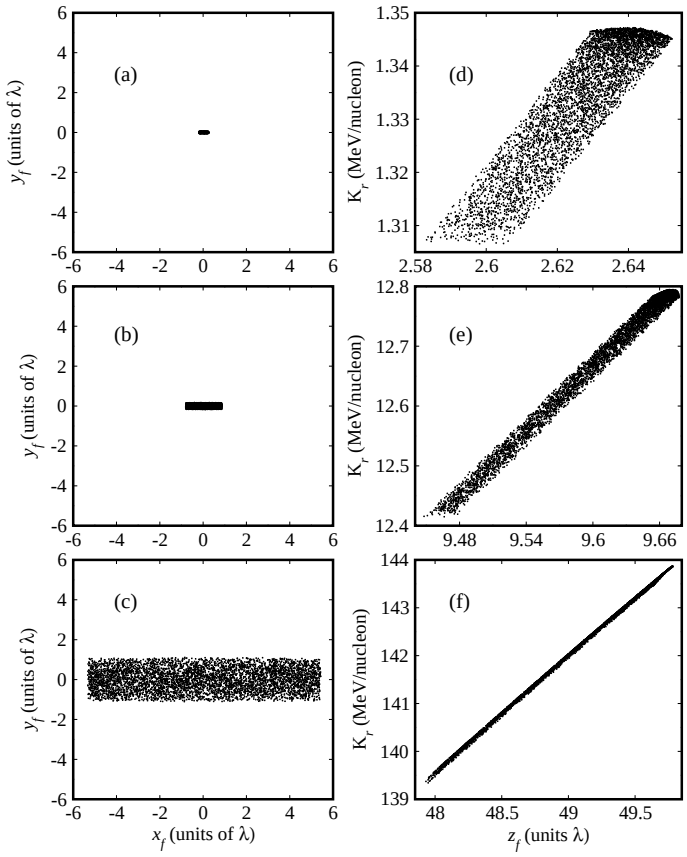

Figure 2.13 – Same as Fig. 2.8 but for acceleration employing a radially polarized beam.

	Size	$\bar{K}_l$ (MeV/nucleon)	$\Delta K_l/\bar{K}_l$ (%)	$\bar{K}_r$ (MeV/nucleon)	$\Delta K_r/\bar{K}_r$ (%)
H^{1+}	1×	416.7 ± 24.4	5.9	532.8 ± 13.3	2.5
	2×	416.2 ± 50.6	12	530.1 ± 16.8	3.2
	4×	403.3 ± 86.9	22	527.2 ± 20.9	4.0
	8×	359.2 ± 152	42	517.6 ± 29.0	5.6
He^{2+}	1×	90.65 ± 0.93	1.0	122.0 ± 1.0	0.8
	2×	90.49 ± 1.70	1.9	121.4 ± 1.5	1.2
	4×	90.20 ± 2.73	3.1	120.2 ± 2.4	2.0
	8×	89.78 ± 4.51	5.0	118.8 ± 3.7	3.1

Table 2.3 – Dependence of the average final kinetic energy $\bar{K}$ and the relative kinetic energy spread $\Delta K/\bar{K}$ on the volume of the initial distribution. The size of the initial ionic distribution is given as a multiple of the volume defined in the text. The protons and alpha particles are interacting with linearly (l) or radially (r) polarized light.

	$\bar{K}_l$ (MeV/nucleon)	$\pm \frac{\Delta K_l}{K_l}$	$\bar{K}_r$ (MeV/nucleon)	$\pm \frac{\Delta K_r}{K_r}$
	cw	pulsed	cw	pulsed
	$\tau = 0.25\,\mathrm{ps}$			
C^{6+}	46.36 ± 0.15	42.58 ± 0.42	57.54 ± 0.50	57.55 ± 0.50
O^{8+}	46.35 ± 0.15	42.56 ± 0.43	57.50 ± 0.50	57.50 ± 0.50
	$\tau = 0.5\,\mathrm{ps}$			
C^{6+}	46.36 ± 0.15	45.13 ± 0.22	57.54 ± 0.50	57.54 ± 0.50
O^{8+}	46.35 ± 0.15	45.12 ± 0.22	57.50 ± 0.50	57.50 ± 0.50

Table 2.4 – Average and standard deviation of the final kinetic energies of carbon and oxygen bare nuclei accelerated by linearly- and radially-polarized laser fields. Acceleration cases corresponding to cw and pulsed fields are compared, using 5 PW laser systems focused to waist radii $w_0 = \lambda/2$.

Following K. T. McDonald [84, 85], the following pulse-shape factor has been chosen

$$g(\eta) = \mathrm{sech}\left(\frac{\eta}{\eta_0}\right). \tag{2.35}$$

This choice justifies using the ansatz given by Eq. (2.34) in the limit $\eta_0 \gg 1$ [84, 85]. The dimensionless phase parameter η_0 can be directly related to the pulse duration τ, itself taken as the full width at half maximum (FWHM), via the relation

$$\eta_0 = \omega\tau / \ln\left[\frac{2+\sqrt{3}}{2-\sqrt{3}}\right], \tag{2.36}$$

with ω the laser frequency. In order to fulfill the condition $\eta_0 \gg 1$, we chose a pulse duration $\tau = 0.25\,\mathrm{ps}$ (approximately equivalent to 7 laser cycles for $\lambda = 10.6\,\mu\mathrm{m}$). For this choice, $\eta_0 \approx 16.9 \gg 1$. Infrared laser pulses with a pulse duration on the ps scale and with TW powers can be generated experimentally (see e.g. [86]), and an extension to higher powers is anticipated in the near future.

Table 2.4 summarizes the results of our simulations on the pulse-shape effects. Listed are the average final kinetic energies together with their spreads for carbon and oxygen nuclei. It can be seen that the introduction of a pulse-shape has negligible influence in the case of the longer pulse $\tau = 0.5\,\mathrm{ps}$ (for both polarizations). Whereas in the case of the shorter pulse $\tau = 0.25\,\mathrm{ps}$, only the results for the radially polarized laser fields remain effectively unchanged. For the pulsed linearly polarized case, the energy is roughly 8% lower than when the cw systems are used, and the energy spread is more than doubled, but still remaining less than 1% in any case.

2.8 Conclusions

In this Chapter, theoretical calculations for electron laser acceleration [33, 62, 71], have been extended to cover similar configurations involving bare nuclei, by numerically solving the relativistic equations of motion of the particles in radially and linearly polarized laser fields like it was done in [62]. The main results include acceleration of bare nuclei of hydrogen, helium, carbon and oxygen, to energies ranging from a few to several hundred MeV/nucleon, using laser systems of power 0.1−5 PW, focused down to waist radii in the neighborhood of half a laser wavelength ($w_0 \sim \lambda/2$). For the charge species studied, the radially polarized fields have been shown to lead to slightly higher energy gains than would be obtained using the linearly polarized fields. The linearly polarized fields, however, lead to a lower spread in the particle beam energy gain, at least for the parameter sets employed in our simulations.

Recognizing that a radially polarized beam may be focused to a tighter spot than would be the case for a linearly polarized one, our results suggest that a laser beam of radial polarization once it can be generated with the desired intensities, may be a better candidate for use in laser acceleration of ions and bare nuclei, for medical and other applications. It has also been demonstrated that focusing even a 100 TW laser beam to a sub-wavelength spot radius increases its peak intensity to the levels needed for acceleration of bare nuclei.

Furthermore, choosing a laser system with a wavelength as long as possible is shown to increase the interaction volume of the focused light beam and the initial ionic ensemble, which leads to a higher number of particles accelerated in one bunch at a given initial ionic density. As an example, CO_2 lasers with a wavelength of 10.6 μm accelerate three orders of magnitude more particles in one shot as the most wide-spread infrared systems with wavelengths around 1 μm, making these systems more appealing for ion acceleration applications once the power of these laser systems reaches the range required.

Finally, calculations have been performed in order to assess the effect, on the kinetic energies of the accelerated particles, due to variations in volume of the initial ionic distribution, and to an added pulse-shape on the laser systems employed. Our investigations prove that for sufficiently long pulses with a duration over 0.25 ps, the pulse shape effects are negligibly small, especially in the case employing laser fields of the radially polarized variety.

Chapter 3

Crossed-beams laser acceleration

Simulations based on the coupled relativistic equations of motion show that protons stemming from laser-plasma processes can be efficiently post-accelerated employing single and crossed pulsed laser beams focused to spot radii on the order of the laser wavelength. We demonstrate that the crossed beams produce quasi-monoenergetic accelerated protons with kinetic energies exceeding 200 MeV, small energy spreads of about 1% and high densities as required for hadron cancer therapy. To our knowledge, this is the first scheme allowing for this important application based on an all-optical set-up. Parts of this Chapter have been published in Ref. [82]

.

3.1 Introduction

In this Chapter, we investigate the vacuum post-acceleration of plasma-generated ions by means of lasers in a single- or crossed-beams configuration. The latter scheme of laser particle acceleration was first proposed for electrons [31, 32, 37, 38]. In contrast to the previous Chapter, we performed simulations which model a controlled particle injection into the focus of a pulsed laser beam in a realistic way and which take into account particle-particle interaction effects. We demonstrate that we do reach the proton flux threshold necessary for broader radio-oncological use, without compromising the kinetic energy and its spread.

The basic idea is to send the protons originating from a TNSA [43, 50–58] or S-LPA [59] experiment through the crossing point of two laser beams at a half-angle θ with respect to the z-axis (see Fig. 3.1 (b) for a scheme and a coordinate system). A simple illustration of the mechanism may be given in the plane-wave picture. Based on the assumption that the laser fields have the same amplitude, frequency, phase and are polarized as shown in Fig. 3.1 (b), the resultant electric

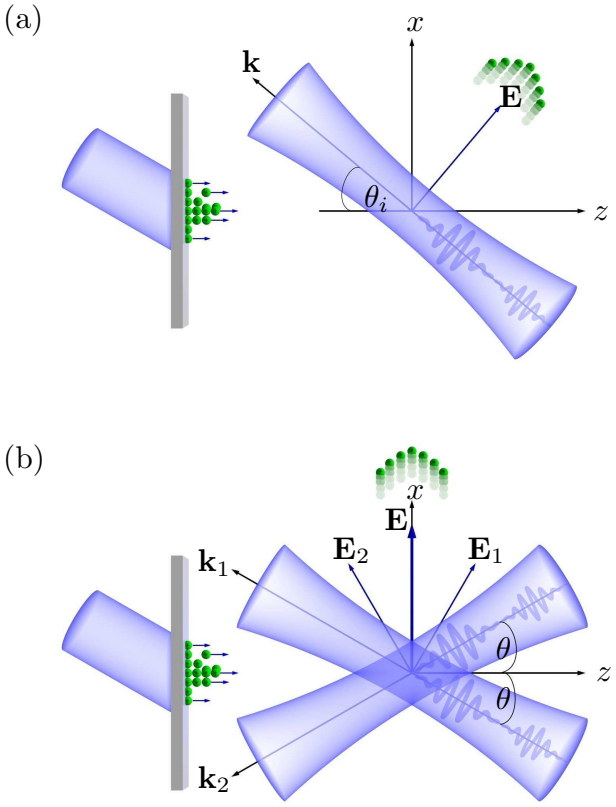

Figure 3.1 – (a) The protons, produced by laser-plasma interaction (left hand side), are injected at the angle θ_i with respect to the propagation direction of a pulsed beam through its focus. The laser field polarization is denoted by $\mathbf{E}$ and the propagation direction is given by $\mathbf{k}$. The protons are ejected out of the focus in the polarization direction $\mathbf{E}$. (b) Here, the protons are injected through the intersection point of two pulsed beams with a crossing half-angle θ. The laser field polarizations are denoted by $\mathbf{E}_1$ and $\mathbf{E}_2$ and their propagation directions are given by $\mathbf{k}_1$ and $\mathbf{k}_2$. The protons are ejected in direction of the resulting electric field $\mathbf{E}$.

field component along the symmetry axis of the set-up vanishes for all points on the x-axis. At the same time, the x-component, increased by constructive interference, strongly accelerates the particles (similar to [38], but for different polarization). After the ejection of the charged particles from the focal region, i.e. no laser-particle interaction takes place anymore, they continue to move with constant velocity.

The superposition of multiple laser beams to obtain a single beam not only with correspondingly higher power but also with preserved beam quality plays a central role in the construction of several laser systems in a wide range of powers. In order to generate one high-power beam, all single beamlines have to add coherently. For instance, the laser system of the Extreme Light Infrastructure (ELI) facility (see p. 52 of Ref. [6]) will partly be based on a coherent combination of 10 to 12 beams of petawatt power which will lead to an exawatt-class output power. Hence, we conclude that experimentally implementing two

coherently superposed crossed beams and one beam for the laser-plasma interaction as a particle injector is certainly demanding, but it is feasible and given the high potential of the set-up it is worth the effort.

The results of our theoretical simulations demonstrate that the protons gain kinetic energies larger than 200 MeV (employing two crossed beams each with a peak intensity of 1.9×10^{24} W/cm^2) with an energy spread of roughly 1%. Furthermore (assuming a realistic repetition rate of 10 Hz [6, 87]), the total number of generated protons reaches 10^{10} min^{-1}. For the first time, all requirements are fulfilled for broader radio-oncological use [15, 18] based on an optical accelerator.

This Chapter is organized as follows. In Section 3.2, the injection into a pulsed beam is described. Then we introduce the equations of motion in Section 3.3 and we discuss the role of particle-particle interaction effects. After defining the coordinate system for the crossed laser fields in Section 3.4, we present the results of our simulations in Section 3.5. Our conclusions are given in Section 3.6.

3.2 Injection mechanism

In order to generate ultra-strong accelerating fields [6, 7] of 10^{24} W/cm^2, one needs to focus the laser field to a beam waist radius on the order of its wavelength [5], which also ensures that the Lawson-Woodward theorem [27, 28] is violated. This necessitates an accurate description of the fields beyond the widely-used paraxial approximation. The parameters of a linearly polarized Gaussian beam which propagates in the z-direction and is polarized in the x-direction and subsequently rotated by θ_i (Fig. 3.1 (a)) will be used to model the fields, i.e. the beam waist radius w_0, the Rayleigh length $z_r = \pi w_0^2/\lambda$, where λ is the laser's wavelength, and the diffraction angle is $\varepsilon = w_0/z_r = \lambda/(\pi w_0)$. For the expressions of the Cartesian field components E_x, E_y, E_z, B_x, B_y, B_z of a linearly polarized laser beam, as well as the expression for the power of the fields to order ε^{11} in the diffraction angle we refer to Section 2.5 of the previous Chapter and for details to the literature [62, 63].

High-intensity laser systems provide their energy in short pulses which are already sufficient to accelerate particles to high velocities [88]. Employing pulsed fields also ensures that the particles injected into the focus get captured rather than reflected. To the lowest order in time, this can be described by multiplying the electromagnetic field components with a Gaussian temporal envelope factor,

$$\begin{aligned} \boldsymbol{E} &\rightarrow \exp\left(-\frac{(t-z/c)^2}{2\Delta t^2}\right)\boldsymbol{E}, \\ \boldsymbol{B} &\rightarrow \exp\left(-\frac{(t-z/c)^2}{2\Delta t^2}\right)\boldsymbol{B}, \end{aligned} \tag{3.1}$$

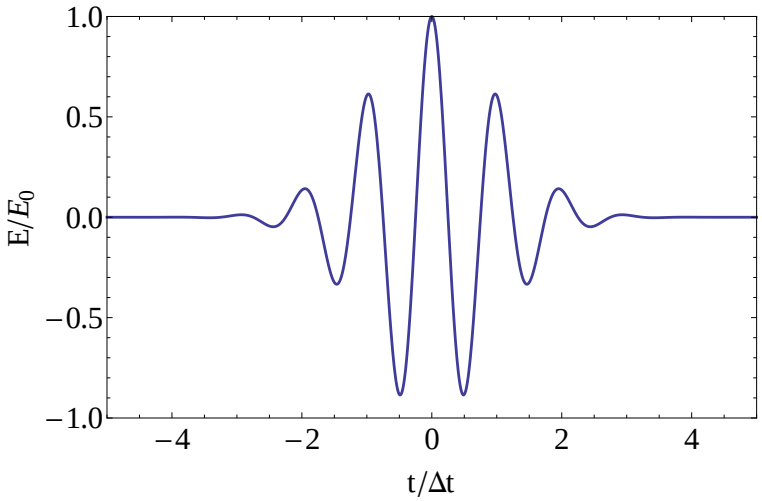

Figure 3.2 – Schematic of a laser pulse with a Gaussian envelope centered around $t = 0$ with a Full Width at Half Maximum (FWHM) pulse duration $\Delta t_{\mathrm{FWHM}} = 2\sqrt{2\log 2}\Delta t$.

with Δt defined via the Full Width at Half Maximum (FWHM) pulse duration $\Delta t_{\mathrm{FWHM}} = 2\sqrt{2\log 2}\Delta t$ (see Fig. 3.2 for a schematic). This approximation is valid for $T/\Delta t_{\mathrm{FWHM}} \ll 1$, with T being the laser period. For the titanium-sapphire laser with wavelength $\lambda = 800$ nm ($T = 2.65$ fs) and pulse durations of $\Delta t \gtrsim 10$ fs used in our simulations, this turns out to be an adequate description. Hence, further temporal corrections [89] which describe the field solutions as a dual power series in the diffraction angle ε and in the small ratio $T/2\pi\Delta t$ can be neglected.

In order to simulate a realistic particle injection into the focal point of the laser pulses, we have to ensure that the ensemble is not already exposed to the laser fields at the beginning of the simulation. This is realized by starting the simulations at time $t_i \leq -5\Delta t$. At these initial times the laser pulse has not arrived yet as one can see from Fig 3.2, such that the particles' motion is only negligibly influenced by the external laser fields. Hence, it is justified to place the initial particle ensemble at an arbitrary spatial position.

To underline the importance of the correct initial time, we compare in Fig. 3.3 the motion of a proton starting at the same spatial point but having two different initial times. One can see that in the case when the particle is directly exposed to the laser fields at $t_i = 0$ (dashed line), it immediately gains energy and is ejected out of the focus after one laser cycle. In a realistic setting, we choose an initial time of $t_i = -10\Delta t$: the particle slowly starts to oscillate and then gets captured and accelerated by the approaching pulse (full line). Choosing the initial time to be $t_i = 0$ would lead to an energy gain overestimation by a factor of approximately three. Our above studies on varying the particles initial conditions have been published in [82]. A similar detailed study has been published by Wang et al. [90].

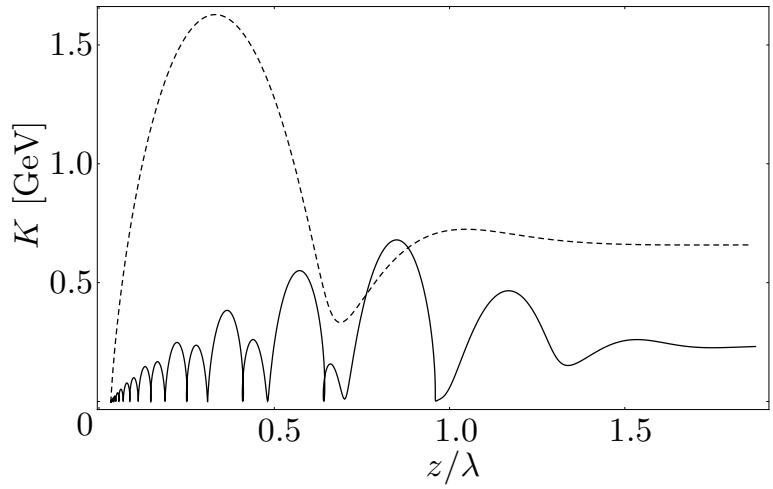

Figure 3.3 – Kinetic energy K for one proton initially being at rest and located at $x = z = \lambda/30$ and $y = 0$. The initial time is $t_i = 0$ (dashed line) and $t_i = -10\Delta t$ (full line). The single proton dynamics is compared at same laser parameters (see text).

3.3 The role of particle-particle interaction effects

The motion of an interacting ensemble of N identical particles of mass m and charge q in the electric and magnetic fields $\boldsymbol{E}$ and $\boldsymbol{B}$, respectively, of a laser beam is considered classically, with randomized initial distributions. The use of laser systems of high intensity (exceeding 10^{24} W/cm^2 for protons) requires a relativistic treatment of particle motion. Thus, the dynamics is governed by the coupled Lorentz-Newton (or propagation) equations[1] (given in SI units):

$$\begin{aligned} \frac{d\boldsymbol{p}_j}{dt} &= q\left(\boldsymbol{E}(\boldsymbol{r}_j) + \boldsymbol{E}_j^{\text{int.}} + c\boldsymbol{\beta}_j \times \left(\boldsymbol{B}(\boldsymbol{r}_j) + \boldsymbol{B}_j^{\text{int.}}\right)\right), \\ \frac{d\mathcal{E}_j}{dt} &= qc\boldsymbol{\beta}_j \cdot \left(\boldsymbol{E}(\boldsymbol{r}_j) + \boldsymbol{E}_j^{\text{int.}}\right). \end{aligned} \tag{3.2}$$

The relativistic energy and momentum of a given particle labeled with j are denoted here by $\mathcal{E}_j = \gamma_j mc^2$ and $\boldsymbol{p}_j = \gamma_j mc\boldsymbol{\beta}_j$, respectively, with $\boldsymbol{\beta}_j = \boldsymbol{v}_j/c$ its velocity scaled by c, and $\gamma_j = (1 - \beta_j^2)^{-1/2}$ its Lorentz factor. The fields mediating inter-ionic interaction are modeled by [80]

[1] Note this form of equations serve also as propagation equations in PIC simulations [69] (see Chap. 4).

$$\boldsymbol{E}_j^{\text{int.}} = \sum_{k\neq j}\left(-\nabla\phi_{jk} - \frac{\partial}{\partial t}\boldsymbol{A}_{jk}\right), \tag{3.3}$$

$$\boldsymbol{B}_j^{\text{int.}} = \sum_{k\neq j}\left(\nabla\times\boldsymbol{A}_{jk}\right), \tag{3.4}$$

with $j,k\in\{1,2,\ldots,N\}$. The interaction potentials read

$$\phi_{jk} = \frac{q}{4\pi\epsilon_0}\frac{1}{|\boldsymbol{r}_j-\boldsymbol{r}_k|}, \tag{3.5}$$

$$\boldsymbol{A}_{jk} = \frac{q}{8\pi\epsilon_0 c^2|\boldsymbol{r}_{jk}|}\left(\boldsymbol{v}_k + \frac{\boldsymbol{r}_{jk}(\boldsymbol{v}_k\cdot\boldsymbol{r}_{jk})}{|\boldsymbol{r}_{jk}|}\right), \tag{3.6}$$

with the relative displacement $\boldsymbol{r}_{jk}=\boldsymbol{r}_j-\boldsymbol{r}_k$ and ϵ_0 being the vacuum permittivity. Eq. (3.5) is the scalar part of the interaction given by the Coulomb potential, whereas relativistic effects such as retardation and current-current interaction are included in the Darwin vector potential up to $\mathcal{O}(\beta^2)$ [80] in Eq. (3.6). Typical kinetic energies of the accelerated protons are of about 200 MeV (cf. Tab. 3.2), which corresponds to $\beta^2\approx 0.3$. Consequently, the truncation of the interaction up to $\mathcal{O}(\beta^2)$ is justified and higher-order contributions such as those up to $\mathcal{O}(\beta^4)$ in Ref. [91] will not be taken into account.

To obtain the kinetic energy gained by interaction with a laser beam, numerical solutions of the coupled equations of motion have to be determined. Due to the velocity-dependent Darwin vector potential in Eq. (3.6), the electric field modeling the interaction in Eq. (3.3) becomes dependent on derivatives of the velocity with respect to time. Hence, equation (3.2) is a system of differential algebraic equations of the form

$$\begin{aligned}
\frac{d\boldsymbol{\beta}_1}{dt} &= f_1\left(\boldsymbol{r}_1,\ldots,\boldsymbol{r}_N,\boldsymbol{\beta}_1,\ldots,\boldsymbol{\beta}_N,\frac{d\boldsymbol{\beta}_1}{dt},\ldots,\frac{d\boldsymbol{\beta}_N}{dt},t\right),\\
&\vdots\\
\frac{d\boldsymbol{\beta}_N}{dt} &= f_N\left(\boldsymbol{r}_1,\ldots,\boldsymbol{r}_N,\boldsymbol{\beta}_1,\ldots,\boldsymbol{\beta}_N,\frac{d\boldsymbol{\beta}_1}{dt},\ldots,\frac{d\boldsymbol{\beta}_N}{dt},t\right).
\end{aligned} \tag{3.7}$$

For each time step the system has to be solved algebraicly with respect to the variables $\frac{d\boldsymbol{\beta}_1}{dt},\ldots,\frac{d\boldsymbol{\beta}_N}{dt}$. The solution of the algebraic system is well-defined because of the only linear dependence on $\frac{d\boldsymbol{\beta}_1}{dt},\ldots,\frac{d\boldsymbol{\beta}_N}{dt}$. Then, a standard fourth-order Runge-Kutta algorithm is used to integrate the remaining system of ordinary differential equations that yields $\boldsymbol{\beta}_j^{\text{fin}}$ and, hence, γ_j^{fin} at a later final time t^{fin} taken equal to many laser field cycles, such that it is ensured that interaction with the full laser pulse takes place. Subsequently, the final kinetic energy of the particle can be determined as $K_j^{\text{fin}}=\gamma_j^{\text{fin}}mc^2$.

Foremost, we carry out simulations based on the coupled equations of motion Eq. (3.2) for an ensemble of 20 particles at typical distances for later applied

$\bar{x}_f$ (units of λ)	$\bar{y}_f$ (units of λ)	$\bar{z}_f$ (units of λ)	$\bar{K}_l$ (MeV/nucleon)
without interaction			
-4.32701 ± 0.00992	-0.00025 ± 0.08083	1.38096 ± 0.00216	114.571 ± 0.005
with interaction			
-4.34379 ± 0.02588	-0.00789 ± 0.06602	1.37911 ± 0.00579	114.574 ± 0.24

Table 3.1 – Particle coordinates and kinetic energies at the ends of the trajectories of an interacting proton ensemble of 20 particles accelerated by linearly polarized laser beams. The laser parameters are P=40 PW, Δt=10.7 fs, $w_0 = 1\lambda$ such that the particle dynamics takes place in the relativistic regime.

particle densities in order to determine the dominant nearest-neighbor contribution of proton-proton interaction effects on the resulting particle beam. Due to the dominating ponderomotive laser forces which lead to a fast drifting apart of the ensemble's particles, for relativistic laser intensities, i.e. $> 10^{24}$ W/cm^2 for protons, it turns out that the dynamics, the energy gain and its spread are influenced only slightly by inter-ionic interaction. A summary is given in Tab. 3.1. The fluctuation in the particles' endpoints and exit kinetic energies is larger, nevertheless the requirements of medical applications are still met. This is in contrast to the non-relativistic laser regime. Here, the repulsive Coulomb interaction is the prevailing part of the interaction, which is in this case non-negligible compared to the electromagnetic fields of the laser. As a consequence, the accelerated ions occupy a larger phase space volume. From radio-oncological point of view we are interested in proton beams of fully relativistic energies, hence for further calculations at these energies and densities it is sufficient to study the uncoupled equations of motions only, i.e. we set $\boldsymbol{B}_j^{\text{int.}} = \boldsymbol{E}_j^{\text{int.}} = \mathbf{0}$ in Eq. (3.2).

3.4 Coordinate transformation of the laser fields

The definition of a coordinate system for the crossed beams set-up depicted in Fig. 3.1 (b) is given by the coordinate transformations (rotations)

$$\begin{aligned} x_1 &= x\cos\theta - z\sin\theta, \\ y_1 &= y, \\ z_1 &= x\sin\theta + z\cos\theta, \end{aligned} \tag{3.8}$$

for the first beam and

$$\begin{aligned} x_2 &= x\cos\theta + z\sin\theta, \\ y_2 &= y, \\ z_2 &= -x\sin\theta + z\cos\theta \end{aligned} \tag{3.9}$$

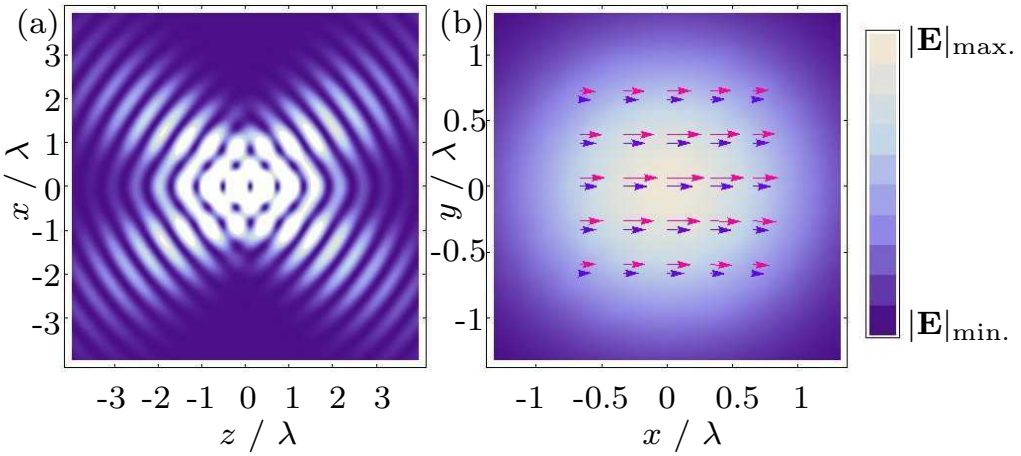

Figure 3.4 – (a) Intensity profile of two crossed Gaussian beams in the propagation plane $y = 0$. For visualization purpose the crossing-half angle is set to $\theta = 35°$. The brighter areas correspond to higher field intensities. (b) Vector field plot of the polarization plane $z = 0$ at $t = 0.2$ fs for the single beam scheme (blue arrows) with power P and crossed beam scheme (red arrows) with power $P/2$ for each beam. The constructive interference of the crossed beams results in a higher electric field strength in the intersection volume. The background of the graph shows a density map of the electric field strength $|\mathbf{E}|$ of two crossed beams in the polarization plane.

for the second beam, respectively. The resultant field components which enter Eq. (3.2) are

$$\begin{aligned} E_x &= (E_{1x} + E_{2x})\cos\theta + (E_{1z} - E_{2z})\sin\theta, \\ E_y &= E_{1y} + E_{2y}, \\ E_z &= (-E_{1x} + E_{2x})\sin\theta + (E_{1z} + E_{2z})\cos\theta, \\ B_x &= (B_{1z} - B_{2z})\sin\theta, \\ B_y &= B_{1y} + B_{2y}, \\ B_z &= (B_{1z} + B_{2z})\cos\theta. \end{aligned} \tag{3.10}$$

Choosing a small crossing half-angle θ leads to constructive addition of the dominating x-components of the electric fields in Eq. (3.10). The adding of further laser beams would further increase the laser intensity and hence the exit kinetic energy of the accelerated particles. With respect to the energy spread we could not achieve substantial improvement, however. For all subsequent simulations we restrict our analysis to the case of two crossed beams and set $\theta = 3°$.

For the intensity profile of the employed Gaussian beams see Fig. 3.4. In particular, from Fig. 3.4 (b) one can clearly sees that the constructive interference results in a stronger electric field.

	$\bar{K}$ [MeV]	N_i
S-LPA source, P=10 PW, Δt=19.2 fs, $w_0 = 1\lambda$		
single	28.1 ± 1.2 %	$1.0{\cdot}10^6$
crossed	59.4 ± 1.0 %	$1.0{\cdot}10^6$
S-LPA source, P=40 PW, Δt=10.7 fs, $w_0 = 1\lambda$		
single	113.2 ± 1.6 %	$1.0{\cdot}10^6$
crossed	233 ± 1.0 %	$1.0{\cdot}10^6$
S-LPA source, P=100 PW, Δt=23.8 fs, $w_0 = 2\lambda$		
single	73.2 ± 1.6 %	$1.3{\cdot}10^7$
crossed	152 ± 1.0 %	$1.3{\cdot}10^7$
TNSA source, P=100 PW, Δt=14.4 fs, $w_0 = 2\lambda$		
single	64.6 ± 0.7 %	$1.0{\cdot}10^5$
crossed	141 ± 0.5 %	$1.0{\cdot}10^5$

Table 3.2 – Average particle kinetic energy $\bar{K}$ and its percentual spread for different laser system parameters. $N_i = n_i \cdot V_{\text{focus}}$ is the number of ions one can accelerate as one bunch with $n_i^{\text{S-LPA}} \approx 10^{21}$ cm^{-3} and $n_i^{\text{TNSA}} \approx 10^{19}$ cm^{-3} is the ion density of the source used and V_{focus} denotes the volume initially containing all ions. The crossing half-angle is $\theta = 3°$. The optimal particle injection angle for the single beam set-up is $\theta_i = 3°$ for the S-LPA source and $\theta_i = 50°$ in case of the TNSA source, respectively. For two crossed beams the particles are injected with an angle θ_c with respect to the symmetry axis (z-axis) of the laser beam configuration. In case of the S-LPA source we have $\theta_c = 0°$ and for the TNSA source $\theta_c = 50°$.

3.5 Results

We consider an ensemble of 5000 particles initially randomly distributed in a micron-scale volume V_{focus} oriented along the z-axis. The volume initially containing the particle ensemble has a length of the order of the laser wavelength and a radius of tens of nanometers, dependent on the focus diameter of the applied laser system, ensuring that all protons are exposed to a homogeneous field. The particles will be assumed to possess initial kinetic energies distributed normally around a mean value $\bar{K}$ and having a spread ΔK. As a source we take protons originating from laser-plasma interactions, such as the S-LPA mechanism, with $\bar{K} = 17$ keV [59] and assuming a large energy spread of $\Delta K = 100\,\%$ or from the TNSA mechanism, with $\bar{K} = 1.2$ MeV and $\Delta K = 25\,\%$ [51]. The total power and the beam pulse duration are varied. Note that the peak intensity of one linearly polarized 10-PW laser beam focused to $w_0 = 1\lambda$ is already $I \sim 9.6 \times 10^{23}$ W/cm^2 [6, 7].

Like in the previous Chapter, our work is motivated by medical applications and hence our main interest is to match the restrictive radio-oncological requirements for the energy gain and the energy spread. In Tab. 3.2, simulation

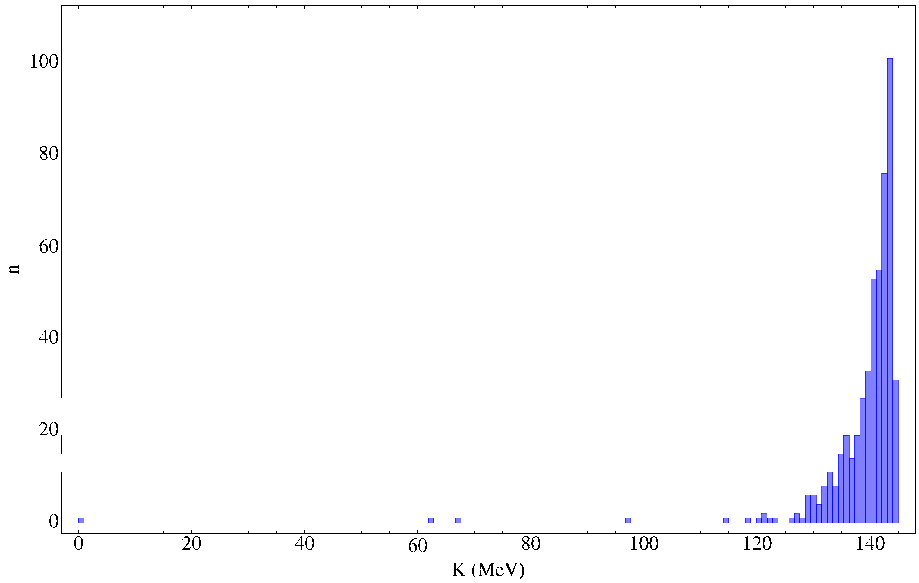

Figure 3.5 – Exit kinetic energy spectrum of particles being injected into an approaching Gaussian beam.

results for the laser acceleration are summarized. The single and crossed beams scheme are compared at same total laser power P, pulse duration Δt and focus radius w_0. The energy gain is ranging from 59 MeV to 233 MeV in case of the crossed beams setup and from 28 MeV to 113 MeV for injection of the ensemble into the focus of only one beam, respectively. Looking at the energy spread one can see that for the crossed beams it is always 1% and a little higher for the case of the single beam setup. For a typical exit kinetic energy spectrum of particles being injected into the focus of an approaching Gaussian beam, see Fig. 3.5.

Moreover, one can see from Tab. 3.2 that for the systems studied here, the average exit kinetic energy $\bar{K}$ obeys for constant injection angle and injection energy the rough scaling behavior $\bar{K} \propto I \propto P/w_0^2$. This behavior results from the fact that the optimal acceleration regime depends strongly on the pulse duration Δt rather than only on the electric field strength. It is achieved for the laser-particle interaction length being of the same order as the Rayleigh length. In Ref. [92], the same scaling behavior was derived for electrons. Therefore, in order to maximize the energy gain of the accelerated protons we first choose the laser power P and the focus radius w_0, and then adjust to the optimal pulse duration Δt.

A further scaling law can be derived for the particle number, which is proportional to the focus volume. Using $V_{\text{focus}} \propto w_0^2 \cdot z_r$ and the definition of the Rayleigh length $z_r \propto w_0^2$, one obtains $V_{\text{focus}} \propto w_0^4$. The typical particle number needed for ion cancer treatment is 10^6-10^{10} per shot with a repetition rate on the order of 5 Hz [13], depending on the ionic species. For a typical interaction volume, one needs at least an ion density of $n_i = 10^6/V_{\text{focus}} \approx 10^{20}\,\text{cm}^{-3}$ in order to render our scheme feasible for medical applications. Using plasma-

generated protons one obtains with the TNSA mechanism an ion density up to the order of $n_i^{\text{TNSA}} \approx 10^{19}\,\text{cm}^{-3}$ and the S-LPA ion source generates a density of $n_i^{\text{S-LPA}} \approx 10^{21}\,\text{cm}^{-3}$ [59]. The latter yields particle numbers of 10^7 per laser shot. Combined with lasers operated at 10 Hz repetition rate [6, 87] this ion number is sufficient for cancer therapy while for the TNSA mechanism a modest improvement would still be necessary.

Such improvement can e.g. be achieved by substituting the assumed titanium-sapphire laser by a super-intense CO_2 laser with a typical wave length of $\lambda = 10.6\,\mu\text{m}$. Using the fact that the waist radius $w_0 \propto \lambda$ and hence the Rayleigh length $z_r \propto \lambda$, the focal region thus increases by three orders of magnitude. Consequently, the ion density needed decreases by three orders of magnitude and the needed laser intensity by two orders of magnitude (cf. Chapter 2). In the near future the use of high repetition rate laser systems [6, 87] will further decrease the number of protons needed per shot.

3.6 Conclusions

The achievement of our studies in the present Chapter are threefold:

First, we demonstrated the theoretical feasibility to inject particles created from laser-plasma interactions (with typical kinetic energy distributions) into an approaching laser pulse and that one can maintain the proton beam quality given in Chapter 2. Furthermore, we quantified the difference in the exit kinetic energy of particles directly exposed to laser fields as it was done in our calculations in Chapter 2 from the ones being injected into an approaching laser pulse. The energy differs roughly by a factor of three.

Second, we studied particle-particle interaction effects on the basis of the coupled Lorentz-Newton equations, where we accounted for relativistic effects to $\mathcal{O}(\beta^2)$ on the basis of the Darwin interaction potential. It turned out that particle-particle effects, eventhough being present, are negligible in the presence of strong laser fields of intensities of the order of 10^{24} W/cm^2.

Third, we superimposed two laser fields (first proposed for electrons [31, 32, 37, 38]) to obtain a higher field strength by constructive interference resulting in higher energy gain and better quality of the created proton beams.

In summary, the combination of the laser-plasma mechanism as a proton source and the post acceleration process by means of single or crossed laser beams places laser acceleration of particles on the cusp of medical feasibility utilizing (present-day or) near-future laser technology [6, 7, 87], while anticipated costs are presently on the scale of those for current synchrotron facilities (cf. [14] and [93]). The rapid advancement of laser technology renders significant reduction likely for the near future. All requirements needed may be achieved: sufficient proton density and exit kinetic energies, and sharp energy spread of approximately 1 %. The scheme that we introduce in the present work calls for

tight focusing mechanisms [5] and relies on results of laser-plasma-interaction research [51–53, 58].

Chapter 4

Chirped laser-plasma interaction

Interaction of a frequency-chirped laser pulse with single protons and a hydrogen gas target is studied analytically and by means of two-dimensional particle-in-cell simulations, respectively. Feasibility of generating intense (10^7 particles per bunch) and phase-space collimated beams of protons (energy spread of about 1%) is demonstrated. The quasi-static laser pulse components, guaranteed by the appropriate chirping of the laser pulse, allow the particles to gain sufficient kinetic energy (around 250 MeV) required for such applications as hadron cancer therapy, from state-of-the-art laser systems of intensities of the order of 10^{21} W/cm^2. Furthermore, very collimated beams with a divergence angle of 2° only are created. Parts of this Chapter have been published in Ref. [94].

4.1 Introduction

In this Chapter, we demonstrate the theoretical feasibility of creating proton beams, of unprecedented energy and quality, from illuminating a hydrogen gas target with an appropriately chirped laser pulse [66–68] of intensity accessible by state-of-the-art laser systems [5]. The basic idea of our model stems from the realization that an incoming highly relativistic laser pulse quickly ionizes hydrogen in the cell and accelerates the electrons away from the much heavier protons, as the pulse intensity rises. At high enough laser intensities the protons get accelerated directly by the laser field. See Fig. 4.1 for a schematic. The strong chirping of the laser pulse introduces quasi-static pulse components leading to efficient proton energy gain from such fields.

We derive an expression for the energy transfer during interaction of a particle with chirped unfocused as well as pulsed electromagnetic fields. Results obtained analytically for the particle's energy gain will be supported by further simulations which describe the focused fields more accurately than the simple plane-wave model. Our two-dimensional (2D) particle-in-cell (PIC) simulations

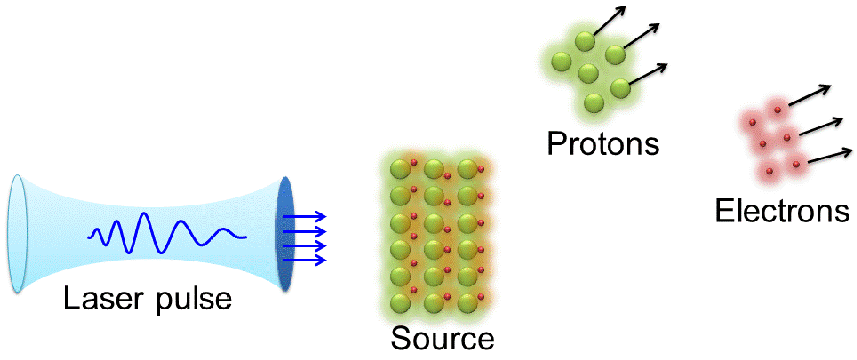

Figure 4.1 – Schematic [95] of the chirped-laser plasma interaction: The impinging chirped laser pulse ionizes the hydrogen gas target leading to an electron blow-off. The remaining protons become subsequently captured and accelerated by the laser pulse.

(cf. Ref. [69] for a review about the method) reveal that proton beams of energy around 250 MeV, energy spread of about 1%, and density of 10^7 particles per bunch, can be produced. Beams of such quality may potentially be suitable for use in hadron cancer therapy assuming the laser-plasma interaction can take place close to the patient [20]. Following acceleration, the beams have to be collimated and guided [96] to compensate larger variations in the laser pulse and its chirp which is still challenging to control at high intensities. Future laser systems at the ELI or HiPER facilities [6, 7] may be utilized to produce monoenergetic multi-GeV proton beams.

This Chapter is organized as follows. In Sect. 4.2 we derive the dynamics of a charged particle in a chirped plane wave field. Then, in Sect. 4.3, we put the plane wave model to the test while comparing it with the dynamics in focused fields. Additionally, we derive the optimal chirp parameter. We continue with the introduction of the particle-in-cell method in Sect. 4.4. The results of the multi-particle simulations are given in Sect. 4.5. We conclude in Sect. 4.6.

4.2 Analytical plane wave model

A point particle of mass M and charge Q acquires relativistic energy and momentum, respectively, of $\mathcal{E} = \gamma Mc^2$ and $\boldsymbol{p} = \gamma Mc\boldsymbol{\beta}$, where $\boldsymbol{\beta}$ is the velocity of the particle scaled by c, the speed of light in vacuum, and $\gamma = (1-\beta^2)^{-1/2}$, when interacting with the fields $\boldsymbol{E}$ and $\boldsymbol{B}$ of an intense laser pulse. It suffices in many applications to represent the fields of the beam by plane waves. A plane wave propagating along the $z-$axis and polarized along the $x-$axis, may be represented by $\boldsymbol{E} = \hat{\boldsymbol{x}} E_0 f$ and $\boldsymbol{B} = \hat{\boldsymbol{y}} E_0 f/c$. As in the previous Chapters, the

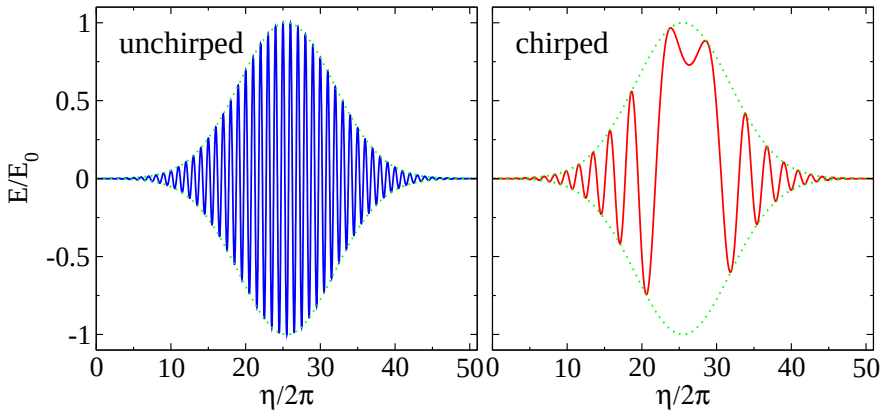

Figure 4.2 – The normalized electric field at focus of a plane-wave pulse employing Eq. (4.6). The parameters used are: $\lambda = 1$ μm, and $\tau = 50$ fs, $\phi_0 = 0$ and $\bar{\eta} = 4s$.

dynamics of the charged particle is described by the Lorentz-Newton equations (SI units) [62, 80]

$$\frac{d\boldsymbol{p}}{dt} = Q\left(\boldsymbol{E} + c\boldsymbol{\beta} \times \boldsymbol{B}\right); \quad \frac{d\mathcal{E}}{dt} = Qc\boldsymbol{\beta} \cdot \boldsymbol{E}. \tag{4.1}$$

The dependence in f on the space-time coordinates is through the combination $\omega t - kz$, with ω being the frequency and $k = \omega/c$ the wave number. This leads to a break-up of the energy-momentum transfer equations (Eqs. 4.1) into four-component equations, namely[1],

$$\frac{d}{dt}(\gamma\beta_x) = a\omega_0(1-\beta_z)f, \quad \frac{d}{dt}(\gamma\beta_y) = 0, \tag{4.2}$$

$$\frac{d}{dt}(\gamma\beta_z) = a\omega_0\beta_x f, \quad \frac{d\gamma}{dt} = a\omega_0\beta_x f, \tag{4.3}$$

where $a = QE_0/(Mc\omega_0)$ is the normalized laser field strength and ω_0 will be defined below. From the second of Eqs. (4.2) we immediately identify a first constant of the motion, namely, $\gamma\beta_y = c_1$. Furthermore, the constant $\gamma(1-\beta_z) = \gamma_0(1-\beta_{z0}) = c_2$ may be arrived at by subtracting the second of Eqs. (4.3) from the first, and integrating. Substituting the constants c_1 and c_2 via β_y and β_z into $\gamma^{-2} = 1 - (\beta_x^2 + \beta_y^2 + \beta_z^2)$, the following key expression for the energy of the particle, scaled by its rest energy, may be arrived at

$$\gamma = \frac{1 + (\gamma\beta_x)^2 + c_1^2 + c_2^2}{2c_2}. \tag{4.4}$$

The combination $\eta = \omega_0(t - z/c)$ will be used often below. Note that with the help of $d\eta/dt = \omega_0(1-\beta_z)$, the first of Eqs. (4.2) may be formally integrated to give

$$\gamma\beta_x = \gamma_0\beta_{x0} + a\int_{\eta_0}^{\eta} f(\eta')d\eta', \tag{4.5}$$

[1]The compact form of Eqs. (4.2) – (4.7) has been introduced by Y. I. Salamin.

where $\beta_{x0} = \beta_x(\eta_0)$ and $\gamma_0 = (1-\beta_0^2)^{-\frac{1}{2}}$.

Frequency chirping amounts to letting ω vary with time in some fashion. Experimentally, laser pulses with a near-uniform spectral intensity over two octaves are feasible [97]. The phase-coherent synthesis of separate femtosecond lasers [98] and the recent synthesis of multiple optical harmonics [99] put forward lasers with an even wider frequency range. We will work with the linear chirp $\omega = \omega_0 + b_0(t - z/c)$ [66–68], with ω_0 denoting the frequency at $t = 0$ and $z = 0$, and b_0 having a unit of s^{-2}. The chirped frequency thus becomes $\omega = \omega_0(1 + b\eta)$, where $b = b_0/\omega_0^2$ is a dimensionless chirp parameter. Also, dependence of the fields on the space-time coordinates may be rewritten as $\omega t - kz \to \eta + b\eta^2$, and the chirped field function $f(\omega t - kz) \to f(\eta + b\eta^2)$. We will initially work with

$$f = \cos(\phi_0 + \eta + b\eta^2)g(\eta); \quad g(\eta) = \exp\left(-\frac{(\eta-\bar{\eta})^2}{2s^2}\right), \tag{4.6}$$

where ϕ_0 is a constant initial phase, $g(\eta)$ a pulse-shape function, and s is related to the pulse duration τ (full-width at half-maximum) via $s = \omega_0\tau/(2\sqrt{2\ln 2})$. In our calculations, we choose a shift in η in the envelope function $g(\eta)$ denoted by $\bar{\eta} = 4s$. Equation (4.6) models an actual laser pulse where the non-vanishing pulse integral may be compensated by a quasi-static tail[2].

To illustrate the mechanism of acceleration, we show in Fig. 4.2 the normalized electric field E/E_0 as a function of η. Interaction of a particle with the unchirped pulse will result in no energy gain, due to the plane-wave symmetry: gain from a positive part of the field gets canceled by loss to an equally strong negative part. However, the chirping breaks this symmetry. Thus, interaction with the low-frequency (quasi-static) and strong positive part of the chirped pulse, which extends over roughly one half of the pulse duration, results in net energy gain.

For a particle initially ($\eta = \eta_0$) at rest, $c_1 = 0$ and $c_2 = \gamma_0 = 1$. Thus, Eqs. (4.4) and (4.5) give the following expression for evolution in η of the particle kinetic energy

$$K(\eta) = (\gamma - 1)Mc^2 = \frac{Mc^2}{2}(\gamma\beta_x)^2. \tag{4.7}$$

Using the initial conditions and Eq. (4.6), Eq. (4.5) can be analytically integrated in terms of a complex error function:

$$\gamma\beta_x(\eta) = a\frac{s(-1)^{1/4}\sqrt{\frac{\pi}{2}}}{2\sqrt{4b^2s^4+1}}\exp\left[-\frac{4b^2\bar{\eta}^2s^2 + 2ib\left(\bar{\eta}^2 - 2i\bar{\eta}s^2 + s^4\right) + s^2}{8b^2s^4+2}\right]$$
$$\times\left\{e^{-i\phi_0}\sqrt{2bs^2+i}\exp\left[\frac{i(-\bar{\eta}+2bs^4)}{4b^2s^4+1}\right]\mathrm{erfi}\left[\frac{(-1)^{1/4}\left(\bar{\eta} - i\left(s^2(2b\eta+1) - i\eta\right)\right)}{s\sqrt{4bs^2-2i}}\right]\right.$$
$$\left.+ie^{i\phi_0}\sqrt{2bs^2-i}\exp\left[\frac{i\bar{\eta}(1+2b\bar{\eta})}{4b^2s^4+1}\right]\mathrm{erfi}\left[\frac{(-1)^{3/4}\left(\bar{\eta} + i\left(s^2(2b\eta+1) + i\eta\right)\right)}{s\sqrt{4bs^2+2i}}\right]\right\}\Bigg|_{\eta_0}^{\eta} \tag{4.8}$$

[2]For a formal discussion on the experimental realization of such a pulse, we refer to Sect. 4.5.3.

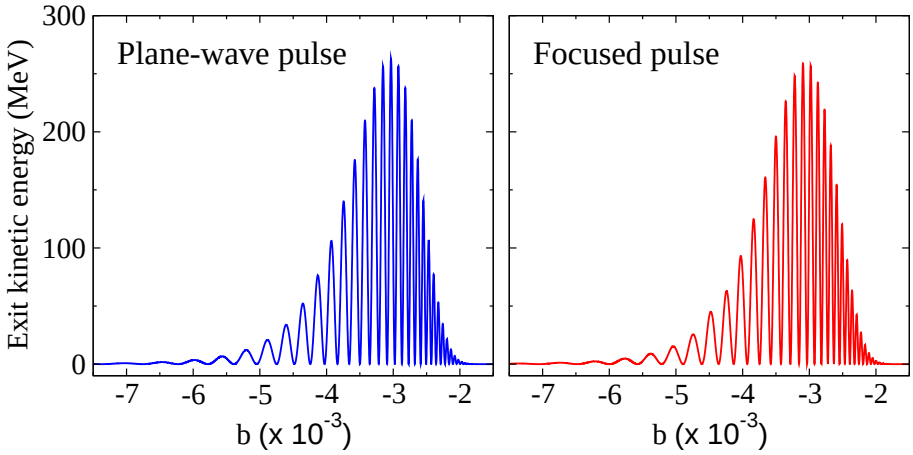

Figure 4.3 – Exit kinetic energy gained by one proton as a function of the dimensionless chirp parameter b in the limit of large η. For the plane-wave pulse the optimal chirp parameter is $b \sim -0.003033$ and $K_{exit} \sim 262.933$ MeV, while for the focused pulse $b \sim -0.002979$ and $K_{exit} \sim 256.959$ MeV. All other parameters are the same as in Fig. 4.4.

Thus, Eq. (4.7) gives the kinetic energy of the particle explicitly, and helps us determine the value of the chirp parameter b that maximizes it. Note from Eqs. (4.5) and (4.7) that the proton energy scales linearly with the laser intensity.

4.3 Focused laser fields and optimal chirp parameter

In order to test the applicability of the analytic plane-wave model, we compare results based on it with those stemming from the use of focused laser fields. For the focused fields, the Lax series expressions will be adopted, according to which all components E_x, E_y, E_z, B_y, and B_z [63] are given in powers of the diffraction angle $\varepsilon = \lambda/\pi w_0$, where w_0 is the waist radius of the beam at focus. Simulations are performed to solve the equations of motion numerically for a single proton submitted to the laser fields from an initial position of rest at the origin of coordinates ($\eta_0 = 0$). In the simulations, $w_0 = 5\lambda$ gives $\varepsilon = 1/5\pi \ll 1$. Hence, terms in the Lax series up to $\mathcal{O}(\varepsilon^2)$ only need to be retained. The simulations demonstrate clearly that the two models predict exit kinetic energies that agree to within 2−3%, see Fig. 4.3. The linear scaling of the exit kinetic energy with the laser intensity given by the plane-wave model only holds true for intensities up to about 5×10^{21} W/cm^2. For highly relativistic particles the exit kinetic energy scales as the square root of the laser intensity, which is the case in conventional TNSA [53], too.

In Fig. 4.4 the exit kinetic energy K of a single proton is displayed as a function of b in the limit of large η. The energy gain is found to peak globally at the

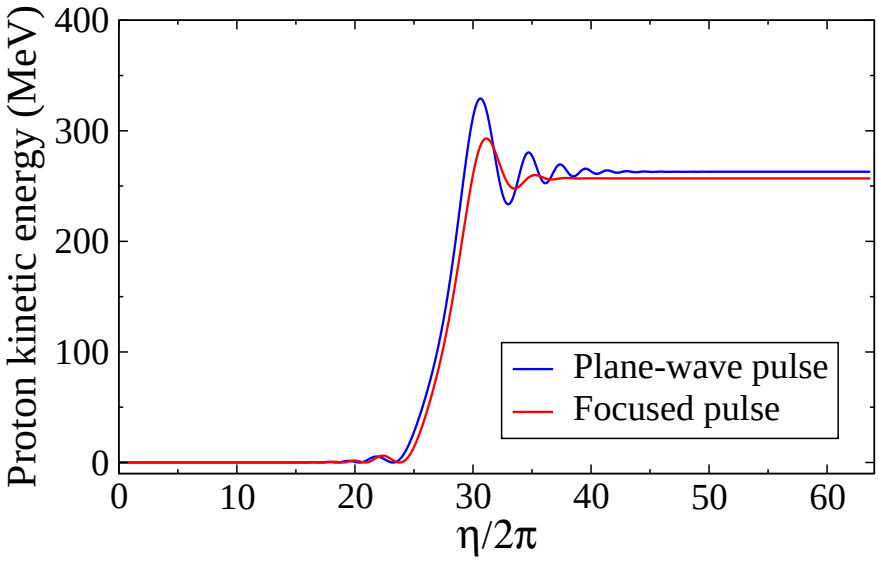

Figure 4.4 – Evolution in η of the kinetic energy of one proton. The peak power P of the employed laser system is 1 PW, which corresponds to a peak intensity of 2.54×10^{21} W/cm^2 (being defined as $I_p = 2P/\pi w_0^2$ [100] throughout this Chapter) for $w_0 = 5\lambda$, $\tau = 50$ fs, and $\lambda = 1$ μm. Other parameters used are: $\phi_0 = 0$, and $\bar{\eta} = 4s$.

chirp parameter values of $b \sim -0.003033$ and -0.002979 for the plane-wave and focused pulses, respectively, and for the specific laser system parameter set used. Other optimal chirp parameter values, which can be determined in like fashion, lead to local, less pronounced kinetic energy maxima. The fact that the optimal values of b are so close (and so are the corresponding exit kinetic energies) demonstrates that the analytic solution is quite reliable and that the plane-wave representation closely describes the physics involved, at least for the parameter set used in which $w_0 \gg \lambda$. On the other hand, it is obvious that dependence upon b of the exit particle kinetic energy is sensitive, especially in the regime where high energy is sought. In fact, the plane-wave calculation yields the uncertainty $\delta K \approx 1/2(\partial^2 K/\partial b^2)|_b(\delta b)^2$, which results from an uncertainty $\delta b \sim 10^{-6}$ in determining b. The plane-wave calculation yields $\delta K \sim 0.195$ MeV, or about 0.074%. When one takes $\delta b \sim 10^{-5}$ instead, the uncertainties increase by two orders of magnitude ($\delta K \sim 19.5$ MeV and 7.4%).

4.4 The Particle-In-Cell method

Before coming to the results of our multi-particle simulations, we introduce the particle-in-cell method (cf. Ref. [69] for a review) to the reader. As it is depicted in Fig. 4.1, the starting point of our simulations in this Chapter is a neutral electromagnetic plasma. Thus two questions may arise:

1. How can one model such an interacting system, in particular in the presence of an impinging laser pulse, which leads to relativistic particle dynamics and the related effects?

2. Having in mind that we aspire towards the creation of dense particle beams, we need an electromagnetic plasma of high particle densities in the excess of 10^{20} particles/cm^3. How could one minimize the computational efforts of modeling such a system?

Let us answer these questions. Due to the long-range Coulomb interaction between the charges, it is clear that a typical collision-based approach would not work here, as singularities would arise. Vlasov circumvented this [101, 102] by introducing a particle distribution function which we denote by $f_{i,e}(\boldsymbol{r}, \boldsymbol{v})$[3], where the subscript i stands for ions and the subscript e for electrons, respectively. The Vlasov evolution equation for the distribution function is given by

$$\frac{\partial f_{i,e}}{\partial t} + \boldsymbol{v} \cdot \frac{\partial f_{i,e}}{\partial \boldsymbol{r}} + \boldsymbol{F}_{i,e} \cdot \frac{\partial f_{i,e}}{\partial \boldsymbol{p}} = 0. \tag{4.9}$$

We are concentrating on electromagnetic plasmas only, hence the force $\boldsymbol{F}_{i,e}$ entering Eq. (4.9) is given by the Lorentz force [80]

$$\boldsymbol{F}_{i,e} = q_{i,e} \left(\boldsymbol{E} + \boldsymbol{v} \times \boldsymbol{B} \right). \tag{4.10}$$

Through the Lorentz force the charged particle dynamics is coupled to Maxwell's equations, which read in SI units (cf. Ref. [80]):

$$\begin{aligned} \nabla \cdot \boldsymbol{B} &= 0 && (4.11)\\ \nabla \times \boldsymbol{E} + \frac{\partial B}{\partial t} &= 0 && (4.12)\\ \nabla \cdot \boldsymbol{E} &= \frac{\rho}{\epsilon_0} && (4.13)\\ \nabla \times \boldsymbol{B} - \mu_0 \epsilon_0 \frac{\partial \boldsymbol{E}}{\partial t} &= \mu_0 \boldsymbol{j} && (4.14) \end{aligned}$$

ϵ_0 is the permittivity and μ_0 the permeability of vacuum, respectively. The latter two Maxwell equations contain the sources that can be recovered from the distribution functions:

$$\begin{aligned} \boldsymbol{j} &= \sum_{i,e} q_{i,e} \int f_{i_e} \boldsymbol{v} d^3\boldsymbol{v}, && (4.15)\\ \rho &= \sum_{i,e} q_{i,e} \int f_{i,e} d^3\boldsymbol{v}. && (4.16) \end{aligned}$$

Even for the simplest cases, this complicated system of coupled partial differential equations is cumbersome to solve. As a consequence, in the 1960s a more

[3] Normally the distribution has to be normalized. Here it is just for illustration purposes.

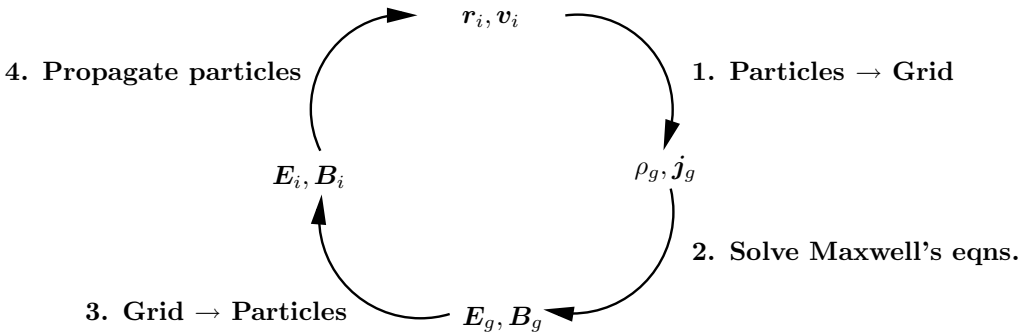

Figure 4.5 – Illustration of the particle-in-cell method (adapted from Fig. 6.7 of Ref. [26]).

applicable method to tackle plasma dynamics has been developed [26], the so-called particle-in-cell (PIC) method. The basic principle of this method is to replace the particle distribution function by so-called quasi- or super-particles of mass m_i and charge q_i. Due to the high number of charged particles in a dense plasma, each quasi-particle of course does not represent a single real particle, but rather a couple of particles.

After discretization of the distribution function $f_{i,e}$, the N quasi-particles can be simply propagated by means of the Lorentz-Newton equation [80]

$$\frac{d}{dt}\boldsymbol{p_i} = q_i(\boldsymbol{E} + \boldsymbol{v}_i \times \boldsymbol{B}), \tag{4.17}$$

with $i = 1 \ldots N$. To solve these equations, we have to solve Maxwell's equations, hence, we need the electromagnetic source terms $\rho(\boldsymbol{r})$ and $\boldsymbol{j}(\boldsymbol{r})$. Computational effort can be further minimized by introducing a spatial grid. Then, the electromagnetic source terms are mapped onto the grid via [26]

$$\begin{aligned} \rho(\boldsymbol{r}) &= \sum_j q_j S(\boldsymbol{r_j} - \boldsymbol{r}), \\ \boldsymbol{j}(\boldsymbol{r}) &= \sum_j q_j \boldsymbol{v}_j S(\boldsymbol{r_j} - \boldsymbol{r}), \quad j = 1 \ldots N_{cell}, \end{aligned} \tag{4.18}$$

where $S(\boldsymbol{r_j} - \boldsymbol{r})$ is the weighting function and N_{cell} is the total number of cells [26]. For most practical purposes it is sufficient to employ a linear weighting function, that maps the particles' charges and currents to the grid. Now, Maxwell's equations can be integrated numerically on the grid. Afterwards, the electromagnetic fields at the particle positions may be obtained by using again the weighting function. Eventually, Eqs. 4.17 are applied to propagate the particles. This cyclic procedure is illustrated in Fig. 4.5. For further details on the PIC method, we refer to Ref. [69].

For the subsequent simulations we use a version of the UMKA2D3V code [103–105] adapted for our purposes, i.e., changing the initial distribution of the quasi-particles and introducing the above described chirped laser pulse. It is a fully

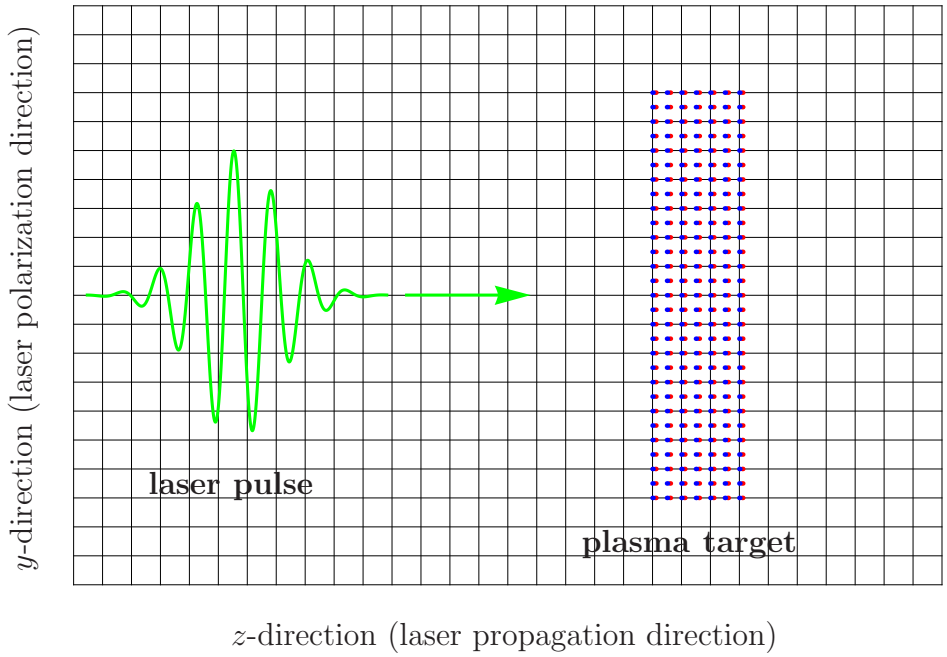

Figure 4.6 – Schematic illustration of the particle-in-cell simulation environment.

kinetic electromagnetic two-dimensional PIC code with three momentum-space degrees of freedom. The spatial dimensions are restricted to the propagation-polarization plane of the incident laser. The numerical realization of advancing the electromagnetic fields, is treated in UMKA2D3V via a finite-difference second-order Yee scheme, which is defined by the following [106]:

$$(\boldsymbol{E}^{n+1} - \boldsymbol{E}^{n})/\Delta t = \nabla^{+} \times \boldsymbol{B}^{n+1/2} - \boldsymbol{j}^{n+1/2}, \tag{4.19}$$

$$(\boldsymbol{B}^{n+1/2} - \boldsymbol{B}^{n-1/2})/\Delta t = -\nabla^{-} \times \boldsymbol{E}^{n}, \tag{4.20}$$

$$\nabla^{+} \cdot \boldsymbol{E}^{n} = \rho^{n}, \tag{4.21}$$

$$\nabla^{-} \cdot \boldsymbol{B}^{n+1/2} = 0. \tag{4.22}$$

The vector representation of the electromagnetic fields on the spatial grid is defined via $\boldsymbol{E}^{n} \equiv E^{n}_{i,j}$ [106], where the space-time coordinates can be restored as $z = i \cdot \Delta z$, $y = j \cdot \Delta y$ and $t = n \cdot \Delta t$, with Δz, Δy being the spatial resolution and Δt the temporal resolution, respectively [106]. The partial derivatives of the nabla operators are defined as [106], e.g.,

$$\partial_z^{+} E^{n}_{i,j} \equiv E^{n}_{i+1,j} - E^{n}_{i,j}/\Delta z, \tag{4.23}$$

$$\partial_z^{-} E^{n}_{i,j} \equiv E^{n}_{i,j} - E^{n}_{i,j-1}/\Delta z. \tag{4.24}$$

In UMKA2D3V, rescaled units are used of the form [106]

$$\text{time} \rightarrow \text{time}/\frac{2\pi}{\omega_0}, \tag{4.25}$$

$$\text{length} \rightarrow \text{length}/\lambda, \tag{4.26}$$

$$\text{electric field} \rightarrow \text{electric field}/\frac{m_e c\omega_0}{2\pi e}, \tag{4.27}$$

$$\text{electron/ion density} \rightarrow \text{electron/ion density}/\frac{m_e\omega_0^2}{16\pi^3 e^2}. \tag{4.28}$$

To propagate the particles, a second order leap-frog scheme is used in UMKA2D3V, that turns the Lorentz-Newton equations into [106]

$$(\boldsymbol{u}^{n+1/2} - \boldsymbol{u}^{n-1/2})/\Delta t = q_\alpha/m_\alpha \cdot \left(\boldsymbol{E}(\boldsymbol{x}_\alpha^n, t) + \frac{\boldsymbol{u}_\alpha^n}{\gamma_\alpha} \times \boldsymbol{B}^n(\boldsymbol{x}_\alpha^n, t)\right), \tag{4.29}$$

$$(\boldsymbol{x}^{n+1} - \boldsymbol{x}^n)/\Delta t = \frac{\boldsymbol{u}_\alpha^{n+1/2}}{\gamma_\alpha^{n+1/2}}, \tag{4.30}$$

where Greek indices denote particles.

The simulation environment is sketched in Fig. 4.6. The laser pulse (green) enters the simulation box (illustrated as a spatial grid) from the left and is propagated through vacuum until it reaches the left edge of the plasma target, which is modeled by positively (red points) and negatively (blue points) charged quasi particles.

4.5 Results

Having studied the single-particle aspects and the basic principles of the PIC algorithms, we now present typical simulation results of the interaction of the chirped laser pulse with a pre-ionized hydrogen target. The target might be either an expanding hydrogen cluster available at sizes ranging from 1 nm to 1 μm [107] or part of a hydrogen gas jet. We are using the following simulation environment: The spatial resolution of our simulation box is given by $\Delta z = \Delta x = \lambda/100$, where the laser wavelength is still assumed to be $\lambda = 1$ μm. The particle number per cell is 100 both for protons and electrons. The x-polarized laser enters the simulation box from the left and propagates in the z-direction. For the fields used to calculate the exit kinetic energy distribution (see. Fig. 4.9), we choose a simple modification of the plane wave fields given by $\boldsymbol{E} = \hat{\boldsymbol{x}} E_0 f e^{-x^2/(2w_0^2)}$ and $\boldsymbol{B} = \hat{\boldsymbol{y}}(E_0/c) f e^{-x^2/(2w_0^2)}$, with f from Eq. (4.6) and the factor $e^{-x^2/(2w_0^2)}$ mimicking spatial focusing in the polarization direction. The target dimensions are assumed to have a length of 0.2λ in the laser propagation direction, and an extension of 0.6λ in the transverse direction. Here, we assume the electrons (in the hydrogen gas) to be underdense $n_e = 0.1\ n_c$, where $n_c = 1.1 \times 10^{21}$ cm^{-3} is the critical density for the wavelength of $\lambda = 1\mu$m. For the protons, the total number per shot being accelerated as one bunch amounts to $\approx 10^7$.

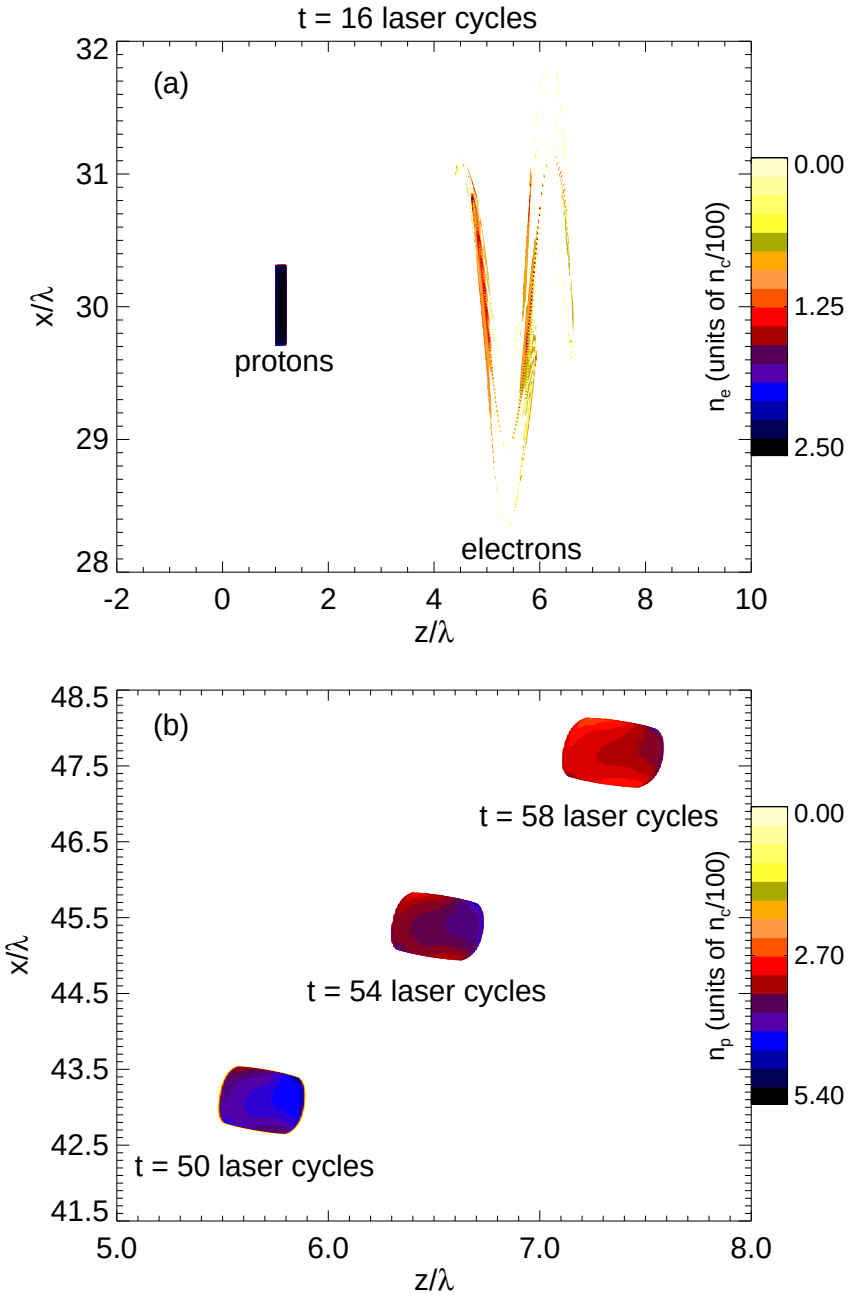

Figure 4.7 – Snap-shots (a) of the electron and proton density distribution during laser–plasma interaction and (b) of the proton density distribution after laser–plasma interaction for various times. The laser peak intensity is 2.54×10^{21} W/cm^2.

4.5.1 Plasma dynamics and beam divergence

Fig. 4.7 provides an insight into the acceleration mechanism and the plasma dynamics. From Fig. 4.7 (a), one can see that when the laser pulse approaches the gas target, the electrons get blown off the target. The density profile of the electrons follows approximately the laser field oscillations. At this time ($t = 16$ laser cycles), the proton distribution almost maintains its initial shape. After

pulse length	5% longer	10% longer	5% shorter	10% shorter
emission angle	69.4°	69.4°	71.2°	73.4°
initial phase	+1°	+3°	+5°	+10°
emission angle	69.9°	69.9°	70.0°	70.3°
target dimension	2×	3×	2×	3×
	in propagation direction		in polarization direction	
emission angle	69.9°	69.9°	70.0°	70.2°

Table 4.1 – Effects of the variation in the pulse parameters and the initial target's dimension on the proton bunch emission angle. The data were calculated in the framework of the non-interacting proton ensemble.

the interaction of the gas target with the laser pulse, one can see from Fig. 4.7 (b) that the protons are accelerated as a symmetric bunch of homogeneous density (average density at $t = 50$ laser cycles: $\bar{n}_p \approx 0.04\ n_c$). Note that the proton bunch is emitted at 70° relative to the laser propagation direction (z-direction).

The control of laser systems in the excess of 10^{21} W/cm^2 is a rather challenging experimental problem. Probably, not every single laser shot is reproducible at the same parameters. Due to the fact that our work is motivated by hadron cancer therapy demanding high reproducibility, it would be interesting to know how the emission angle varies with small changes in the laser parameters and in the target dimensions. Investigations on that are summarized in Tab. 4.1.

The table demonstrates that our scheme is quite robust against changes in the initial set of parameters. In order to investigate the beam displacement at the tumor due to variation in the initial conditions, we have to estimate the distance the proton bunch has to travel before arriving at the patient. There have been interesting conceptual design studies of potential laser-plasma accelerators for medical applications. J. Weichsel et al. [20] propose an optical gantry, such that the laser-plasma interaction could take place close to the patient. Assuming this distance to be 30 cm, the displacement at the tumor amounts to approx. 1 mm for a typical small variation of 0.2° in the emission angle. This reaches the precision of current synchrotron facilities used for hadron cancer therapy.

To make the proton beams applicable for larger variations in the emission angle, they have to be focused and guided by conventional means after the laser-plasma interaction has taken place. Recently, this was demonstrated successfully by M. Schollmeier et al. [96]. They managed to focus and collimate a laser-accelerated proton beam with an initial divergence angle of about 60° to a spot diameter of 1 mm.

Due to the comparatively low density of the plasma target and, hence, suppressed Coulomb explosion, the time-dependent beam divergence is low. In order to estimate the spread of the proton ensemble over macroscopic distances, i.e., upon arrival at a patient, we calculated the two-dimensional volume con-

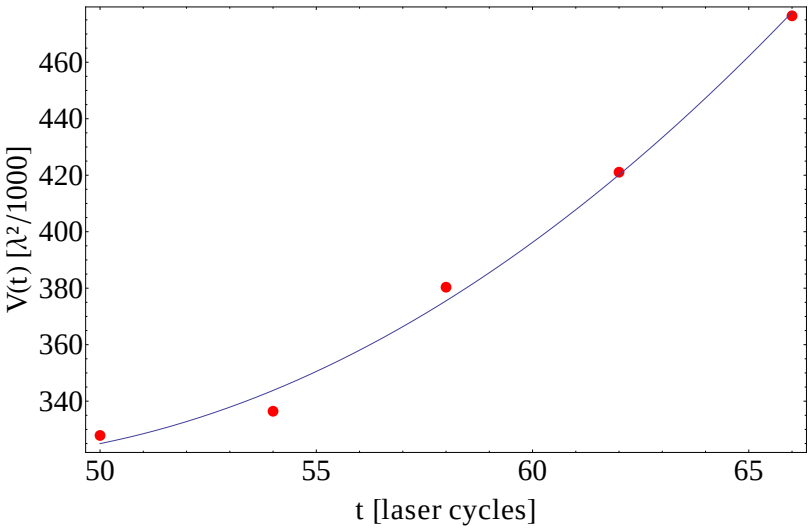

Figure 4.8 – Quadratic fit of the proton beam divergence for further time steps.

taining all protons $V(t)$ at further time steps. We then applied a least-squares fit on the basis of a quadratic function (see Fig. 4.8). We obtained the following function roughly describing the divergence of the particle beam as a function of time, $V(t) = 1179.25 - 37.26t + 0.40t^2$, where $V(t)$ is in units of $\lambda^2/1000$. The time step t has units of laser cycles.

Assuming the proton bunch moving with a kinetic energy of 250 MeV (corresponding to $\beta = 0.61$), and further assuming the patient being located 30 cm away from the laser-plasma interaction, it takes the proton bunch approx. $\delta t = 4.92 \times 10^5$ time steps to arrive at the tumor tissue. Using the above formula, the spread of the proton beam increases to $V(\delta t) \approx 0.98$ cm^2; this number roughly corresponds to a divergence angle (opening angle of the cone defined by the beam) of 2°.

While this number sounds promising and compares well to other laser acceleration schemes, the generated proton beams are not directly applicable for radiotherapy. Following acceleration, the particles need to be focused and guided [96] to render the scheme feasible for tumors of various dimensions and densities. This is probably required in every case whenever ion beams are generated by laser means.

4.5.2 Exit kinetic energy and its spread

In Fig. 4.9 we compare the exit kinetic energy distribution of 3000 initially randomly distributed non-interacting particles (see Chaps. 2 and 3 for the method) in a spatial volume with the same dimensions as the gas target (cf. Fig 4.7 (a)), with the one stemming from the laser – gas target interaction. In the case of pure vacuum acceleration $K = 258.3$ MeV $\pm$ 1.2%, while for the laser-plasma-cell acceleration $K = 245.2$ MeV $\pm$ 0.8%. The small discrepancy

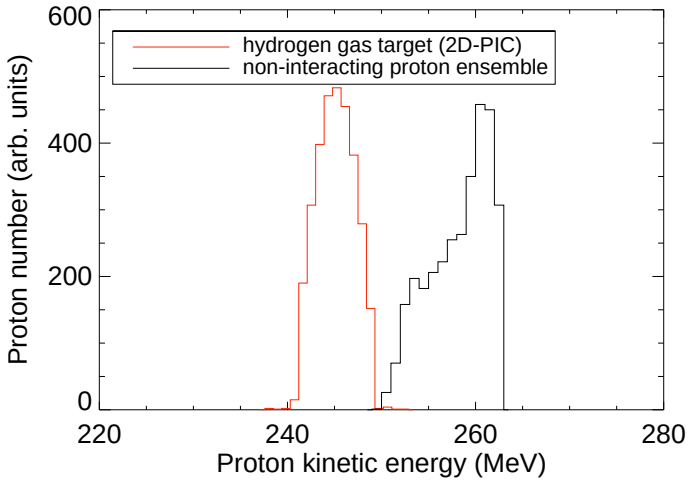

Figure 4.9 – Proton kinetic energy distributions after the interaction of a chirped laser pulse ($b = -0.003033$) with a hydrogen gas target (red) and with an ensemble of protons without particle-particle interaction effects (black). The laser peak intensity is 2.54×10^{21} W/cm^2 and $w_0 = 5\lambda$ for both cases.

between the reported mean kinetic energies is about 5%, which can be attributed to particle-particle interaction effects. Moreover, the simulation of the randomly distributed non-interacting particle ensemble has been carried out in three spatial dimensions, whereas the PIC simulation is two dimensional. Due to the similar values of the exit kinetic energy in both methods, it is obvious that the prevailing part of the proton's kinetic energy is transferred via direct interaction with the laser field.

To study the effect of shooting on more common gas targets of larger spatial extent such as hydrogen gas jets, we performed further simulations summarized in the table below. We studied two possibilities to enlarge the gas target, namely, in polarization and propagation directions. In both cases the energy spread increases and the mean energy decreases slightly.

enlargement of initial distribution	2×	3× energy (MeV)	5×
in pol. direction	$250.8 \pm 2.9\%$	$244.9 \pm 4.6\%$	$228.4 \pm 9.4\%$
in prop. direction	$254.3 \pm 1.4\%$	$251.1 \pm 2.5\%$	$245.1 \pm 5.4\%$

Table 4.2 – Variation of the plasma distribution's dimensions (initially 0.6λ in pol. direction and 0.2λ in prop. direction) with resulting mean kinetic energy and percentage energy spread. Other parameters are as in the captions of Fig. 4.4. The data were calculated in the framework of the non-interacting proton ensemble.

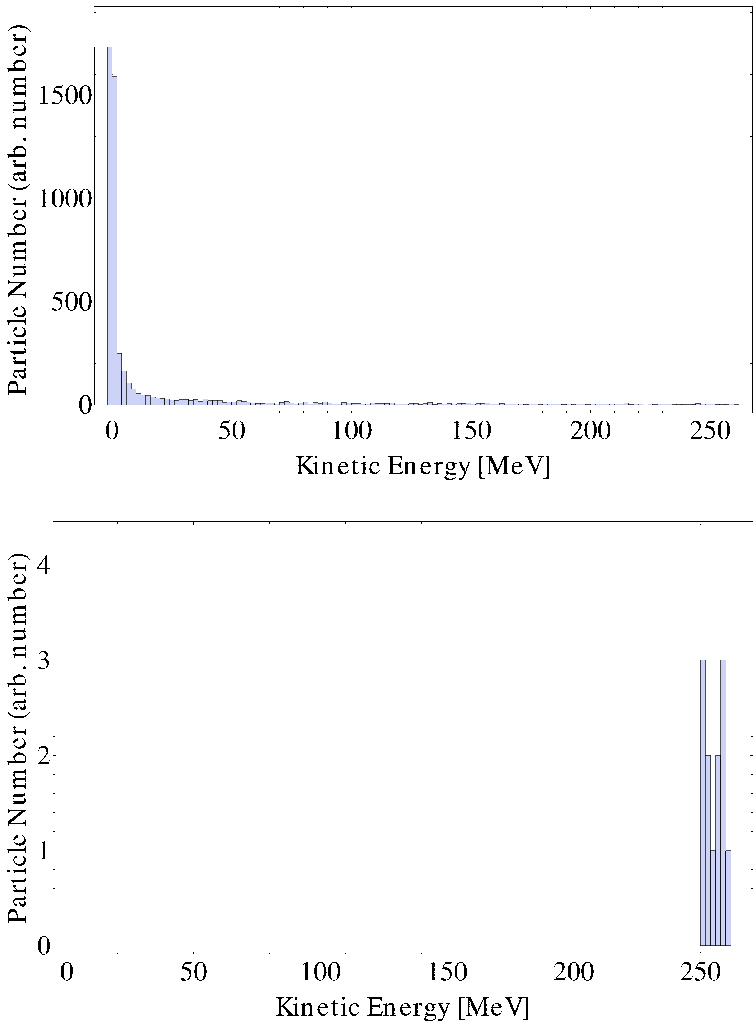

Figure 4.10 – (a) Histogram showing the spectrum for a large initial distribution. (b) Histogram for the particles with $E_{kin} > 250$ MeV. The data were calculated in the framework of the non-interacting proton ensemble.

In case of enlarging the target in polarization direction, the exponential intensity gradient of the focused fields explains this behavior: particles at different positions are exposed to laser fields of different strengths. However, we want to emphasize that even for a considerable increase of the target dimensions one could still produce proton beams for applications, employing some velocity filtering after the laser-plasma interaction. Figure 4.10 (a) shows the spectrum from shooting on a target which was increased by a factor of 40 along the transverse directions. In this case, most particles, i.e., the ones outside of the focus are certainly not accelerated at all. Cutting the spectrum at a threshold energy of $E_{thresh.} = 250$ MeV yields a monoenergetic spectrum with an energy spread of about 3% of the remaining particles (cf. Fig. 4.10 (b)). Although only a small fraction of the total number of particles are within this range, there are still about 10^7 particles accelerated in one bunch. As a consequence, it seems to be sufficient to study the interaction of a chirped laser pulse with a small

plasma target only.

In case of enlarging the target in propagation direction of the laser pulse, the energy spread increases as well. Here, it is not possible to enlarge the target arbitrarily. Otherwise the electrons located at the rear surface are pushed into the neighboring plasma, leading to different acceleration dynamics not covered anymore by our model. The target thickness allowed is in the range of a few micrometers (cf. second line Tab. 4.2), which may be implemented as a gas jet generated by a micro-nozzle.

In order to reach similar particle energies as given above by using an unchirped laser pulse one would have to raise the laser intensity by three orders of magnitude, to $10^{24}\mathrm{W/cm}^2$. At such an intensity the chirped laser scheme (employing the same parameters as in Fig. 4.4) already yields monoenergetic proton beams with $K = 17.3$ GeV $\pm$ 1.0%. This value was calculated in the framework of the non-interacting proton ensemble.

4.5.3 The pulse form $f(\eta)$, its frequency spectrum and the underlying acceleration mechanism

In this subsection we discuss the realization of the pulse form $f(\eta)$ introduced in Eq. (4.6). For an electromagnetic pulse purely consisting of oscillating components, the integral over the pulse form has to vanish. This is not the case for the pulse form as given by Eq. 4.6, hence, it contains a static component. In order to realize our pulse as being composed of purely oscillating components, we have to remove the static zero-frequency component from its frequency spectrum. First, we have to calculate the Fourier transform of the pulse form $f(\eta)$ denoted by $\tilde{f}(\tilde{\eta})$ in order to obtain the frequency spectrum being defined as $|\tilde{f}(\tilde{\eta})|^2$. We denote the Fourier transformed variable of η by $\tilde{\eta}$. Recall that for the coordinate $z = 0$, η is linearly related to the laser frequency $\eta = \omega_0 t$ and it is $\tilde{\eta} = \omega/\omega_0$. We work with the symmetric Fourier transform given by

$$\tilde{f}(\tilde{\eta}) \equiv \frac{1}{\sqrt{2\pi}} \int_{-\infty}^{\infty} f(\eta) e^{i\tilde{\eta}\eta} d\eta. \tag{4.31}$$

For the specific $f(\eta)$ from Eq. (4.6) the Fourier transform can be carried out fully analytically based on the assumptions $b < 0$, $s > 0$, $\bar{\eta} > 0$:

$$\begin{aligned}\tilde{f}(\tilde{\eta}) \;=\; & \frac{\mathrm{Cosh}\left[\frac{-2\bar{\eta}(1+b\bar{\eta}-\tilde{\eta})+is^2(-1+\tilde{\eta})^2}{-2i+4bs^2}\right]}{2\sqrt{2ib+\frac{1}{s^2}}} + \frac{\mathrm{Cosh}\left[\frac{is^2(1+\tilde{\eta})^2+2\bar{\eta}(1+b\bar{\eta}+\tilde{\eta})}{2i+4bs^2}\right]}{2\sqrt{-2ib+\frac{1}{s^2}}} \\ + \; & \frac{\mathrm{Sinh}\left[\frac{-2\bar{\eta}(1+b\bar{\eta}-\tilde{\eta})+is^2(-1+\tilde{\eta})^2}{-2i+4bs^2}\right]}{2\sqrt{2ib+\frac{1}{s^2}}} - \frac{\mathrm{Sinh}\left[\frac{is^2(1+\tilde{\eta})^2+2\bar{\eta}(1+b\bar{\eta}+\tilde{\eta})}{2i+4bs^2}\right]}{2\sqrt{-2ib+\frac{1}{s^2}}}\end{aligned} \tag{4.32}$$

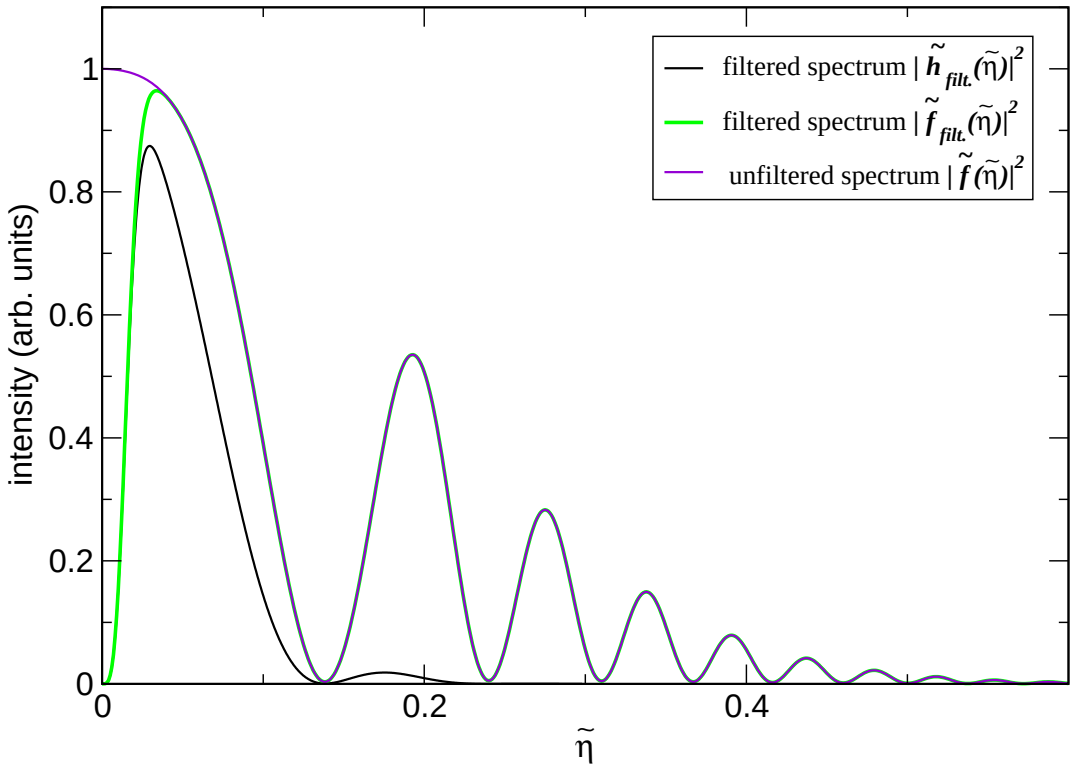

Figure 4.11 – Frequency spectrum with applied low-frequency filter ($\Delta = 0.01$) (green curve), with applied low- ($\Delta = 0.01$) and high- ($\delta = 0.01$) frequency filters (black curve) and without filter (violet curve). The Fourier transformed variable is $\tilde{\eta} = \omega/\omega_0$.

To cancel the static component one can multiply $\tilde{f}(\tilde{\eta})$ simply by a filter function, e.g.,

$$g_1(\tilde{\eta}) = 1 - e^{-\frac{\tilde{\eta}^2}{2\Delta^2}}, \tag{4.33}$$

where the width Δ (in units of ω/ω_0) introduces a smooth cut-off to the lower frequency part of the spectrum (see Fig. 4.11). The filtered spectrum ($|\tilde{f}_{\text{filt.}}(\tilde{\eta})|^2$) may then be defined via

$$\tilde{f}_{\text{filt.}}(\tilde{\eta}) \equiv g_1(\tilde{\eta})\tilde{f}(\tilde{\eta}). \tag{4.34}$$

In order to determine the total frequency range of a spectrum with the applied filter bandwidth Δ, one has to define minimal and maximal frequencies of the spectrum. A reasonable choice may be frequencies at which the intensity drops down to 1% its peak value, i.e. not influencing particle dynamics. For a filter choice $\Delta = 0.0002$ that leaves the kinetic energy gain almost unchanged (see Fig. 4.12 (b)) it yields $\omega_{\text{min.}} \approx 0.0001\omega_0$ and $\omega_{\text{max.}} \approx 0.6\omega_0$. The peak of the dominant low frequency part is located at $\omega \approx 0.0010632\omega_0$. For our choice of ω_0 it implies frequencies ranging from approx. $\nu_{\text{min.}} = 10$ GHz to $\nu_{\text{max.}} = 100$ THz. The peak of the low frequency part of the spectrum in absolute units is located at $\nu = 0.32$ THz. On the experimental side, such a spectrum may be

thought of as composed from different types of synchronized lasers, e.g. near-infrared and CO_2 laser systems [72], potentially also terahertz lasers. The rapid advancement in larger wavelength lasers and spectral synthesis [108] give hope to availability in near future.

From the intensity distribution of the frequency spectrum in Fig. 4.11 it becomes obvious that a charged particle gains the prevailing part of its kinetic energy from interaction with the low-frequency part of the spectrum. This can be shown by removing the peaks at higher frequencies from the spectrum (black line of Fig. 4.11). Mathematically this may be achieved by introducing another filter function

$$g_2(\tilde{\eta}) = e^{-\frac{\tilde{\eta}^2}{2\delta^2}}. \tag{4.35}$$

The spectrum without peaks at higher frequencies reads then

$$\tilde{h}_{\text{filt.}}(\tilde{\eta}) \equiv g_2(\tilde{\eta})\tilde{f}_{\text{filt.}}(\tilde{\eta}). \tag{4.36}$$

A high-frequency filter of width $\delta = 0.1$ implies a cut-off frequency at $\omega_c \approx 0.12\omega_0$. Note that ω_0 can be related to the scale set by the inverse of the FWHM pulse duration T^{-1}_{FWHM} via $T^{-1}_{\text{FWHM}} = \omega_0/30\pi$. This yields $\omega_c \approx 11.3T^{-1}_{\text{FWHM}}$. The exit kinetic energy gain corresponds in this case to 94% of the unfiltered value.

To arrive at the filtered pulse form factor in η-space we have to apply the inverse Fourier transform defined as

$$\begin{aligned} f_{\text{filt.}}(\eta) &\equiv \frac{1}{\sqrt{2\pi}} \int_{-\infty}^{\infty} \tilde{f}_{\text{filt.}}(\tilde{\eta}) e^{-i\tilde{\eta}\eta} d\tilde{\eta}, \\ h_{\text{filt.}}(\eta) &\equiv \frac{1}{\sqrt{2\pi}} \int_{-\infty}^{\infty} \tilde{h}_{\text{filt.}}(\tilde{\eta}) e^{-i\tilde{\eta}\eta} d\tilde{\eta}. \end{aligned} \tag{4.37}$$

This can also be carried out fully analytically. As an example we give the full expression for $f_{\text{filt.}}(\eta)$ in Appendix A, Eq. (A.2).

In Fig. 4.12 (a) we plot $f_{\text{filt.}}(\eta)$ (blue and green line) for different filter bandwidths Δ. The smaller the filter width becomes, the closer the modified pulse form looks to the original one $f(\eta)$. For $\Delta = 0.0002$, the curve of $f_{\text{filt.}}(\eta)$ and $f(\eta)$ cannot be differentiated on the plot's scale. Furthermore, from Fig. 4.12 (a) (black line) one can see that even without the high frequency part of the spectrum the strong positive part in the center of the pulse remains maintained. In case of a non-optimal choice of the chirp parameter (red line), the positive and negative areas in the center of the pulse cancel partially, resulting in low energy gain.

Figure 4.12 (b) shows the evolution of the kinetic energy for the pulse form factor $f(\eta)$ and for the filtered pulse form factors $f_{\text{filt.}}(\eta)$ and $h_{\text{filt.}}(\eta)$, respectively. The difference in the exit kinetic energy of $f(\eta)$ and $f_{\text{filt.}}(\eta)$ amounts only to approximately 3% and for $f(\eta)$ and $h_{\text{filt.}}(\eta)$ the difference is about 6%. This clearly explains the underlying acceleration mechanism: The large positive (asymmetric) part of the pulse caused by the peak in the low-frequency

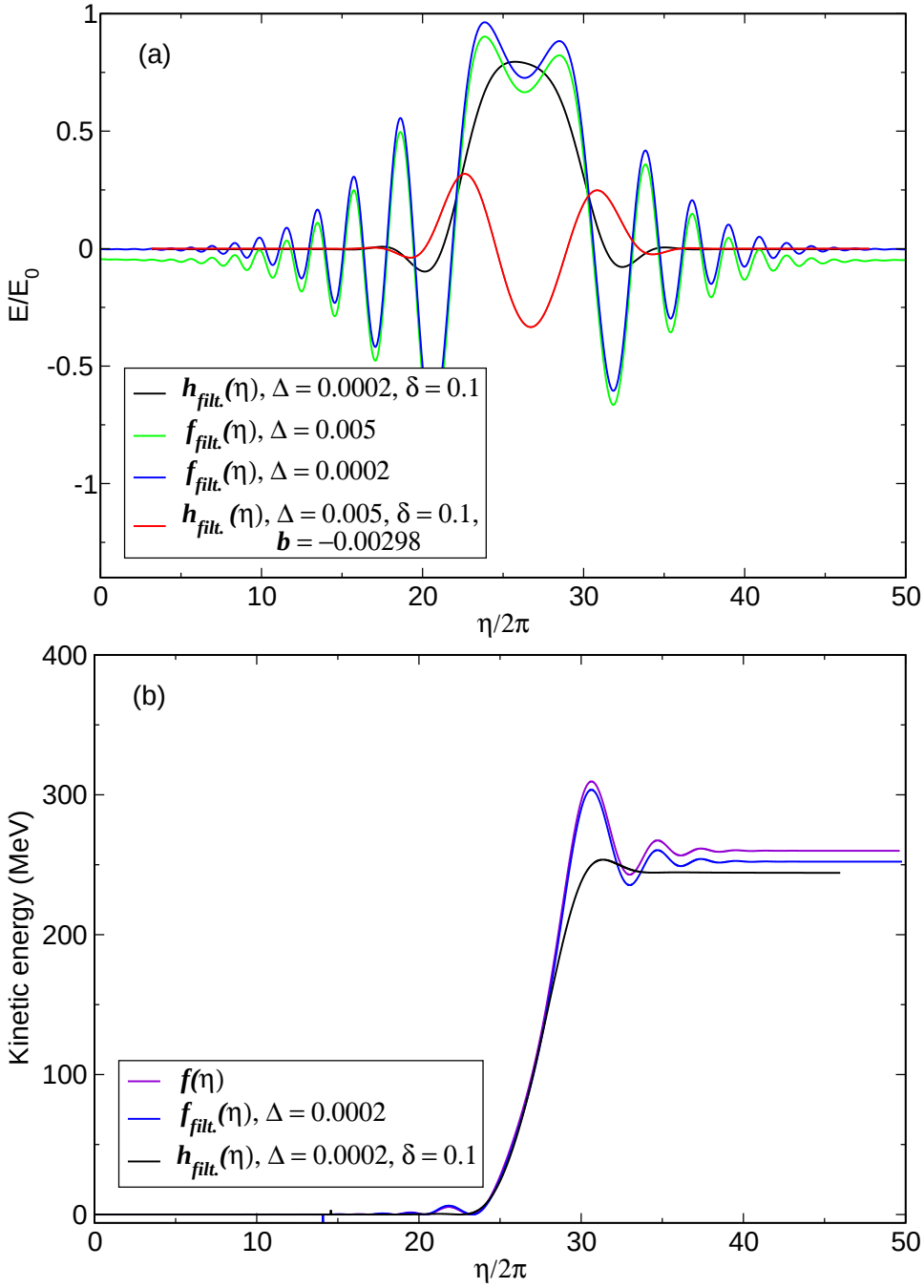

Figure 4.12 – (a) Low-frequency filtered pulse form factor $f_{\text{filt.}}(\eta)$ for different filter widths Δ. High- and low-frequency filtered pulse form factor $h_{\text{filt.}}(\eta)$ for optimal chirp parameter $b = -0.003033$ (black line) and for a non-optimal chirp parameter $b = -0.00298$ (red line). (b) Evolution of the kinetic energy for $f(\eta)$, $f_{\text{filt.}}(\eta)$ and $h_{\text{filt.}}(\eta)$.

part of the spectrum results in net energy gain of the particles. Even for a wider η-range (e.g. $\eta \in [-12s, +12s]$), the exit kinetic energy remains almost unchanged. Hence, it is possible to obtain approximately the same results from a pulse form without a static component.

We may verify that the integral over the filtered pulse form vanishes, as required:

$$\lim_{a\to\infty} \int_{-a}^{a} f_{\text{filt.}}(\eta) d\eta \stackrel{!}{=} 0. \tag{4.38}$$

Whereas the integration can still be carried out analytically (resulting in a large expression), the limiting procedure is to be done numerically with "∞" being replaced by a large number, e.g. $a \to 10^6$. This calculation yields a small numerical value close to 0.

We would like to annotate that in the plane wave case the integration over η from $-\infty$ to $+\infty$ would result in zero energy gain for a particle exposed to a purely oscillating pulse. Hence, Sect. 4.2 only yields a good estimate of the exit kinetic energy for a finite range of integration centered around the strong positive part of the pulse. In an experimental set-up the interaction with the quasi-static negative (decelerating) tail resulting from the above-described filtering of the static component can be circumvented by shooting in the gas jet just shortly before the arrival of the positive part of the laser pulse. In further studies, it would be interesting to study the interaction of the long quasi-static tail with a hydrogen cluster in order to check if and when ionization takes place. In Ref. [41] it was demonstrated that for Highly Charged Ions (HCI) ionization first takes place at the peak of the envelope of the incident laser (at comparable intensities as those used in our set-up), which leads to GeV electron energies.

4.6 Conclusions

In this Chapter we studied the interaction of a frequency-chirped laser pulse with an underdense hydrogen plasma target of spatial extent of the order of the laser wavelength. The electrons are quickly blown off the target, while the more inert protons become subsequently accelerated via direct energy transfer from the quasi-static laser field. We have demonstrated the theoretical feasibility of creating a dense proton beam (10^7 protons per bunch) of high energy ($\approx$ 250 MeV) and good quality (energy spread $\sim 1\%$). The required laser peak intensity of about 10^{21} W/cm^2 is within the range of state-of-the-art high-intensity laser systems [5].

Furthermore, we developed an analytical model for determining the optimal pulse shape and the final kinetic energy of the particles, which is in good agreement with the performed 2D-PIC simulations. The agreement of the kinetic energy with calculations assuming a non-interacting initial ensemble is also within 5%.

Our work has mainly been concerned with proton acceleration to energies and densities required for hadron therapy. Following acceleration, ion beam shaping [96] beyond the scope of this thesis has to be applied.

Chapter 5

Summary and Outlook

We began our theoretical studies in Chapter 2 in the framework of vacuum laser acceleration of charged particles, investigated first for electrons [32, 33] and later for ions [62]. The basic idea is to directly expose a random, non-interacting ensemble of bare nuclei to an intense laser field [62]. We apply laser fields of linear [63] and radial polarization [64, 65, 71, 74]. Key to achieving relativistic laser intensities in the excess of 10^{20} W/cm^2 is the tight focusing to the order of the laser wavelength [62]. The use of long-wavelength CO_2 laser systems leads to an increase by three orders of magnitude in the total particle number per bunch being accelerated, as compared to usual optical lasers with wavelengths around 1 μm. Based on relativistic simulations, we demonstrate the theoretical feasibility of creating ion beams of energies of several hundred MeV having a low energy spread of only 1 %.

In Chapter 3, we study the interaction of a pulsed laser system with a particle source having the typical properties as being created from a laser-plasma interaction process such as TNSA or S-LPA. While in Chapter 2 the particles are assumed to be "born" in the focus of the laser beam at the peak value of its intensity as it might be the case for an ionization process [41], we model a realistic particle injection mechanism in Chapter 3 letting the particle ensemble interact with the full pulse. Schemes in a single- and a crossed-beams [31,32,37,38] configuration are studied. Particle-particle interaction effects are shown to be negligible in the presence of ultra-strong laser fields. We show the theoretical feasibility of creating dense particle beams maintaining the good beam properties of Chapter 2. For the first time, all requirements for broader radio-oncological use are fulfilled based on an all-optical set-up ($I \approx 10^{24}$ W/cm^2).

Chapter is devoted to the study of the interaction of a strongly chirped [66–68] laser pulse with a plasma target. The target is assumed to be an underdense hydrogen plasma with spatial dimensions of the order of the laser wavelength. Interaction between the laser pulse and the target is studied within the numerical framework of two-dimensional PIC simulations (cf. Ref. [69] for a review). This allows for a fully relativistic treatment of the classical dynamical many-body problem of an electromagnetic plasma. Our theoretical investiga-

tions indicate the possibility of creating dense monoenergetic proton beams of low angular divergence while interacting with laser systems of intensities being available at present-day facilities ($I \approx 10^{21}$ W/cm^2). The results of the PIC simulation for the exit kinetic energy agrees on a five-percent level with results obtained from a non-interacting ensemble, letting us conclude that at the intensities used, particle-particle interactions only yield minor contributions to the underlying process [94].

The present work may stimulate further studies in the field. It would be certainly interesting to also investigate the dynamics and the acceleration gradients of electrons being shot into the strong quasi-static fields used in Chapter 4. Also, the Fourier analysis of chirped pulses used in Chapter 4 may be extended to a general ansatz of a laser pulse represented as a superposition of finite frequency components. The amplitudes of the different components may then be numerically optimized to yield a pulse form that maximizes the particles' final kinetic energy. Furthermore, in the light of future high-intensity laser facilities such as ELI [6] or HiPER [7], the interaction of even an unchirped laser pulse with micron-size targets (possibly of spherical symmetry [109]) may reveal further interesting properties for the creation of ion beams. In particular, at intensities exceeding 10^{23} W/cm^2, it was recently shown based on the Landau-Lifshitz propagation equation that radiation back-reaction effects play an important role for linearly polarized laser light [110].

Recently, there arose a discussion about the possibility of creating electron-positron pair cascades at laser intensities $> 10^{24}$ W/cm^2 in particular in the presence of matter [111, 112]. These QED effects lead to laser field absorption and may put limitations the proposed acceleration process. Hence, also further quantum mechanical studies on the underlying concept of laser acceleration would be appealing. Additionally, the interaction of the quasi-static tail preceding the laser pulse applied in Chapter 4 could be investigated quantum mechanically by solving the time-dependent Dirac equation in order to make quantitative predictions about the role of a ionization in the acceleration process.

Furthermore, the dynamics of a highly relativistic electron ensemble in autoresonance acceleration [42], where the frequency of cyclotron motion (caused by a strong static external magnetic field) of the electrons' orbits coincides with the laser frequency, may lead to the emission of intense coherent radiation of short wavelengths. Such autoresonant acceleration and the possibility of creating coherent hard x-ray or gamma radiation may also be studied in the framework of Particle-In-Cell simulations describing the creation of an electron bunch from an underdense gas target in an ab initio manner. Current results indicate a gamma ray spectrum with photon energies of up to 150 keV from electrons undergoing autoresonant betatron motion in a laser wakefield scenario [113].

Appendix A

Inverse Fourier transform

Here we give an analytical expression for the inverse Fourier transform of Eq. (4.34) defined as

$$f_{\text{filt.}}(\eta) \equiv \frac{1}{\sqrt{2\pi}} \int_{-\infty}^{\infty} \tilde{f}_{\text{filt.}}(\tilde{\eta}) e^{-i\tilde{\eta}\eta} d\tilde{\eta}. \tag{A.1}$$

Assuming that $b < 0$, $s > 0$, $\bar{\eta} > 0$ and $\Delta > 0$, this yields

$$\begin{aligned}
f_{\text{filt.}}(\eta) &= \frac{1}{2}\cos\left[\eta(1+b\eta) - \frac{i(\eta-\bar{\eta})^2}{2s^2}\right] + \frac{1}{2}\cos\left[\eta(1+b\eta) + \frac{i(\eta-\bar{\eta})^2}{2s^2}\right] \\
&- \frac{1}{2}i\sin\left[\eta(1+b\eta) - \frac{i(\eta-\bar{\eta})^2}{2s^2}\right] + \frac{1}{2}i\sin\left[\eta(1+b\eta) + \frac{i(\eta-\bar{\eta})^2}{2s^2}\right] \\
&- \frac{\Delta\left(\cosh\left[\frac{s^2\left(i+2\Delta^2\eta(1+b\eta)\right)+i\Delta^2(\eta-\bar{\eta})^2+2\bar{\eta}(1+b\bar{\eta})}{4bs^2+2i(1+s^2\Delta^2)}\right]\right)}{2\sqrt{-2ib+\frac{1}{s^2}}\sqrt{\frac{i+2bs^2+is^2\Delta^2}{i+2bs^2}}} \\
&+ \frac{\Delta\left(\sinh\left[\frac{s^2\left(i+2\Delta^2\eta(1+b\eta)\right)+i\Delta^2(\eta-\bar{\eta})^2+2\bar{\eta}(1+b\bar{\eta})}{4bs^2+2i(1+s^2\Delta^2)}\right]\right)}{2\sqrt{-2ib+\frac{1}{s^2}}\sqrt{\frac{i+2bs^2+is^2\Delta^2}{i+2bs^2}}} \\
&- \frac{\Delta\left(\cosh\left[\frac{s^2\left(i-2\Delta^2\eta(1+b\eta)\right)+i\left(\Delta^2(\eta-\bar{\eta})^2+2i\bar{\eta}(1+b\bar{\eta})\right)}{4bs^2-2i(1+s^2\Delta^2)}\right]\right)}{2\sqrt{2ib+\frac{1}{s^2}}\sqrt{\frac{i-2bs^2+is^2\Delta^2}{i-2bs^2}}} \\
&- \frac{\Delta\left(\sinh\left[\frac{s^2\left(i-2\Delta^2\eta(1+b\eta)\right)+i\left(\Delta^2(\eta-\bar{\eta})^2+2i\bar{\eta}(1+b\bar{\eta})\right)}{4bs^2-2i(1+s^2\Delta^2)}\right]\right)}{2\sqrt{2ib+\frac{1}{s^2}}\sqrt{\frac{i-2bs^2+is^2\Delta^2}{i-2bs^2}}}.
\end{aligned} \tag{A.2}$$

Bibliography

[1] A. Einstein, "Zur Quantentheorie der Strahlung," Physikalische Zeitschrift **18** (1917).

[2] T. H. Maiman, "Stimulated optical radiation in ruby," Nature **187**, 493–494 (1960).

[3] D. Strickland, G. A. Mourou, "Compression of amplified chirped optical pulses," Opt. Commun. **56**, 219–221 (1985).

[4] A. Dubietis, G. Jonusauskas, and A. Piskarskas, "Powerful femtosecond pulse generation by chirped and stretched pulse parametric amplification in BBO crystal," Opt. Commun. **88**, 437–440 (1992).

[5] S.-W. Bahk, P. Rousseau, T. A. Planchon, V. Chvykov, G. Kalintchenko, A. Maksimchuk, G. A. Mourou, and V. Yanovsky, "Generation and characterization of the highest laser intensities (1022 W/cm2)," Opt. Lett. **29**, 2837–2839 (2004).

[6] "The Extreme Light Infrastructure European Project (ELI). Scientific Case," (2007). `http://www.extreme-light-infrastructure.eu/pictures/ELI-scientific-case-id17.pdf`.

[7] "High Power Laser Energy Research (HiPER). HiPER technical background and conceptual design report," `http://www.hiperlaser.org/docs/tdr/HiPERTDR2.pdf`.

[8] Y. I. Salamin, S. X. Hu, K. Z. Hatsagortsyan, and C. H. Keitel, "Relativistic high-power laser-matter interactions," Physics Reports **427**, 41–155 (2006).

[9] G. A. Mourou, T. Tajima, and S. V. Bulanov, "Optics in the relativistic regime," Rev. Mod. Phys. **78**, 309–371 (2006).

[10] F. Krausz and M. Ivanov, "Attosecond physics," Rev. Mod. Phys. **81**, 163–234 (2009).

[11] "LHC–The Large Hadron Collider," `http://lhc.web.cern.ch/lhc/`.

[12] "Deconstruction: large hadron collider," `http://www.symmetrymagazine.org/cms/?pid=1000350`.

[13] H. Eickhoff, D. Böhne, T. Haberer, B. Schlitt, P. Spiller, J. Debus, and A. Dolinskii, "HIT–Heidelberg Ion beam Therapy. Scientific Case." http://www-aix.gsi.de/~spiller/facilit_ep00.ps.

[14] "HIT–Heidelberg Ion beam Therapy. Facts in short." http://www.klinikum.uni-heidelberg.de/index.php?id=115415&L=en.

[15] O. Jäkel, M. Krämer, C. P. Karger, and J. Debus, "Treatment planning for heavy ion radiotherapy: clinical implementation and application," Phys. Med. Biol. **46**, 1101–1116 (2001).

[16] T. I. Yock and N. J. Tarbell, "Technology Insight: proton beam radiotherapy for treatment in pediatric brain tumors," Nature Clinical Practice Oncology **1**, 97–103 (2004).

[17] M. P. Levin, H. Kooy, J. S. Loeffler, and T. F. DeLaney, "Proton beam therapy," British Journal of Cancer **93**, 849–854 (2005).

[18] S. E. Combs, A. Nikoghosyan, O. Jaekel, C. P. Karger, T. Haberer, M. W. Münter, P. E. Huber, J. Debus, and D. Schulz-Ertner, "Carbon ion radiotherapy for pediatric patients and young adults treated for tumors of the skull base," Cancer **115**, 1348–1355 (2009).

[19] E. Fokas, G. Kraft, H. An, and R. Engenhart-Cabillic, "Ion beam radiobiology and cancer: Time to update ourselves," Biochimica et Biophysica Acta (BBA) - Reviews on Cancer **1796**, 216 – 229 (2009).

[20] J. Weichsel, T. Fuchs, E. Lefebvre, E. d'Humières, and U. Oelfke, "Spectral features of laser-accelerated protons for radiotherapy applications," Phys. Med. Biol. **53**, 4383–4397 (2008).

[21] "Vulcan laser facility," http://www.clf.rl.ac.uk/Facilities/Vulcan/12248.aspx.

[22] R. Paschotta, "Encyclopedia of laser physics and technology," http://www.rp-photonics.com/optical_parametric_chirped_pulse_amplification.html.

[23] L. D. Landau and L. M. Lifshitz, *Classical theory of fields* (Addison Wesley, 1962), 2nd ed.

[24] J. H. Eberly and A. Sleeper, "Trajectory and mass shift of a classical electron in a radiation pulse," Phys. Rev. **176**, 1570–1573 (1968).

[25] J. E. Gunn and J. P. Ostriker, "On the motion and radiation of charged particles in strong electromagnetic waves. I. Motion in plane and spherical waves," Astrophys. J. **165**, 523–541 (1971).

[26] P. Gibbon, *Short pulse laser interaction with matter* (Imperial College Press, 2005), fist ed.

[27] J. D. Lawson, "Lasers and accelerators," IEEE Trans. Nucl. Sci. **NS-26**, 4217 (1979).

[28] P. M. Woodward, J. IEEE **93**, 1554 (1979).

[29] L. W. Davis, "Theory of electromagnetic beams," Phys. Rev. A **19**, 1177–1179 (1979).

[30] D. Bauer, P. Mulser, and W. H. Steeb, "Relativistic ponderomotive force, uphill acceleration, and transition to chaos," Phys. Rev. Lett. **75**, 4622–4625 (1995).

[31] C. M. Haaland, "Laser electron acceleration in vacuum," Opt. Commun. **114**, 280–284 (1995).

[32] E. Esarey, P. Sprangle, and J. Krall, "Laser acceleration of electrons in vacuum," Phys. Rev. E **52**, 5443–5453 (1995).

[33] Y. I. Salamin and C. H. Keitel, "Electron acceleration by a tightly focused laser beam," Phys. Rev. Lett. **88**, 095005 (2002).

[34] Y. I. Salamin, G. R. Mocken, and C. H. Keitel, "Electron scattering and acceleration by a tightly focused laser beam," Phys. Rev. ST Accel. Beams **5**, 101301 (2002).

[35] P. X. Wang, Y. K. Ho, X. Q. Yuan, Q. Kong, N. Cao, A. M. Sessler, E. Esarey, and Y. Nishida, "Vacuum electron acceleration by an intense laser," Appl. Phys. Lett. **78**, 2253 (2001).

[36] Q. Kong, Y. K. Ho, N. Cao, J. Pang, P. X. Wang, and L. Shao, "Electron dynamics characteristics in high-intensity laser fields ," Appl. Phys. B **74**, 517 (2002).

[37] Y. I. Salamin and C. H. Keitel, "Subcycle high electron acceleration by crossed laser beams," Appl. Phys. Lett. **77**, 1082–1084 (2000).

[38] Y. I. Salamin, G. R. Mocken, and C. H. Keitel, "Relativistic electron dynamics in intense crossed laser beams: Acceleration and Compton harmonics," Phys. Rev. E **67**, 016501 (2003).

[39] Y. I. Salamin, "Covariant electron dynamics in two interfering laser beams: analysis of the vacuum beat wave accelerator," Phys. Lett. A **270**, 115–121 (2000).

[40] Y. I. Salamin, "Electron acceleration in a tightly-focused vacuum laser beat wave," Phys. Lett. A **335**, 289–294 (2005).

[41] S. X. Hu and A. F. Starace, "Gev electrons from ultraintense laser interaction with highly charged ions," Phys. Rev. Lett. **88**, 245003 (2002).

[42] Y. I. Salamin, F. H. M. Faisal, and C. H. Keitel, "Exact analysis of ultrahigh laser-induced acceleration of electrons by cyclotron autoresonance," Phys. Rev. A **62**, 053809 (2000).

[43] T. Tajima and J. M. Dawson, "Laser electron accelerator," Phys. Rev. Lett. **43**, 267–270 (1979).

[44] A. Modena, Z. Najmudin, A. E. Dangor, C. E. Clayton, K. A. Marsh, C. Joshi, V. Malka, C. B. Darrow, C. Danson, D. Neely, and F. N. Walsh, "Electron acceleration from the breaking of relativistic plasma waves," Nature **377**, 606–608 (1995).

[45] C. I. Moore, A. Ting, K. Krushelnick, E. Esarey, R. F. Hubbard, B. Hafizi, H. R. Burris, C. Manka, and P. Sprangle, "Electron trapping in self-modulated laser wakefields by raman backscatter," Phys. Rev. Lett. **79**, 3909–3912 (1997).

[46] V. Malka, S. Fritzler, E. Lefebvre, M.-M. Aleonard, F. Burgy, J.-P. Chambaret, J.-F. Chemin, K. Krushelnick, G. Malka, S. P. D. Mangles, Z. Najmudin, M. Pittman, J.-P. Rousseau, J.-N. Scheurer, B. Walton, and A. E. Dangor , "Electron Acceleration by a Wake Field Forced by an Intense Ultrashort Laser Pulse," Science **298**, 1596–1600 (2002).

[47] J. Faure, Y. Glinec, A. Pukhov, S. Kiselev, S. Gordienko, E. Lefebvre, J.-P. Rousseau, F. Burgy, and V. Malka, "A laser-plasma accelerator producing monoenergetic electron beams," Nature **431**, 541–544 (2004).

[48] A. Caldwell, K. Lotov, A. Pukhov, and F. Simon, "Proton-driven plasma-wakefield acceleration," Nature Physics **5**, 363–367 (2009).

[49] A. Henig, S. Steinke, M. Schnürer, T. Sokollik, R. Hörlein, D. Kiefer, D. Jung, J. Schreiber, B. M. Hegelich, X. Q. Yan, J. Meyer-ter Vehn, T. Tajima, P. V. Nickles, W. Sandner, and D. Habs, "Radiation-pressure acceleration of ion beams driven by circularly polarized laser pulses," Phys. Rev. Lett. **103**, 245003 (2009).

[50] B. M. Hegelich, B. J. Albright, J. Cobble, K. Flippo, S. Letzring, M. Paffett, H. Ruhl, J. Schreiber, R. K. Schulze, and J. C. Fernández, "Laser acceleration of quasi-monoenergetic MeV ion beams," Nature **439**, 441–444 (2006).

[51] H. Schwoerer, S. Pfotenhauer, O. Jäckel, K.-U. Amthor, B. Liesfeld, W. Ziegler, R. Sauerbrey, K. W. D. Ledingham, and T. Esirkepov, "Laser-plasma acceleration of quasi-monoenergetic protons from microstructured targets," Nature **439**, 445–448 (2006).

[52] J. Fuchs, P. Antici, E. dHumières, E. Lefebvre, M. Borghesi, E. Brambrink, C. A. Cecchetti, M. Kaluza, V. Malka, M. Manclossi, S. Meyroneinc, P. Mora, J. Schreiber, T. Toncian, H. Pépin, and P. Audebert, "Laser-driven proton scaling laws and new paths towards energy increase," Nature Physics **2**, 48–54 (2006).

[53] L. Robson, P. T. Simpson, R. J. Clarke, K. W. D. Ledingham, F. Lindau, O. Lundh, T. McCanny, P. Mora, D. Neely, C.-G. Wahlström, M. Zepf,

and P. McKenna, "Scaling of proton acceleration driven by petawatt-laser-plasma interactions," Nature Physics **3**, 58–62 (2007).

[54] A. Maksimchuk, S. Gu, K. Flippo, D. Umstadter, and V. Y. Bychenkov, "Forward ion acceleration in thin films driven by a high-intensity laser," Phys. Rev. Lett. **84**, 4108–4111 (2000).

[55] R. A. Snavely, M. H. Key, S. P. Hatchett, T. E. Cowan, M. Roth, T. W. Phillips, M. A. Stoyer, E. A. Henry, T. C. Sangster, M. S. Singh, S. C. Wilks, A. MacKinnon, A. Offenberger, D. M. Pennington, K. Yasuike, A. B. Langdon, B. F. Lasinski, J. Johnson, M. D. Perry, and E. M. Campbell, "Intense high-energy proton beams from petawatt-laser irradiation of solids," Phys. Rev. Lett. **85**, 2945–2948 (2000).

[56] S. Karsch, S. Düsterer, H. Schwoerer, F. Ewald, D. Habs, M. Hegelich, G. Pretzler, A. Pukhov, K. Witte, and R. Sauerbrey, "High-intensity laser induced ion acceleration from heavy-water droplets," Phys. Rev. Lett. **91**, 015001 (2003).

[57] L. Romagnani, J. Fuchs, M. Borghesi, P. Antici, P. Audebert, F. Ceccherini, T. Cowan, T. Grismayer, S. Kar, A. Macchi, P. Mora, G. Pretzler, A. Schiavi, T. Toncian, and O. Willi, "Dynamics of electric fields driving the laser acceleration of multi-mev protons," Phys. Rev. Lett. **95**, 195001 (2005).

[58] A. J. Mackinnon, M. Borghesi, S. Hatchett, M. H. Key, P. K. Patel, H. Campbell, A. Schiavi, R. Snavely, S. C. Wilks, and O. Willi, "Effect of plasma scale length on multi-mev proton production by intense laser pulses," Phys. Rev. Lett. **86**, 1769–1772 (2001).

[59] J. Badziak, "Laser-driven generation of fast particles," Opto-Electr. Review **15**, 1–12 (2007).

[60] A. Macchi, S. Veghini, and F. Pegoraro, ""light sail" acceleration reexamined," Phys. Rev. Lett. **103**, 085003 (2009).

[61] S. V. Bulanov, E. Y. Echkina, T. Z. Esirkepov, I. N. Inovenkov, M. Kando, F. Pegoraro, and G. Korn, "Unlimited ion acceleration by radiation pressure," Phys. Rev. Lett. **104**, 135003 (2010).

[62] Y. I. Salamin, Z. Harman, and C. H. Keitel, "Direct high-power laser acceleration of ions for medical applications," Phys. Rev. Lett. **100**, 155004 (2008).

[63] Y. I. Salamin, "Fields of a Gaussian beam beyond paraxial approximation," Appl. Phys. B **86**, 319–326 (2007).

[64] Y. I. Salamin, "Fields of a radially polarized Gaussian laser beam beyond the paraxial approximation," Opt. Lett. **31**, 2619–2621 (2006).

[65] Y. I. Salamin, "Accurate fields of a radially polarized Gaussian laser beam ," New J. of Phys. **8**, 133 (2006).

[66] K. P. Singh, "Electron acceleration by a chirped short intense laser pulse in vacuum," Appl. Phys. Lett. **87**, 254102 (2005).

[67] F. Sohbatzadeh, S. Mirzanejhad, and M. Ghasemi, "Electron acceleration by a chirped Gaussian pulse," Phys. Plasmas **13**, 123108 (2006).

[68] S. M. F. Sohbatzadeh and H. Aku, "Synchronization scheme in electron vacuum acceleration by a chirped gaussian pulse," Phys. Plasmas **16**, 023106 (2009).

[69] J. M. Dawson, "Particle simulation of plasmas," Rev. Mod. Phys. **55**, 403–447 (1983).

[70] Z. Harman, Y. I. Salamin, B. J. Galow, and C. H. Keitel, "Optimizing direct intense-field laser acceleration of ions," Phys. Rev. A **84**, 053814 (2011).

[71] Y. I. Salamin, "Acceleration in vacuum of bare nuclei by tightly focused radially polarized laser light," Opt. Lett. **32**, 3462–3464 (2007).

[72] I. Pogorelsky, V. Yakimenko, M. Polyanskiy, P. Shkolnikov, M. Ispiryan, D. Neely, P. McKenna, D. Carroll, Z. Najmudin, and L. Willingale, "Ultrafast CO_2 laser technology: Application in ion acceleration," Nuclear Instruments and Methods in Physics Research Section A: Accelerators, Spectrometers, Detectors and Associated Equipment **620**, 67 – 70 (2010).

[73] GSI. See `http://www.gsi.de/portrait/Broschueren/Therapie/synchrotron(ep2000).pdf` .

[74] Y. I. Salamin, "Electron acceleration from rest in vacuum by an axicon Gaussian laser beam," Phys. Rev. A **73**, 043402 (2006).

[75] The use of this figure is kindly authorized by Y. I. Salamin.

[76] J. P. Barton and D. R. Alexander, "Fifthorder corrected electromagnetic field components for a fundamental gaussian beam," J. Appl. Phys. **66**, 2800 (1989).

[77] S. Quabis, R. Dorn, M. Eberler, O. Glöckl, and G. Leuchs, "The focus of light – theoretical calculation and experimental tomographic reconstruction," Appl. Phys. B **72**, 109 (2001).

[78] R. Dorn, S. Quabis, and G. Leuchs, "Sharper focus for a radially polarized light beam," Phys. Rev. Lett. **91**, 233901 (2003).

[79] S. Quabis, R. Dorn, M. Eberler, O. Glöckl, and G. Leuchs, "Generation of a radially polarized doughnut mode of high quality," Appl. Phys. B **81**, 597 (2005).

[80] J. D. Jackson, *Classical Electrodynamics* (John Wiley & Sons, 1999), 3rd ed.

[81] Y. I. Salamin, "Direct particle acceleration by two identical crossed radially polarized laser beams," Phys. Rev. A **82**, 013823 (2010).

[82] B. J. Galow, Z. Harman, and C. H. Keitel, "Intense high-quality medical proton beams via laser fields," Opt. Express **18**, 25950–25957 (2010).

[83] B. Qiao, M. Zepf, M. Borghesi, and M. Geissler, "Stable GeV ion-beam acceleration from thin foils by circularly polarized laser pulses," Phys. Rev. Lett. **102**, 145002 (2009).

[84] K. T. MacDonald. `http://www.hep.princton.edu/~mcdonald/accel/gaussian.ps`.

[85] K. T. MacDonald. `http://www.hep.princton.edu/~mcdonald/accel/gaussian2.ps`.

[86] C. A. J. Palmer, N. P. Dover, I. Pogorelsky, M. Babzien, G. I. Dudnikova, M. Ispiriyan, M. N. Polyanskiy, J. Schreiber, P. Shkolnikov, V. Yakimenko, and Z. Najmudin, "Monoenergetic proton beams accelerated by a radiation pressure driven shock," Phys. Rev. Lett. **106**, 014801 (2011).

[87] Z. Major, S. Trushin, I. Ahmad, M. Siebold, C. Wandt, S. Klingebiel, T.-J. Wang, J. A. Fülöyanp, A. Henig, S. Kruber, R. Weingartner, A. Popp, J. Osterhoff, R. Hörlein, J. Hein, V. Pervak, A. Apolonski, F. Krausz, and S. Karsch, "Basic concepts and current status of the petawatt field synthesizer a new approach to ultrahigh field generation," The Review of Laser Engineering **37**, 431–436 (2009).

[88] J. X. Wang, Y. K. Ho, L. Feng, Q. Kong, P. X. Wang, Z. S. Yuan, and W. Scheid, "High-intensity laser-induced electron acceleration in vacuum," Phys. Rev. E **60**, 7473–7478 (1999).

[89] Z. Yan, Y. K. Ho, P. X. Wang, J. F. Hua, Z. Chen, and L. Wu, "Accurate description of ultra-short tightly focused Gaussian laser pulses and vacuum laser acceleration," Appl. Phys. B **81**, 813–819 (2005).

[90] P. X. Wang, S. Kawata, and Y. K. Ho, "Simulations of vacuum laser acceleration: Hidden errors from particles initial positions," Opt. Express **18**, 14144–14151 (2010).

[91] X. Jaén, J. Llosa, and A. Molina, "A reduction of order two for infinite-order lagrangians," Phys. Rev. D **34**, 2302–2311 (1986).

[92] G. V. Stupakov and M. S. Zolotorev, "Ponderomotive laser acceleration and focusing in vacuum for generation of attosecond electron bunches," Phys. Rev. Lett. **86**, 5274–5277 (2001).

[93] E. Gerstner, "Laser physics: Extreme light," Nature **446**, 16–18 (2007).

[94] B. J. Galow, Y. I. Salamin, T. V. Liseykina, Z. Harman, and C. H. Keitel, "Dense monoenergetic proton beams from chirped laser-plasma interaction," Phys. Rev. Lett. **107**, 185002 (2011).

[95] The use of this figure is kindly authorized by Y. I. Salamin.

[96] M. Schollmeier, S. Becker, M. Geißel, K. A. Flippo, A. Blažević, S. A. Gaillard, D. C. Gautier, F. Grüner, K. Harres, M. Kimmel, F. Nürnberg, P. Rambo, U. Schramm, J. Schreiber, J. Schütrumpf, J. Schwarz, N. A. Tahir, B. Atherton, D. Habs, B. M. Hegelich, and M. Roth, "Controlled transport and focusing of laser-accelerated protons with miniature magnetic devices," Phys. Rev. Lett. **101**, 055004 (2008).

[97] E. Goulielmakis, S. Koehler, B. Reiter, M. Schultze, A. J. Verhoef, E. E. Serebryannikov, A. M. Zheltikov, and F. Krausz, Opt. Lett. **33**, 1407–1409 (2008).

[98] R. K. Shelton, L.-S. Ma, H. C. Kapteyn, M. M. Murnane, J. L. Hall, and Jun Ye, "Phase-coherent optical pulse synthesis from separate femtosecond lasers," Science **293**, 1286–1289 (2001).

[99] H.-S. Chan, Z.-M. Hsieh, W.-H. Liang, A. H. Kung, C.-K. Lee, C.-J. Lai, R.-P. Pan, and L.-H. Peng, "Synthesis and measurement of ultrafast waveforms from five discrete optical harmonics," Science **331**, 1165–1168 (2011).

[100] R. Paschotta, "Encyclopedia of laser physics and technology," `http://www.rp-photonics.com/optical_intensity.html`.

[101] A. A. Vlasov, "On vibration properties of electron gas," J. Exp. Theor. Phys. **8**, 291 (1938).

[102] A. A. Vlasov, "The vibrational properties of an electron gas," Soviet Physics Uspekhi **10**, 721 (1968).

[103] V. A. Vshivkov and G. I. Dudnikova, "Algorithms for the solution of the problem of laser pulse interaction with plasma," Computational technologies **6**, 47–63 (2001).

[104] G. I. Dudnikova, T. V. Liseikina, and V. Y. Bychenkov, "Parallel algorithms for numerical simulation of electromagnetic radiation propagation in plasma," Computational technologies **10**, 37–48 (2005).

[105] A. Macchi, F. Califano, F. Cornolti, F. Pegoraro, S. V. Bulanov, T. V. Liseikina, and H. Ruhl, *Asymmetry and polarization effects in relativistic laser interaction with underdense plasmas, in: Science and Supercomputing at CINECA - Report 2001* (2001), cineca ed.

[106] T. V. Liseykina, private communication.

[107] F. Peano, J. L. Martins, R. A. Fonseca, L. O. Silva, G. Coppa, F. Peinetti, and R. Mulas, "Dynamics and control of the expansion of finite-size plasmas produced in ultraintense laser-matter interactions," Phys. Plasmas **14**, 056704 (2007).

[108] A. Wirth, M. T. Hassan, I. Grguras, J. Gagnon, A. Moulet, T. T. Luu, S. Pabst, R. Santra, Z. A. Alahmed, A. M. Azzeer, V. S. Yakovlev, V. Pervak, F. Krausz, and E. Goulielmakis, "Synthesized light transients," Science **334**, 195–200 (2011).

[109] T. V. Liseykina, S. Pirner, and D. Bauer, "Relativistic attosecond electron bunches from laser-illuminated droplets," Phys. Rev. Lett. **104**, 095002 (2010).

[110] M. Tamburini, F. Pegoraro, A. Di Piazza, C. H. Keitel, and A. Macchi, "Radiation reaction effects on radiation pressure acceleration," New J. Phys. **12**, 123005 (2010).

[111] A. M. Fedotov, N. B. Narozhny, G. Mourou, and G. Korn, "Limitations on the attainable intensity of high power lasers," Phys. Rev. Lett. **105**, 080402 (2010).

[112] E. N. Nerush, I. Y. Kostyukov, A. M. Fedotov, N. B. Narozhny, N. V. Elkina, and H. Ruhl, "Laser field absorption in self-generated electron-positron pair plasma," Phys. Rev. Lett. **106**, 035001 (2011).

[113] S. Cipiccia, M. R. Islam, B. Ersfeld, R. P. Shanks, E. Brunetti, G. Vieux, X. Yang, R. C. Issac, S. M. Wiggins, G. H. Welsh, M.-P. Anania, D. Maneuski, R. Montgomery, G. Smith, M. Hoek, D. J. Hamilton, N. R. C. Lemos, D. Symes, P. P. Rajeev, V. O. Shea, J. M. Dias, and D. A. Jaroszynski, "Gamma-rays from harmonically resonant betatron oscillations in a plasma wake," Nature Physics **7**, 867–871 (2011).

Danksagung

An erster Stelle möchte ich Herrn Hon.-Prof. Dr. Christoph Keitel für die freundliche Aufnahme in seine Arbeitsgruppe und für seine Intuition bei der Auswahl interessanter Themen, sowie das in mich gesetzte Vertrauen danken. Seine Unterstützung und seine unentbehrlichen Ratschläge haben diese Arbeit überhaupt erst ermöglicht.

Großer Dank geht an Herrn PD Dr. Andrey Surzhykov für die Übernahme der Zweitkorrektur und für viele spannende Seminare.

Vielen Dank auch an Herrn Prof. Dr. Dirk Dubbers und Herrn Prof. Dr. Klaus Pfeilsticker für ihre Bereitschaft an meinem Rigorosum teilzunehmen.

Zu tiefem Dank bin ich meinem Mitbetreuer Herrn Dr. Zoltán Harman verpflichtet, der sich nach Belieben Zeit für mich nahm und dessen Ideen wichtige Beiträge zu meiner Arbeit lieferten. Herzlichen Dank für all die gemeinsame Diskussionen, die Geduld und den Glauben an mich.

An nächster Stelle möchte ich mich bei Herrn Prof. Dr. Yousef Salamin bedanken, von dessen Arbeiten ich für mein Thema relevante Methoden erlernen konnte. Herzlichen Dank auch für tiefsinnige Gespräche, die weit über den Rahmen meiner Arbeit hinaus gingen.

Besonderer Dank gilt Herrn Prof. Dr. Hans Jürgen Pirner. Er brachte mir in seinen Vorlesungen, während einer Miniforschung und meiner Diplomarbeit in seiner Gruppe wertvolle Grundlagen der theoretischen Physik bei.

Dr. Tatyana Liseykina und Dr. Thomas Pfeifer gilt mein Dank für die prompte Beantwortung vieler Fragen.

Desweiteren danke ich den Gruppenleitern PD Dr. Antonino Di Piazza, PD Dr. Jörg Evers, Dr. habil. Karen Hatsagortsyan und PD Dr. Dr. Carsten Müller, die stets ein offenes Ohr für Fragen hatten.

Für herausragende organisatorische Tätigkeiten danke ich dem ehemaligen Computeradministrator Peter Brunner, unserer Sekretärin Sibel Babacan und dem Computeradministrator Dominik Hertel.

Von meinen übrigen Kollegen und Freunden danke ich Sven Augustin und Dr. Markus Kohler für das Korrekturlesen von Teilen meiner Arbeit. Bei Dr. Ben King möchte ich mich für unsere gemeinsamen Stunden bedanken, die wir dazu nutzten über spannende Themen der Physik außerhalb unserer Gebiete zu grübeln. Felix Mackenroth danke ich für themenbezogene Gespräche. Für viele lustige gemeinsame Stunden danke ich Anis Dadi, Dr. Hossein Ebadi, Dr. Huayu Hu, Dr. Mihai Macovei, Dr. Bennaceur Najjari, Dr. Octavian Postavaru, Sandra Schmid, Dr. Jacek Zatorski, ...

Für immer dankbar bin ich meiner Familie, die mich all die Jahre lang mit Rat und Tat unterstützte. Insbesondere gilt der Dank meinen Eltern, welche mir von klein auf das Streben nach Wissen als eines der höchsten Güter der Menschheit vermittelten.

Meinen langjährigen treuen Freunden Lars A., Markus D., Peter G. und Benjamin K. danke ich für die unvergesslichen Momente, welche wir zusammen erleben durften.

Ich möchte mich auch ganz herzlich bei der Familie meiner Frau bedanken, die mich nett aufnahm. Vielen Dank für die schönen gemeinsamen Stunden und die Hilfsbereitschaft.

Meinen größten Dank möchte ich meiner Ehefrau Saskia aussprechen, die all die Jahre zu mir hielt, nie den leisesten Zweifel aufkommen ließ und ohne deren Unterstützung, Geduld und Liebe dieser Lebensabschnitt undenkbar gewesen wäre.